SCUOLA DI DOTTORATO
UNIVERSITÀ DEGLI STUDI DI MILANO-BICOCCA

Department of Materials Science

PhD program Materials Science and Nanotechnology Cycle XXX

Curriculum in Materials Science

Synthesis and self-assembly of biocompatible amphiphilic block copolymers

Surname Bertani Name Daniela

Registration number 716995

Tutor: prof. Roberto Simonutti

Coordinator: prof. Marco Bernasconi

ACADEMIC YEAR 2016/2017

TABLE OF CONTENTS

CHAPTER 1

Introduction

1.1 Drug delivery

Nanomedicine is the application of nanotechnology to medicine. It aims to address several obstacles to the diagnosis and treatment of serious diseases faced by modern medicine. Despite outstanding advancements in cancer biology and pharmaceutical design in the last few decades, ultimate drug efficacy has failed to progress at a comparable pace.[1] Timing of release and effective and selective drug transport to the desired target are the two main challenges that must be met to ensure proper treatment with minimal adverse effects. Polymeric drug carriers have proved to be able to provide protective encapsulation to their cargo, prolonging circulation times and delaying its release within the therapeutic window.

In this PhD thesis, the self-assembly of amphiphilic block copolymers constituted by biocompatible hydrophilic blocks is investigated.

In Chapter 2, relevant controlled polymerization techniques and mechanisms are described.

In Chapter 3, a complete picture of the previously unreported self-assembly behavior of RAFT-synthesized poly(styrene)-*block*-poly(N,N'-dimethylacrylamide) (PS-*b*-PDMA) by the solvent switching method from DMF is drawn. A comprehensive sample set covering a 10 kDa – 57 kDa molecular weight range and 0.09 – 0.75 hydrophilic volume fraction range was prepared. Obtained nanoparticle morphologies were analyzed in depth with various microscopy techniques (TEM, CEM, CET, FIB-SEM, AFM) and correlated with copolymer chemical characteristics in a morphology map. Interestingly, PS-*b*-PDMA samples close to the "crew-cut" compositional range exhibited a tendency to form hierarchical aggregates. In particular, low molecular weight and low hydrophilic fraction copolymers organized in extended, open bilayers intertwining in bicontinuous disordered networks spanning several microns. A continuous porous sponge phase was observed inside microparticles, stable enough to withstand lyophilization.

In Chapter 4, the framework of well-known biocompatible and biodegradable poly(ethylene oxide)-*block*-poly(D,L-lactic acid) (PEO-*b*-PLA) was expanded to include the effect of the non-selective solvent on nanoparticle final morphologies during solvent switching. A clear trend in nanoparticle size and PDI variation followed the choice of organic solvent in the order ACT < DX < THF ~ DMF, which is only partially supported by conventional considerations based on solubility theories. CEM and CET were used to characterize nanoparticles and to map the morphological areas made accessible by each non-selective

solvent. This map is a useful tool to aid in the selection of the organic solvent for the fabrication of nanoparticles of the desired size and shape.

In Chapter 5, three polymeric precursors were prepared by CROP of 2-ethyl-2-oxazoline (EtOx). The great functionalization flexibility of these systems was explored by selecting three terminating agents: methanolic KOH, to introduce a terminal –OH group that can be exploited as an initiator of lactide ROP; 2-(Dodecylcarbonylthioylthio)-2-methylpropionic acid (DDAT), in order to use PEtOx as a macro-chain transfer agent for RAFT polymerization; and acrylic acid, that would allow the synthesis of bottle-brush PEtOx polymers. After successful functionalization was achieved in all cases, PEtOx-DDAT was used for the synthesis of poly(2-ethyl-2-oxazoline)-*block*-poly(styrene)-*block*-poly(*tert*-butyl acrylate) (PEtOx-*b*-PS-*b*-P*t*BA), a triblock copolymer bearing two hydrophobic blocks for which different selective solvents can be found. Furthermore, the *tert*-butyl residue can be cleaved to yield poly(acrylic acid) (PAA).

In Chapter 6, the research focus was shifted from the characterization of final morphologies to the *in situ* monitoring of nanoparticle formation during solvent switching. A fluorescent molecular rotor was used as a viscosity probe and encapsulated inside forming nanoparticles. TRPL spectroscopy provides interesting insight on chain mobility and glass transition at the nanoscale in PS-*b*-PDMA and PEO-*b*-PLA self-assembled from different organic solvents. Our results suggest that core-forming chain mobility is strongly affected by the solvent and plays a crucial role in determining the aggregation pathway.

Finally, in Chapter 7 an alternative route to polymer nanoparticle formation was undertaken. Polymerization-induced self-assembly of *n*-butyl acrylate (*n*BA) using a glycopolymer macro-chain transfer agent in methanol/water mixtures is described. Despite control on the polymerization was rather poor, remarkably stable soft-core spherical particles were obtained.

CHAPTER 2

Controlled polymerization techniques

2.1 RAFT polymerization

Living radical polymerization (LRP) techniques aim to conjugate the advantageous features of free radical polymerization – compatibility with a wide range of monomers and functionalities, relatively mild reaction conditions – with a good control over molecular weight distribution, chain architecture, and chain-end functionality. In order to achieve 'livingness', termination reactions, which are inherent to radical polymerization processes, need to be minimized. Among the LRP techniques developed in the last few decades, nitroxide-mediated polymerization (NMP)[2], atom transfer radical polymerization (ATRP)[3], macromolecular design via the interchange of xanthates (MADIX)[4] and radical addition-fragmentation chain transfer (RAFT) polymerization have found extensive application in polymer synthesis for several applications. MADIX and RAFT are thought to proceed via the same degenerative transfer mechanism, and differ only in the chain transfer agents (CTAs) used.

In a free radical polymerization, individual chains are formed, propagate and terminate by radical-radical reactions within 10 s. In an ideal LRP, the birth and growth of all chains are simultaneous, and no termination occurs. Due to the presence of radicals, the latter condition can never be fully met; however, a strategy to render all *irreversible* termination reactions negligible was developed at CSIRO in 1998 by Rizzardo and others.[5] Their group synthesized organic compounds that can reversibly react with propagating radical species, by reversible chain transfer mechanisms. When that occurs, propagating chains enter a temporarily non-reactive 'dormant' state. Intermittent switching between the reactive, propagating state and the dormant state ensures that all chains have equal opportunity to grow. Such 'radical regulating' compounds are thiocarbonylthio-containing molecules with generic structure depicted in Figure 2.1.

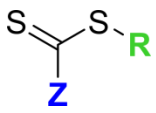

Figure 2.1 – Generic structure of RAFT chain transfer agent (CTA).

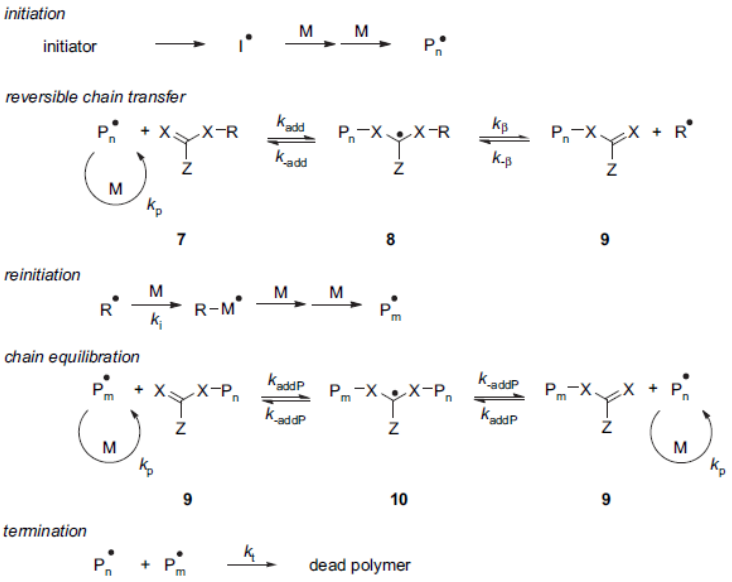

Figure 2.2 – RAFT polymerization mechanism. Reproduced from Boyer, C.; Bulmus, V.; Davis, T. P.; Ladmiral, V.; Liu, J.; Perrier, S. *Chem. Rev.* **2009**, *109*, 5402–5436.[6]

The mechanism of RAFT polymerization relies on a series of addition-fragmentation equilibria, as shown in Figure 2.2. The first step is initiation by radical formation. Thermal initiators are commonly used thanks to their market availability, but photoinitiators are also attracting considerable interest, as they allow 'on-off' polymerization rates and tolerate molecular oxygen.[7,8] Radical-bearing oligomers react with the CTA in a second initialization step. Thanks to the high reactivity of the C=S bond, radical addition is favored over double bond addition, so all CTA is consumed during this step. An equilibrium is established where radical intermediate **8** can fragment back to yield the original CTA **7** and a propagating oligomeric radical $P_m^{\bullet}$, or fragment to yield an oligomeric CTA (**9**) and release a radical re-initiator group $R^{\bullet}$. R should be a good homolytic leaving group, with a fragmentation rate k_β comparable to initiation rate k_i or fragmentation rate k_{add}. Released radicals subsequently undergo reinitiation and propagation, and growing chains rapidly switch between the propagating state and the dormant CTA end-capped state. Due to the rapid exchange between the two states, the concentration of chain radicals $P_m^{\bullet}$ is lower than the more stabilized compound **10**. This way, radical-radical termination reactions are suppressed, though not eliminated: combination or disproportion reactions can still occur. Living characteristics are imparted only when the molecular weight of the polymer formed is substantially lower than that which might be formed in the absence of a RAFT agent, and the number of polymer molecules with RAFT agent-derived ends far exceeds the number formed as a consequence of

termination.

It naturally follows that RAFT CTA design is of paramount importance to achieve a good control over polymerization. The R group should possess a better leaving ability than the propagating radical, and should be able to efficiently reinitiate monomers when expelled.[9] A trade-off has to be found between the two features, as they are respectively enhanced and diminished by radical stabilization. The choice of Z group should be guided by its ability to activate the C=S bond towards radical addition and provide little stabilization to adducts **8** and **10**, so that fragmentation is favored. For this reason, Z groups are generally suitable only for specific monomer classes. Particularly active monomers like vinyl acetate (VAc) form **10** adducts that are more stable than propagating radicals, so heteroatom-bearing Z groups are necessary to destabilize the adduct and promote fragmentation. Whereas xanthates and dithiocarbamates are effective in mediating RAFT polymerization of very active monomers, they are unsuitable in controlling the propagation of less activated monomers. Methacrylates feature a higher radical stability, and will only add to the CTA if its C=S bond is sufficiently activated; otherwise, fragmentation of adduct **10** will be favored, and the concentration of propagating radicals will reach levels where termination reactions are common, as in conventional radical polymerization. Numerous RAFT CTAs have been designed and tested on a great variety of monomers.[10,11] General molecular design guidelines have been proposed by the CSIRO and are shown in Figure 2.3.

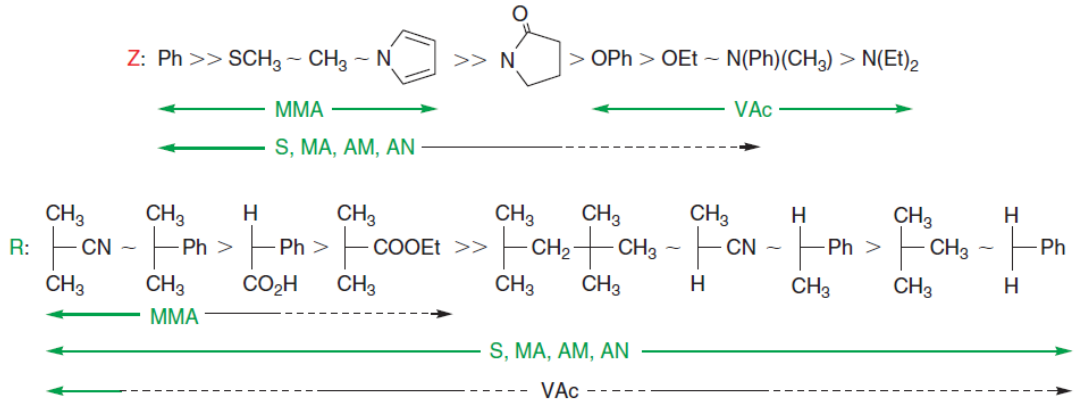

Figure 2.3 – RAFT CTA design guidelines. For Z groups, fragmentation rates increase and addition rates decrease from left to right. For R groups, fragmentation rates decrease from left to right. Dashed lines indicate partial polymerization control. MMA = methyl acrylate, VAc = vinyl acetate, S = styrene, MA = methylacrylate, AM = acrylamide, AN = acrylonitrile. Reproduced from Moad, G.; Rizzardo, A. E.; Thang, S. H. *Aust. J. Chem* **2005**, *58*, 379–410.

If the amount of dead polymer is small enough, and chain-end termination with CTA is retained (Figure 2.2, **9**), block copolymers can be synthesized by sequential RAFT

polymerization processes (Figure 2.4). The homopolymer obtained from the first polymerization acts as a macromolecular CTA (macroCTA) for the second polymerization (chain extension) step.

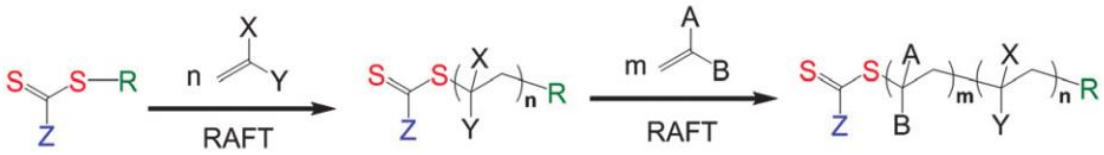

Figure 2.4 – Block copolymer synthesis by sequential RAFT polymerization of two different monomers. Reproduced from: Keddie, D. J. *Chem. Soc. Rev.* **2014**, *43* (2), 496–505.

When chain extension is planned, considerations about the suitability of the Z group must also apply to the second monomer: low activity of the macroCTA during the second step leads to increased copolymer PDI and contamination with homopolymers of the second monomer due to insufficient chain transfer. As for the R group, it is now constituted by the first block (macro-R), so appropriate choice of the R group directly translates to the appropriate choice of the order of monomer addition. Analogously to what was described above, macro-R groups that are more stable in macroradical form possess better leaving group abilities. For this reason, monomers with tertiary propagating radicals (methacrylates, methacrylamides) should be polymerized before less stabilized monomers (acrylates, acrylamides, styrenes), which should in turn be polymerized before more reactive radicals (vinyl esters, vinyl amides) (Figure 2.5).

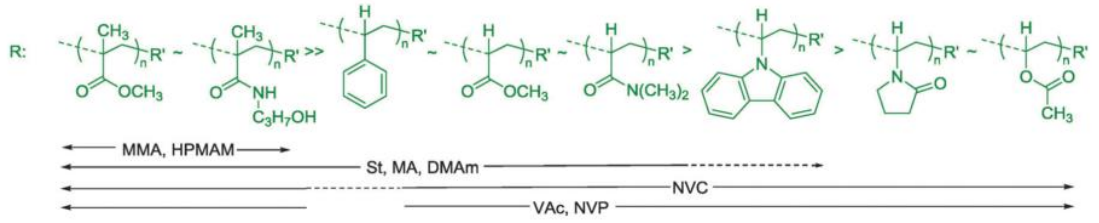

Figure 2.5 - Guidelines for selection of macro-R group for the preparation of block copolymers. Dashed lines indicate partial control over polymerization is achieved. MMA = methyl methacyrlate, HPMAM = N-(2-hydroxypropyl) methacrylamide, St = styrene, DMAm = N,N-dimethylacrylamide, NVC = N-vinylcarbazole, VAc = vinyl acetate, NVP = N-vinylpyrrolidone. Reproduced from: Keddie, D. J. *Chem. Soc. Rev.* **2014**, *43* (2), 496–505.

RAFT has found widespread application in those fields that require precise control on the polymerization and flexible reaction conditions; one of these is material synthesis for biomedical use, particularly for drug delivery. Physiological environment calls for biocompatible, hydrophilic or amphiphilic polymers with tunable properties. Most

importantly, the homogeneity of these properties and their correlation with polymer composition, architecture, and functionalization are desirable.[12] RAFT polymerization offers control over synthesis of a wide variety of monomers, in diverse reaction conditions (including water), without the need for metal-containing initiators or catalysts.[13–16] Polymers responsive to stimuli present in biological environments (temperature, pH, oxidative/reducing reactions) can be produced.[17–22] Its tolerance to diverse functionalities allows the direct incorporation of biologically relevant moieties or targeting or compatibilizing compounds such as peptides, antibodies and receptors, or post-polymerization modification by click chemistry.[23–27] RAFT can also be coupled with other pseudo-living polymerization techniques to include non-vinylic blocks, like biodegradable poly(ε-caprolactone) (PCL)[28,29] and poly(lactic acid) (PLA)[30,31], or poly(oxazoline)s (POx).[32] Drug delivery systems (DDS) built from functional RAFT-polymers are now common in the literature (Figure 2.6).[33–36]

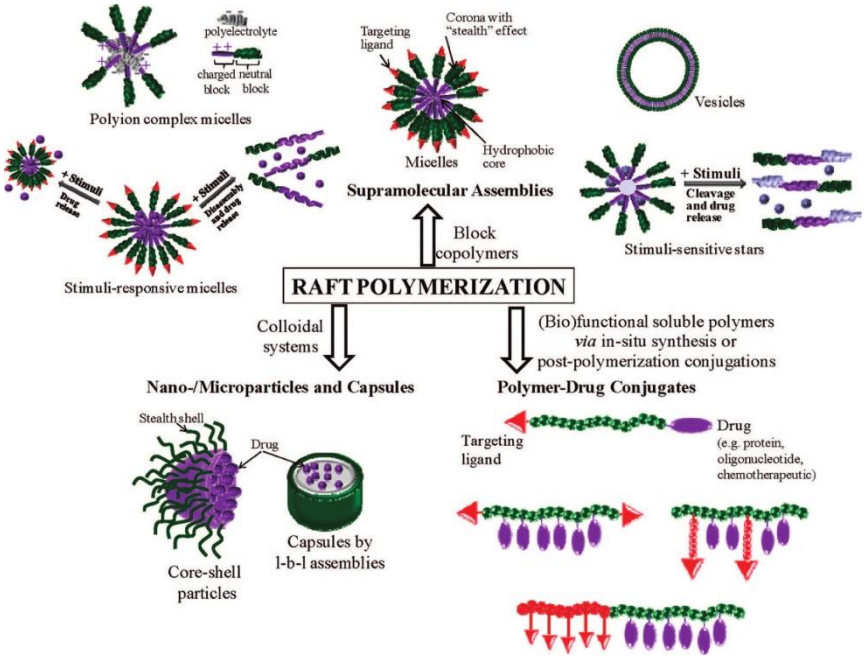

Figure 2.6 - Examples of controlled drug delivery systems by RAFT-polymers: stealth and/or targeted micelles and vesicles, stimuli-responsive micelles and stars, polyion complexes, polymer-drug conjugates, particles, and capsules. Reproduced from: Boyer, C.; Bulmus, V.; Davis, T. P.; Ladmiral, V.; Liu, J.; Perrier, S. *Chem. Rev.* **2009**, *109*, 5402–5436.[6]

2.1.1 PISA

Post-polymerization self-assembly of amphiphilic block copolymers by solvent switching methods gives access to the whole variety of possible nanoparticle morphologies, but its scalability is limited by time-consuming processing and dilute conditions. Recently, considerable interest is focused on polymerization-induced self-assembly (PISA) by RAFT chain extension: a solvophilic polymer end-capped with a RAFT functionality is used as a

stabilizing and macro-chain transfer agent for chain extension with a solvophobic block. As polymerization of the second block proceeds, the amphiphilicity of growing copolymer will increase, and bring about the formation of nanoparticles with different morphologies. If chain extension is carried out to total monomer conversion, post-polymerization purification is unnecessary; moreover, much higher dispersion concentrations can be achieved, even up to 50%-70% solid contents. Of course, direct nanoparticle formation in aqueous environment has special appeal for biomedical applications. Two approaches to PISA have been explored: *i*) emulsion polymerization conditions (insoluble monomer)[37–40] and *ii*) dispersion polymerization conditions (soluble monomer, insoluble polymer).[19,41–43] The Armes research group has thoroughly investigated dispersion PISA in fully aqueous medium. Vinyl monomers that are fully water soluble, but yield water insoluble homopolymers are relatively few: they comprise acrylamides (N-isopropyl acrylamide [NIPAm] and N,N'-diethyl acrylamide [DEAm]), acrylic and methacrylic monomers bearing short ethylene glycol side chains (2-methoxyethyl acrylate [MEA], di(ethyleneglycol) methylether methacrylate [DEGMA]) and 2-hydroxypropylmethacrylate (HPMA). Among the most common hydrophilic macroCTAs, PEO, poly(glycerol methacrylate) (PGMA) and poly(2-(methacryloyloxy)ethyl phosphorylcholine) (PMPC) CTAs allowed the formation of non-spherical morphologies when chain-extended with HPMA.[44] Morphology can be tuned by varying degrees of polymerization and solids concentration, as is shown in Figure 2.7(Left). Furthermore, by monitoring the evolution of nanostructures as a function of hydrophobic block degree of polymerization, interesting insight on the mechanisms of vesicle formation from branched worms was gained (Figure 2.7(Right)). The addition of salts or pH variations can also be used as tools for morphology control.[45]

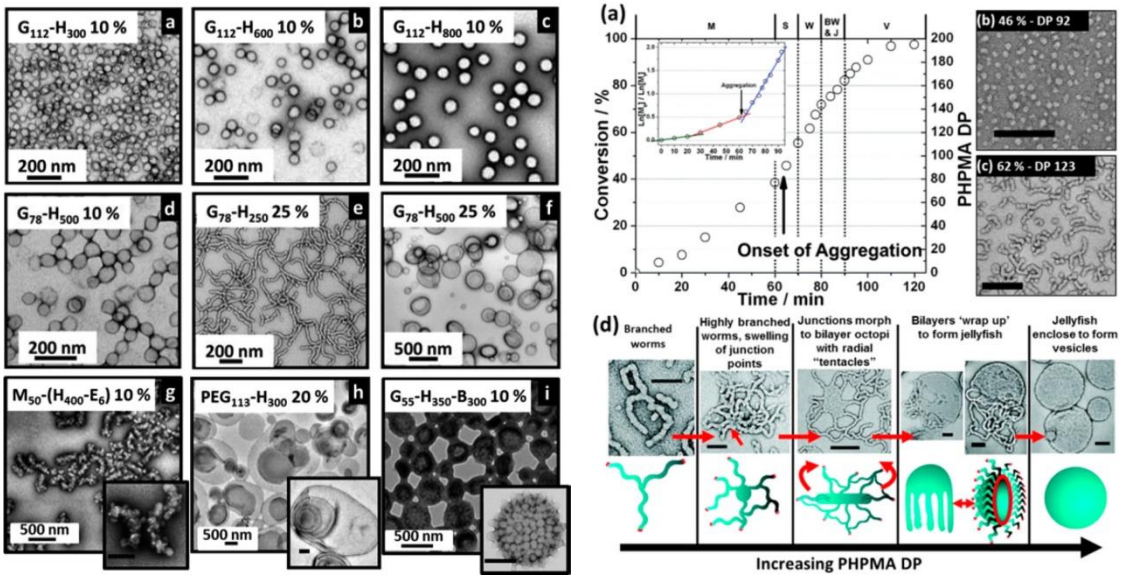

Figure 2.7 – (Left) TEM images of nanoparticles obtained by aqueous PISA at different HPMA degree of polymerization (a–c), solid content (d–f) and copolymer composition (g–i). G = GMA, H = HPMA, M = MPC, B = benzyl methacrylate. (Right) Evolution of particle morphology from branched worms to vesicles (d) as a function of HPMA degree of polymerization. Reproduced from: Warren, N. J.; Armes, S. P. *J. Am. Chem. Soc.* **2014**, *136*, 10174–10185.

The pool of viable vinyl monomers for PISA in dispersion conditions can be broadened to include other acrylates and methacrylates (n-butyl acrylate [BA], benzyl methacrylate [BzMA], MMA…) if alcohol or alcohol/water mixtures are used instead of pure water.[46] For example, Jones et al. extensively explored dispersion PISA of BzMA using a poly(N,N'-dimethylaminoethyl acrylate) (PDMAEMA) macroCTA in ethanol, obtaining monodisperse nanoparticles of various morphologies at solid contents up to 29%.[47] The composition of the dispersant plays a fundamental role during self-assembly, allowing or hindering morphology transitions from spheres to lower-curvature architectures: in a later paper, Jones et al. reported that adding water to the aforementioned PISA formulation accelerated polymerization kinetics, but limited the obtainable morphologies to spheres and worm/sphere mixes.[48] Similar observations were also reported by Zhang et al. for dispersion polymerization of BA using a PAA macroCTA in ethanol/water mixtures of variable compositions.[39] Due to the hydrophobicity of BzMA and BA, an increase in water fraction lead to a greater partitioning between monomer and solvent and an increase in local monomer concentration, which considerably sped up its consumption. On the other hand, this increased localization favored the formation of spheres, and prevented their fusion into worms and then vesicles; above a certain water fraction, reaction conditions resembled those of emulsion rather than dispersion polymerization.

PISA is also a promising platform for one-pot, one-step polymerization, self-assembly and loading of a cargo. Karagoz et al.[49] were the first to demonstrate the simultaneous PISA of Sty (using a poly(oligoethyleneglycol methacrylate) [POEGMA]) and incorporation of Nile Red in methanol. Successful incapsulation of singlet oxygen-generating porphyrins,[50] silica nanoparticles and bovine serum albumin (BSA) followed in the next few years,[51] confirming PISA's applicability in biomedicine and drug delivery.

2.2 Controlled ROP polymerization

Ring opening polymerization (ROP) techniques allow the controlled synthesis of polymers bearing heteroatoms and other functional groups on their backbone, which are of particular importance in biomedical applications by virtue of their potential biodegradability and/or analogy to naturally occurring polymers.

The forces that drive ROP may vary with the involved monomers; however, all ROP benefit by the enthalpy loss associated with the opening of a strained ring. An additional gain in entropy can occur when moieties with low rotational freedom, such as carbonates or disulfides, constitute the ring. In fact, 6-membered rings generally feature very little strain, but lactide and glycolide are polymerizable, thanks to the planar conformation of the two ester moieties. Still, the very low ring strain makes depolymerization reactions non-negligible, especially at high temperatures. Great effort is dedicated to the development of catalysts that can ensure good polymerization control in reasonable conditions. In the following Section, ROP techniques relevant to this Thesis are briefly summarized: the anionic ROP (AROP) of lactide mediated by amidine and guanidine catalysts, and cationic ROP (CROP) of 2-oxazolines.

2.2.1 Organocatalyzed AROP of lactide

Controlled synthesis of polylactide have been traditionally carried out in the presence of organometallic catalysts, in particular metal (Sn, Al, lanthanides) alkoxydes.[52] Contamination of the final products by heavy metals is particularly problematic for drug delivery applications, due to their potential toxicity. In the last 15 years, metal-free alternative catalysts for controlled ROP of lactide, glycolide, caprolactone and other relevant cyclic esters, lactones and carbonates have been sought. Their advantages include commercial availability and low cost, mild reaction conditions and control over molecular weight, chain-end fidelity and chain architecture. Cyclic monomer activation by nucleophilic compounds like 4-(dimethylamino)pyridine (DMAP), phosphines, N-heterocyclic carbenes (NHC)[53] and other amines[54] have been proposed. Another approach to ROP relies on H-bonding activation

of *i*) an alcoholic initiator by an H-bond acceptor, *ii*) an alcoholic initiator and the monomer by a bifunctional catalyst with H-bond accepting and H-bond donating moieties, or *iii*) an alcoholic initiator by an H-bond acceptor and the monomer by an H-bond donor cocatalyst (Scheme 2.1). Typical H-bond donor groups are: thiourea, alcohol, phenol, amide, sulfonamide, protonated amine, guanidine and amidine, and phosphorylated moieties. H-bond acceptors are cyclic amidines and guanidines. Catalysts may form one or multiple H-bonds – generally weak or of moderate strength – with reactants. All organocatalysts presented are water resistant, but water (even in small quantities) competes with H-bonding activity with catalysts, and can act as an initiator of polymerization.

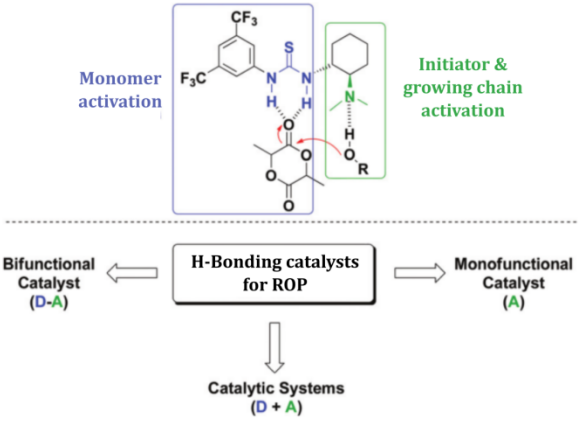

Scheme 2.1 – H-bonding activation pathways for organocatalyzed ROP.[55]

An overview of H-bonding catalysts for ROP are represented in Figure 2.8. Basic cyclic amidines like DBU (amidine), MTBD (guanidine), and phosphazenes are typical monofunctional H-bonding acceptors. In particular, DBU allows the preparation of P(L-LA) with molecular weights up to 85 kDa within 2 h at room temperature in chloroform (Đ = 1.05–1.08), and is also able to polymerize several phosphoesters in the same conditions, although control is lost when monomer conversion exceeds 50%.

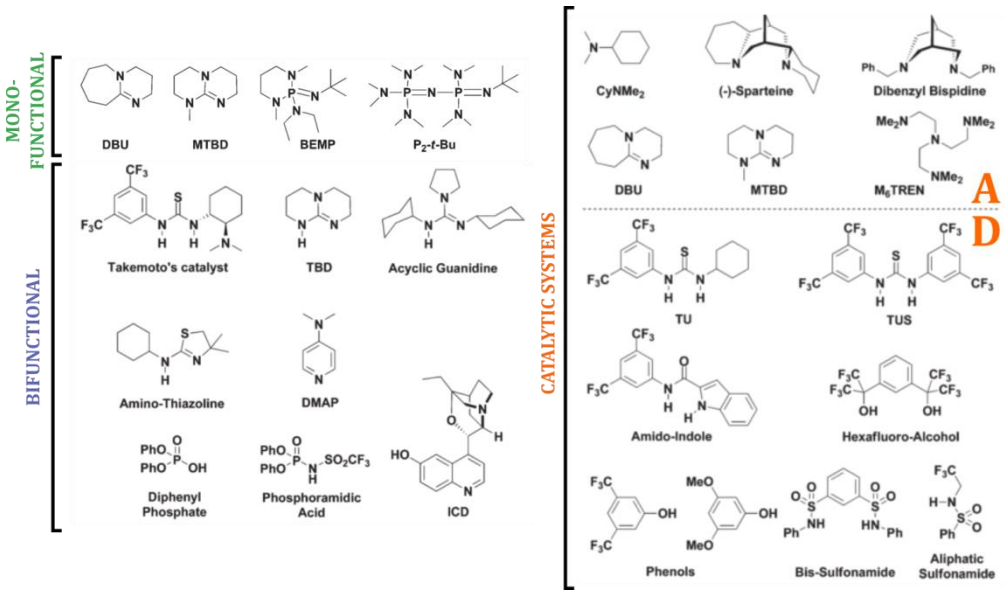

Figure 2.8 – Overview of monofunctional, bifunctional non-ionic H-bonding catalysts for ROP (left). Catalysts systems constituted by H-bond acceptors (A) and donors (D) are shown on the right.

Bifunctional catalysts carry both H-bond donor and acceptor moieties, and are therefore able to activate both monomer and initiating alcohol by forming complexes with both reactants. They have no tendency towards self-aggregation, and possess stereogenic centers that are able to control the stereochemistry of growing lactide chains. This class comprises cyclic and acyclic guanidines, DMAP, Takemoto's catalyst, sulfonic, phosphoric and phosphoramidic acids, and amino-thiazolines.

Finally, co-catalyst systems involve an H-bond donor (D) and an H-bond acceptor (A) molecules binding to monomer and initiator but not to each other. This limitation is balanced by facile synthetic or commercial access, and the possibility to combine different D and A molecules to tailor their activity. The first proposed catalytic system was constituted by thiourea (TU) and tertiary amines,[56,57] which was found to be able to polymerize lactide to 99% conversion in < 24 h with a final polydispersity of 1.06 and absence of transesterification reactions. DBU was used as cocatalyst of TU and commercial substituted phenols of various monomers, including LA, CL, VL, and some phosphoesters. This system also yielded relatively controlled block PVL-*b*-PLA and PCL-*b*-PLA copolymers (Đ = 1.22 – 1.39).[58]

DBU was also used as a cocatalyst in a ionic (protonated DBU)-(deprotonated benzoic acid) complex for the controlled polymerization of lactide.[59]

Along with its H-bond acceptor activity, DBU also feature a nucleophilic character that can interact with lactide monomers by nucleophilic attack on ring carbonyls; this aspect has only

been fully elucidated in 2016 by Sherck and coworkers, and will be further discussed in Chapter 4.[60]

2.2.2 CROP of 2-oxazolines

Oxazolines are 5-membered cyclic imines that are typically bearing substituents on their 2 or 4 position. Whereas polymerization of 4-oxazolines is difficult, ring opening of 2-oxazolines in a controlled fashion has attracted considerable scientific interest, particularly for their application in biomedical context (see introductory overview in Chapter 5). In this case, ring strain relaxation has a negligible role on ROP thermodynamics, as the polymerization is mainly driven by the isomerization of the cyclic amine to a more stable tertiary amine.[61] A simplified polymerization scheme is shown in Scheme 2.1.

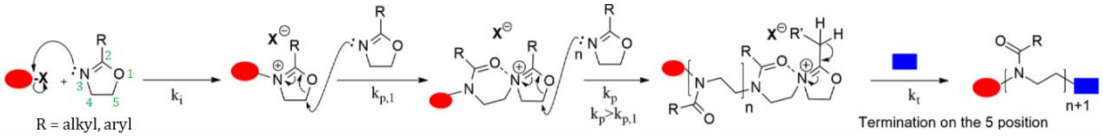

Scheme 2.2 – General scheme of CROP of 2-oxazolines. Reproduced from: Verbraeken, B.; Monnery, B. D.; Lava, K.; Hoogenboom, R. *Eur. Polym. J.* **2017**, *88*, 451–469.

ROP is initiated by nucleophilic attack of the cyclic imino ether on an electrophilic initiator, with the release of a negative counterion. Unless very reactive initiators (such as triflates) are used, this step only occurs at high temperatures (> 80 °C). Though a wide variety of initiators have been developed, the most commonly used are tosylates (in particular, methyltosylate), triflates and nosylates. α-end functionalities can be introduced during the initiation step by using suitably substituted initiators; notable examples are propargyl tosylate for the incorporation of a "clickable" alkyne moiety,[62] α –bromoisobutyrylamide for orthogonal polymerization of vinyl monomers by ATRP,[63] and multifunctional initiators for star-polymer formation.[64]

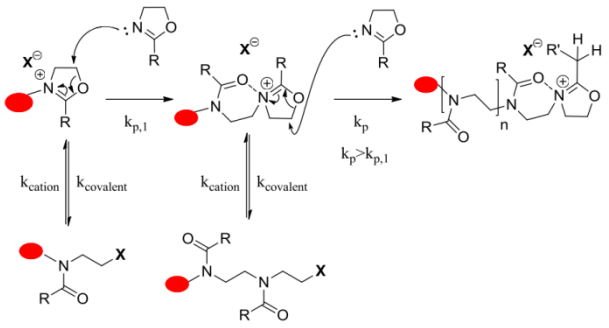

Scheme 2.3 – Propagation step of CROP of 2-oxazolines. Reproduced from: Verbraeken, B.; Monnery, B. D.; Lava, K.; Hoogenboom, R. *Eur. Polym. J.* **2017**, *88*, 451–469.

Propagation is a two-step process: initially, the first monomer attacks the species generated by the initiator. This is the rate-determining step, as kinetics are rather slow. After this first event, propagation kinetics accelerate considerably, due to an intra-molecular dipole-ion polarization effect that stabilizes the much more reactive cationic intermediate, which is almost exclusively responsible for propagation. The initiator counterion X^- plays an important role in stabilizing the cationic oxazolinium species, as does the solvent: thanks to its polarity, acetonitrile is used almost invariably, often at temperatures above its boiling point in microwave reactors.[65] Statistical and gradient copolymers can be obtained with good control by mixing differently substituted 2-oxazolines in this phase, or the pseudo-living cationic conditions can be exploited by adding the second monomer after complete consumption of the first, to obtain block copolymers.[66,67] Chain transfer reactions can occur, although only to a small extent, as they are much slower than propagation. The main side reaction is β-elimination with the formation of enamine ether-terminated "dead" polymer and a proton-initiated oxazolinium cation; the enamine can perform a nucleophilic attack on propagating chains causing branching.

Due to the stability of oxazolinium species, the termination step may also require rather harsh conditions (60-80 °C). Water has the tendency to induce termination on the kinetically controlled 2 position; in contrast, carboxylates, nitrogen-based compounds, and methanolic potassium hydroxide tend to terminate on the thermodynamically controlled 5-position (Scheme 2.4).

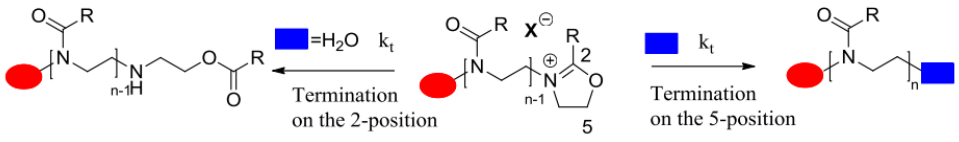

Scheme 2.4 – Termination step of CROP of 2-oxazolines. Reproduced from: Verbraeken, B.; Monnery, B. D.; Lava, K.; Hoogenboom, R. *Eur. Polym. J.* **2017**, *88*, 451–469.

ω-Functionalization can be incorporated by choosing a suitable terminating agent. Common terminating agents are nitrogen compounds (ammonia and primary, secondary, and tertiary amines, which yield primary, secondary, tertiary amine and quaternary ammonium[68] end groups, respectively), carboxylate derivatives and sodium thiolates.

CHAPTER 3

PS-*b*-PDMA self-assembly from DMF

Poly(N,N'-dimethyl acrylamide) (PDMA), to the best of our knowledge, has not been throughly investigated as a hydrophilic block for amphiphilic block copolymer self-assembly. Due to its excellent water-sorbing properties, PDMA has primarily found applications in the fabrication of hydrogels. Often randomly copolymerized with other thermosensitive and pH-sensitive acrylamides, reports of chemically and physically crosslinked PDMA hydrogels for tissue engineering and drug delivery are abundant in the literature.

Hillmyer's group has used PDMA as a middle block between PLA and PS in PLA-*b*-PDMA-*b*-PS triblock copolymers for the fabrication of nanostructured materials.[69,70] They found the suitable triblock composition for the formation of a PLA cylindric phase separated from the surrounding PS matrix by PDMA domains in bulk. Since PDMA is stable under basic hydrolytic etching conditions, sacrificial PLA could be etched away exposing ordered hollow nanochannels of highly controlled size coated with hydrophilic PDMA. PDMA amidic side groups were then hydrolyzed in acidic conditions to yield P(DMA_x-*co*-AA_{1-x}) blocks with tunable composition. This procedure allows for a good control over the fraction of carboxylic acid moieties present on the nanochannel surface, which can be used for further functionalization (e.g. by carbodiimide-mediated coupling).

Research by Stenzel and coworkers[71] focused their investigation on the blocking ability of two classes of PS macroCTAs upon chain-extension with DMA. Despite the presence of some tailing in GPC curves of the synthesized PS-*b*-PDMA diblocks towards lower molecular weights, relatively good control was achieved when a trithiocarbonyl-bearing CTA was employed (PDI = 1.2 ÷ 1.4). PS-*b*-PDMA copolymers of different composition and molecular weight were then used to cast films from DCM under a flux of humid air. The interaction between PDMA blocks and air-borne water droplets induced the formation of hexagonally-packed regular pores. In this case, the main cause of ordered pore formation lay in the balance between water droplet surface tension reduction by the polymer's stabilizing ability, and PDMA solvation; in other words, copolymers were considered as surfactants rather than self-assembling agents.

More recently, PDMA was used as a water-soluble macroCTA agent for the polymerization of diacetone acrylamide (DAAM) in aqueous PISA conditions. After crosslinking, different nanostructure morphologies were achieved by varying hydrophobic

PDAAM's degree of polymerization, but, interestingly, open lamellae were the predominant morphology over a wide range of synthetic conditions.[72] Figg *et al*.[73] also employed a PDMA macroCTA and DAAM as hydrophobic block, and focused on the effect of the core-forming block's degree of hydrophobicity, which was tuned by random copolymerization of DMA and DAAM monomers in different ratios. They observed a transition from spherical micelles to worms and then to vesicles with decreasing core hydrophobicity (at constant DP). Moreover, a relatively large area of stability for worms with high aspect ratios was found. It should be noted that both open lamellae and long worms are seldom encountered in amphiphilic diblock copolymer self-assembly.

PS-*b*-PDMA nanoparticle formation in water by gradual solvent switching has been a research topic in our group for a few years. Extensive and systematic investigation on the self-assembly of PS-*b*-PAA was conducted by Eisenberg and coworkers, who helped lay the foundations of this field's methodology (and terminology).[74–83] PAA's (partial) anionic nature enhances its incompatibility with aprotic aromatic PS, granting a regime of strong separation between the two polymeric domains that helps identify the rules of amphiphilic self-assembly. In order to finely gauge the effect of block immiscibility on self-assembly, our group opted for a hydrophilic block somewhat similar in chemical structure to PAA but with a higher degree of compatibility with PS. DMA is still fairly polar and highly hydrophilic, but it's aprotic and pH insensitive. PS-*b*-PDMA undergoes no phase separation in bulk at certain molecular weights and compositions,[69] an indication of a reduced interaction parameter χ.

Predominantly hydrophilic PS_{105}-*b*-$PDMA_{817}$ self-assembled in water from DMF yielded monodisperse 'star-like' micelles with small, solid cores (D_H = 125 nm, D_{core} = 20 nm). Time-resolved photoluminescence spectroscopy revealed that the PS cores could transition to their glassy state after a certain water content was reached, in spite of their nanometric size and of the presence of a non-negligible amount of DMF.[84] Predominantly hydrophobic PS_{62}-b-$PDMA_{10}$, on the other hand, yielded spherical particles whose size (D ~ 150 nm) largely exceeded what can be reasonably expected from these systems if a simple micellar morphology is assumed.[85] When indented with an AFM cantilever in force spectroscopy mode, single particles crumbled into smaller spheres, exposing a hierarchical organization of presumably simple micelles coalesced into larger aggregates, in a pomegranate-like fashion.

The suitability of PS-*b*-PDMA nanoparticles for drug delivery applications was demonstrated by cytotoxicity assays on human umbilical vein endothelial cells (HUVEC) and macrophages, which showed no major toxicity of PS_{241}-*b*-$PDMA_{86}$ nanoparticles (D = 50 nm) even in high concentrations (500 ug/mL).[86] Furthermore, the nanoparticles were able to

cross a cellular model of the highly selective blood-brain barrier (BBB) after functionalization with a lipoprotein peptide. Transportation of particles or molecules across the BBB depends, among other things, on particle size and surface charge: particles or molecules with a net negative or positive charge on their surface are more often blocked by the BBB.[87] Moreover, protic groups favour the formation of hydrogen bonds with opsonins and other proteins responsible for foreign object clearance by the organism. Aprotic, neutral PDMA has therefore more potential as 'stealthy' drug carrier coating than PAA. In fact, PDMA can be found ever more frequently in polymer-protein conjugates, drug-delivery nanocarriers and encapsulants for bioactive metallic and oxide nanoparticles.[88–90]

In this Chapter, PS-*b*-PDMA synthesis and self-assembly is described. First, a systematic approach was used to map the obtained morphologies as a function of copolymer composition and molecular weight. Then, in-depth microscopy characterization was performed on classes of complex morphologies that were not previously described, especially in the predominantly hydrophobic composition range. Finally, time-resolved spectroscopy of a luminescent molecular rotor was used to probe the *in situ* viscosity of the particles during formation.

3.1 Experimental

Materials

Dichloromethane (DCM), methanol, N,N'-dimethylformamide (DMF), tetrahydrofuran (THF), dry 1,4-dioxane, deuterated chloroform ($CDCl_3$) were purchased from Sigma Aldrich and used as received. Styrene and N,N'-dimethylacrylamide (DMA) were purchased from Sigma and distilled before use to remove the inhibitor. 2,2′-Azobis(2-methylpropionitrile) (AIBN) was purchased from Sigma Aldrich and crystallized from cold methanol. Ultrapure and deionized water were obtained from Direct-Q5 system (Millipore, Italy). 3-(Benzylsulfanylthiocarbonylsulfanyl) propionic acid (BTP) was synthesized as described in the literature[71].

3.1.1 Synthesis of poly(styrene) macro chain transfer agents (PS macro-CTA)

Four PS macro-CTAs with different molecular weights were synthesized as follows. In a typical reaction, styrene monomer (13.6 g, 131 mmol), BTP (0.356 g, 1.31 mmol) and AIBN (0.0215 g, 0.131 mmol) were added to a 100 mL Schlenk flask. After degassing by three freeze-pump-thaw cycles, the flask was filled with Argon and put in an oil bath at 110 °C under magnetic stirring. After 24 h, the reaction was quenched with liquid nitrogen, and excess monomer was distilled away at reduced pressure. The polymer was then redissolved in

DCM, precipitated twice in methanol and filtered. The lightly yellow solid was finally dried in vacuo for several hours. The average molecular weight, and hence number *n* of repeating styrene units, was determined by GPC in THF calibrated with PS standards. When higher molecular weights were targeted, the styrene-to-BTP ratio was increased accordingly.

3.1.2 Synthesis of poly(styrene)-*b*-poly(N,N'-dimethylacrylamide) (PS-*b*-PDMA)

The PS macroCTA was left under vacuum in a 100 mL Schlenk flask for one hour. DMAwas thoroughly degassed and added to the flask, along with AIBN as initiator and 35 mL anhydrous 1,4-dioxane as solvent. The monomer-to-macroRAFT agent ([M]/[T]) and macroRAFT agent-to-initiator ([T]/[I]) molar ratios were kept at 500 and 10 respectively. The solution was further degassed by three freeze-pump-thaw cycles, then heated in an oil bath at 60 °C under magnetic stirring and allowed to react in argon atmosphere. The targeted molecular weight of the PDMA block was achieved by varying the reaction time. The reaction was quenched in liquid N_2, the solvent and excess monomer was removed by low pressure distillation. The samples were then dried in rotary evaporator. The lightly yellow solids obtained were dissolved once again in THF, purified by dialysis (MWCO of 3500 Da) against MilliQ water for 48 hours, and freeze-dried.

3.1.3 Nanoparticle fabrication by gradual solvent switch method

Typically, 1 mL of copolymer solution (20 mg/mL) in the organic solvent of choice was stirred until completely clear and homogeneous. MilliQ water was added dropwise at the fixed rate of under magnetic stirring until a large excess (4:1 H_2O:organic solvent by volume) was reached. The resulting turbid dispersion was dialyzed (3500 MWCO) against MilliQ water for up to 48 h. Variations to this protocol are detailed in the main text.

3.1.4 Copolymer characterization

^{1}H and ^{13}C NMR spectra were recorded using a Bruker AMX-500 spectrometer operating at 500 and 125.70 MHz, respectively. Molecular weight distributions and polydispersity indexes were determined by Gel Permeation Chromatography (GPC) using a WATER 1515 isocratic HPLC Pump, a WATER 2414 refractive index detector, four Styragel columns (HR2, HR3, HR4, HR5). Samples were dissolved in THF and their chromatograms recorded with a flow of 1.0 mL/min at 35 °C. A calibration with polystyrene standards (Sigma-Aldrich) was used. Thermal properties were determined by Differential Scanning Calorimetry (DSC) using a Mettler Toledo DSC 1 instrument with a heating and cooling rate of 20 or 10 K/min under nitrogen gas flow (80 mL/min).

3.1.5 Nanoparticle characterization

NP size and size distributions were recorded at 25 °C on a Malvern Zetasizer equipped with a continuous wave 1 mW He-Ne laser operating at 632.8 nm and an avalanche photodiode detector, Q.E. > 50% at 633 nm, placed at 173° with respect to the incident beam. Reported data is the average of at least three different measurements. Samples were analyzed at a concentration of ~1 mg/mL. AFM imaging and force spectroscopy were carried out with a JPK NanoWizard (JPK Instruments, Berlin, Germany) with closed loop scanner using silicon cantilevers with a resonance frequency of 70 kHz and a nominal spring constant of 1.7 N m^{-1} (OMCL-AC240TS, Olympus, Tokyo, Japan). Real spring constants of individual cantilevers were determined using the thermal noise method. 10 µl of colloidal dispersion was casted on freshly cleaved mica, and was left to dry under a fume hood for several hours. Imaging was performed in tapping mode under ambient conditions. Force spectroscopy was performed on single particles, either isolated or on the edge of an aggregate. The cantilever tip was centered on top of the particle, and force-versus-distance curves with increasing applied loads were recorded. After every measurement, the particle was imaged again in order to detect any indentation or deformation caused by the tip. Reference force curves were taken on the mica substrate to determine the cantilever deflection sensitivity. Scanning Electron Microscopy (SEM) analysis was performed on a Vega TS5136 XM Tescan microscope. The electron beam excitation was 30 kV at a beam current of 25 pA, and the working distance was 12 mm. In this configuration the beam spot was 38 nm sized. Prior to SEM analysis, samples were gold-sputtered. Cross sectioning and SEM imaging of sectioned nanoparticles were carried out in a FEI Nova 600 Nanolab Dualbeam Focused Ion Beam/SEM system. A 10 µl droplet of the dispersion was casted on a silicon wafer and left to dry overnight under a fume hood. Individual nanoparticles were selected and coated with a 1 µm thick layer of platinum. They were then cross sectioned by removing half or successive slices of a particle with Ga+ ion beam at a beam current of 100 pA followed by a polishing step of the cut with a beam current of 10 pA. Samples of NP dispersions after dialysis were vitrified by applying a 3 µl aliquot to a previously glow-discharged 200-mesh holey and Quantifoil carbon grids (Ted Pella, USA). Grids were blotted and then plunged into liquid ethane using a FEI Vitrobot Mark IV (FEI Company, the Netherlands). The samples were imaged using a Tecnai G2F20 microscope (FEI Company, the Netherlands) equipped with a Schottky Field Emission electron source, a US1000 2kx2k Gatan CCD camera and operating at an acceleration voltage of 200 kV. The cryo-tomographic (CET) series were collected tilting the vitrified sample over ±60°, with a tilt step of 2°. Computation of tomogram was carried out with the IMOD28 software package. Segmentation and 3D visualization were done using the Amira package

(FEI Visualization Science Group, Bordeaux). The cryo-EM and CET imaging were performed under low dose conditions (60-80 electron/A2). Intensity profiles on tomogram slices have been obtained using MatLab (MATLAB 6.1, The MathWorks Inc., Natick, MA, 2000).

3.2 Results and discussion

Amphiphilic PS-*b*-PDMA copolymers were synthesized by RAFT chain extension of PS macro-CTAs of different molecular weights with DMA (Scheme 3.1). Trithiocarbonylthio-based RAFT agent BTP provided a good control over block formation: all GPC traces were fairly symmetrical and showed a rigid translation of the curve to higher molecular weights, and copolymer polydispersity was not dramatically affected by chain extension (Table 3.1). PDI values are in agreement with those reported by Wong et al.[91] It should be noted that better control over copolymerization (i.e. lower PDIs) was achieved by others[69] with DDAT as CTA; however, our goal was to avoid any effect on self-assembly caused by anything other than the block copolymer and the solvent/non-solvent mixture used. The aliphatic dodecyl chain on DDAT, having unfavorable interactions with both PDMA and PS, could have a disrupting effect on the process, especially for lower copolymer molecular weights. BTP, on the other hand, bears a benzyl moiety on the R group, which acts as an additional styrene unit at the block copolymer chain end, and a short-chain carboxylic acid on the Z group, which will be closest to the hydrophilic block and will therefore be solvated.

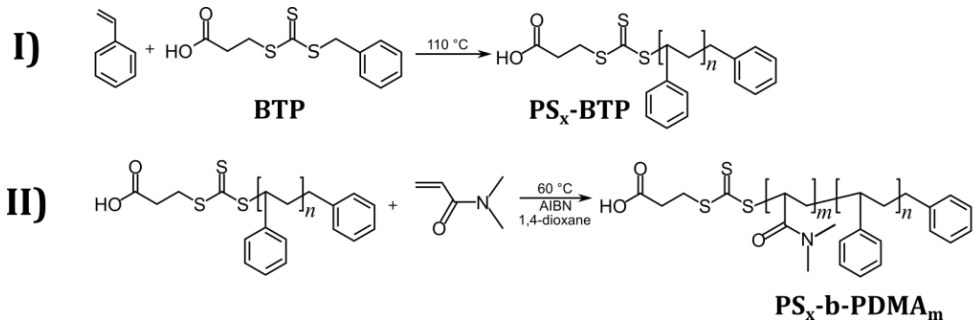

Scheme 3.1- Reaction scheme for the polymerization of PS-*b*-PDMA sample set by RAFT.

Due to its amphiphilic nature, copolymer purification by precipitation in a non-solvent led to a significant loss of sample due to the formation of stable dispersions instead of solid sedimentation. For this reason, polymerization solutions were dialyzed against water for up to 48 hours; no peaks associated with DMA monomer or solvent was detected by ^{1}H-NMR of

freeze-dried samples. The number of repeating DMA units *m* was determined by ^{1}H-NMR ($CDCl_3$) using the following equation:

$$m = \frac{\left[(I_{b+c+d} + I_a + I_e) - I_f\right]}{9} \cdot n \quad (1)$$

where *n* is the number of macroCTA's repeating PS units determined by GPC calibrated with PS standards, and I_x are the integrals defined in Figure 3.1.

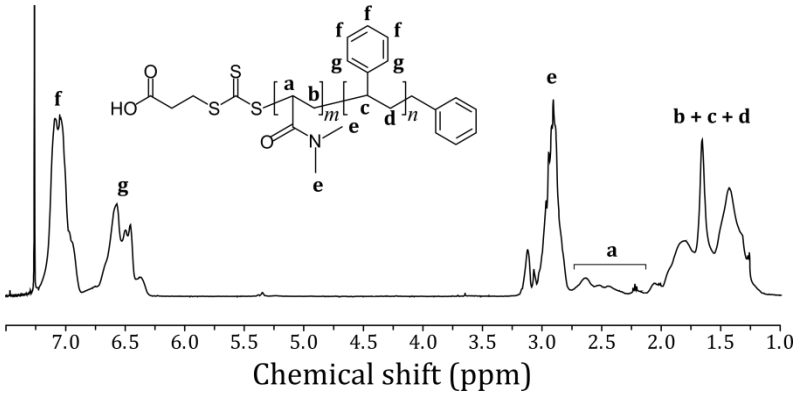

Figure 3.1 - ^{1}H-NMR spectrum of a representative PS-*b*-PDMA sample in $CDCl_3$.

Table 3.1 - Molecular characteristics of PS-*b*-PDMA samples. Number m of repeating DMA units were calculated by ^{1}H-NMR (equation (1)). (a) Polydispersity indexes Đ and weight-average molecular weights obtained by GPC. (b) Glass transition temperatures measured by DSC at 20 K/min. (c) PDMA volume fraction calculated using ρ_{PDMA} = 1.21 g/cm^3 and ρ_{Sty} = 1.04 g/cm^3.[69]

	PS_n-BTP			**PS_n-*b*-$PDMA_m$**				
	M_w[a] (g/mol)	***Đ*[a]**	**$T_{g,PS}$[b] (°C)**	**M_w[a] (g/mol)**	**f_{PDMA}[c]**	***Đ*[a]**	**T_g,[b] (°C)**	
PS_{62}-*b*-$PDMA_{173}$	10200	1.06	94	15200	0.70	1.40	119	
PS_{81}-*b*-$PDMA_{10}$	8000	1.13	95	10400	0.09	1.22	90	
PS_{81}-*b*-$PDMA_{17}$				10900	0.15	1.22	53	
PS_{81}-*b*-$PDMA_{35}$				12500	0.26	1.23	95	119
PS_{97}-*b*-$PDMA_8$	10000	1.15	98	10900	0.06	1.13	95	
PS_{97}-*b*-$PDMA_{109}$				10500	0.48	1.13	98	122
PS_{97}-*b*-$PDMA_{153}$				20600	0.56	1.36	95	123

PS_{97}-*b*-$PDMA_{229}$				26600	0.66	1.38	125	
PS_{97}-*b*-$PDMA_{342}$				35000	0.74	1.23	125	
PS_{241}-*b*-$PDMA_{73}$	25000	1.12	103	26000	0.20	1.15	98	
PS_{241}-*b*-$PDMA_{86}$				34600	0.23	1.17	98	
PS_{202}-*b*-$PDMA_{84}$	21000	1.34	104	22000	0.25	1.42	104	121
PS_{202}-*b*-$PDMA_{115}$				29700	0.32	1.40	104	122
PS_{202}-*b*-$PDMA_{164}$				34100	0.40	1.53	125	
PS_{202}-*b*-$PDMA_{233}$				36800	0.49	1.46	124	
PS_{394}-*b*-$PDMA_{38}$	41000	1.13	105	50800	0.06	1.24	105	
PS_{394}-*b*-$PDMA_{75}$				54700	0.14	1.14	105	
PS_{394}-*b*-$PDMA_{125}$				58900	0.21	1.11	105	121
PS_{394}-*b*-$PDMA_{405}$				57000	0.46	1.30	125	

DSC of was first performed on the whole sample set at 20 °C/min after copolymer purification. The method comprised of a first heating scan up to 150 °C, a cooling scan, and a second heating scan. Any leftover solvent (i.e. water) evaporates during the first heating scan through the pierced crucible lid, a phenomenon that is recorded by the instrument as a negative peak around the solvent's boiling point. The evaporation peak overlaps with other thermal phenomenon occurring in the same temperature range, preventing the observation and measurement of glass transitions. In particular, since glass transitions of PS and PDMA are close to 100 °C ($T_{g,bulk}$(PS) = 105 °C, $T_{g,bulk}$(PDMA) = 120 °C), they are covered by the broad peak of water evaporation: in fact, due to PDMA's hygroscopicity, even a brief exposure of the dried sample to air causes contamination by a sufficiently large amount of water to negatively affect the measurement. In this phase, glass transitions were therefore measured during the second heating scan. In general, only one glass transition was observed by this method: for copolymers with $f_{PDMA} > 0.5$, a sharp transition close to $T_{g,bulk}$(PDMA); for copolymers with $f_{PDMA} < 0.3$, a sharp transition close to $T_{g,bulk}$(PS). For $0.3 < f_{PDMA}$ 0.5, and high m_{PDMA}, two distinct glass transitions corresponding to the PS and PDMA were visible. In

the same f_{PDMA} range, but with low m_{PDMA}, the glass transition of PDMA occurred at lower temperatures compared to bulk values, and overlapped with that of PS. Overall, it's difficult to assess by DSC alone whether the detection of a single transition means that the two block are not phase separated in bulk. It can safely be said that phase separation does occur in bulk when two glass transitions are observed.

3.3 PS-*b*-PDMA self-assembly from DMF

The self-assembly of all samples into water-dispersed nanoparticles was induced by nanoprecipitation: a 20 mg/mL polymer solution in DMF was kept under magnetic stirring at 350 rpm, and MQ water was added by syringe pump at the fixed rate of 2 mL/h, until a final solvent/non-solvent mixture composition of 1:4 was reached. In all cases, the solutions immediately turned from clear to turbid upon the addition of the first few water drops. Each dispersion was then dialyzed against MQ water in order to remove DMF, and analyzed by DLS and TEM. Selected samples (*vide infra*) were further analyzed by CEM, SEM, AFM and TRPL.

TEM imaging at room temperature provided an overview of nanoparticle morphologies obtained by this procedure (**Figure 3.2**) (PS_{62}-*b*-$PDMA_{10}$ and PS_{105}-*b*-$PDMA_{817}$ were also included to further complete the picture). PS is sufficiently eletron-dense to allow a good contrast even without any staining; on the other hand, PDMA is largely transparent to the electron beam. Hence, in the following images, the dark regions are the PS domains.
Nanodispersions were grouped into 5 clusters based on their predominant morphology: micelles, worms, bilayers, compound micelles and mixed micelles and worms. The basis of such classification lay both on TEM images, which revealed the morphology class, and on DLS, which, when multiple populations with different morphologies were present in a single dispersion, allowed to assess which one was predominant over the other. DLS may fall short when strongly anisotropic particles, like worms, are formed; in these cases, we mainly relied on TEM.

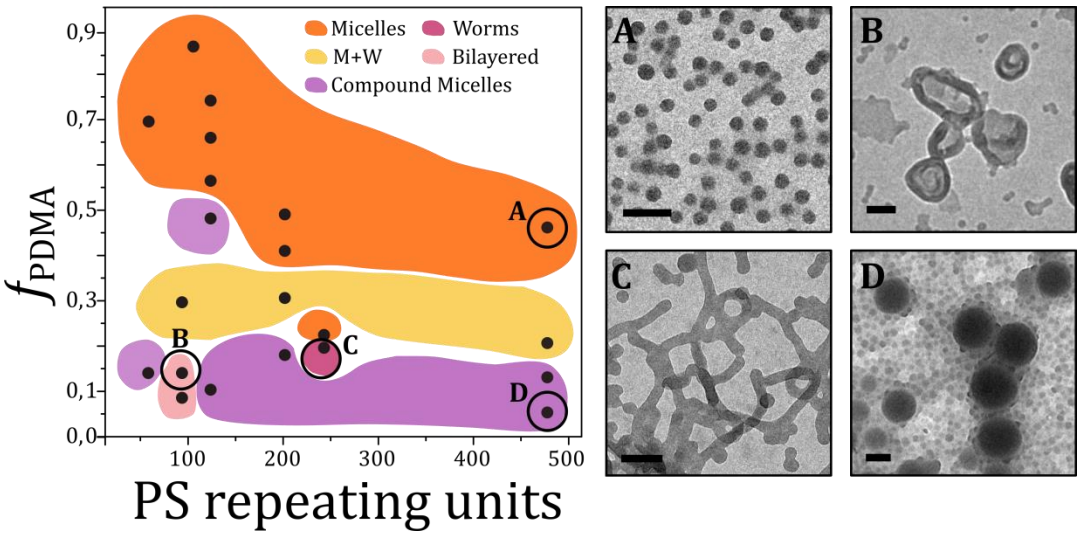

Figure 3.2 - Morphology map of nanodispersions obtained by PS-*b*-PDMA self-assembly from DMF. Micrographs representative of each morphology type are reported on the right: (A) micelles, (B) bilayers, (C) worms, (D) compound micelles. M+W = mix of micelles and worms.

Spherical micelles

For f_{PDMA} > 0.40, fairly monodisperse spherical "star-like" micelles are formed (Figure 3.2(A)). This is expected, as energy reduction due to PDMA solvation compensates the energy increase due chain stretching within PS cores.

For strongly unbalanced hydrophilic systems (f_{PDMA} ~ 1), the elastic energy in the core is expected to be negligible, and the overall micelle free energy only depends on the balance between the corona and the free surface energies. The core radius depends on the length of both blocks, according to:

$$R_{core} \sim a_{core} \left(\frac{N_{core}}{\phi}\right)^{\frac{3}{5}} \left(\frac{\gamma}{K}\right)^{\frac{2}{5}}, \quad (2)$$

[92]

where a_{core} and N_{core} are the core-forming monomer size and number of repeating units, respectively, ϕ is the volume fraction of polymer in the core, which in dense particles (as are most particles obtained experimentally), is ~ 1, and γ is the surface free energy per area a_{core}^2. K is a logarithmic term that includes a_{corona} and N_{corona}, the corona-forming monomer size and number of repeating units, respectively, and results in a shrinking of the core size. The dependency of R_{core} on N_{corona} is often neglected by approximating K to unity, but it proved to be non-negligible for high N_{corona}/N_{core} ratios.

In our case, core radius does not depend on m_{PDMA} for f_{PDMA} > 0.55: for n_{PS} = 97, D_{core} = 20 ± 4 nm, 17 ± 4 nm, and 17 ± 5 nm for m_{PDMA} = 153, 229 and 342 respectively. Conversely, it

does for copolymers with f_{PDMA} < 0.5: PS_{97}-*b*-$PDMA_{109}$ yields micelles with a core diameter of 64 ± 6 nm a sharp increase in size caused by a decrease in m_{PDMA}.

When f_{PDMA} decreases, micelles transition from "star-like" towards "crew-cut" regime, where the hydrophilic corona thickness is lower than the core radius. This condition applies when the hydrophilic volume fraction is close to zero. In this regime, the core radius is related to the copolymer's characteristics as follows:

$$R_{core} \sim \frac{3N_{core}}{\phi} \cdot \frac{a_{core}^2}{a_{corona}} \cdot \left(\frac{\gamma p_{corona}^{1/2}}{C_1 C_2 N_{corona}}\right)^{1/2}, \quad (3)$$

[92]

where C_1, C_2 are numerical coefficients in the order of unity, and p_{corona} is the ratio of the Kuhn segment and size of corona-forming monomers ($p = l/a$). Empirical relations between crew-cut micelle core radii and the repeating units of the two blocks have also been proposed, e.g. for PS-*b*-PAA copolymers:[83]

$$R_{core} \sim N_{PS}^{0.4} N_{PAA}^{-0.15}, \quad (4)$$

where N_{PS} and N_{PAA} are PS and PAA repeating units, respectively.

In our case, compound aggregates were preferred by copolymers with f_{PDMA} < 0.30 over single micelles (see after). Anyway, PS_{81}-*b*-$PDMA_{29}$ is an exception, forming numerous single micelles with a core diameter of 34 ± 5 nm. It should be noted that with an f_{PDMA} of 0.29, these micelles can hardly be considered "crew-cut", and belong to the intermediate region between the two limit conditions

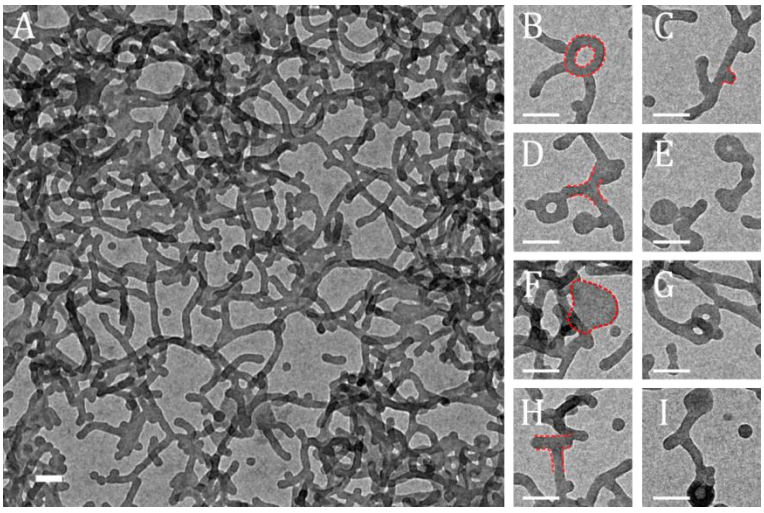

Figure 3.3 - TEM s micrographs of PS_{241}-*b*-$PDMA_{73}$ after dialysis. (A) Overview at low magnification, (B-I) details of morphologic features: Y- (D) and T-junctions (H), closed loops (B), buds (C), worm fusion into lamellae (F).

Worms

PS_{241}-*b*-$PDMA_{73}$ is the only sample whose morphology is prevalently that of elongated worms (Figure 3.3(A)). Their aspect ratio is very variable, but their remarkable feature is the relatively high occurrence of Y junctions and closed loops (Figure 3.3(B–I)). Branched worm structures were predicted[93] and observed[94,95] in nonionic small-molecule amphiphiles in oil/water mixtures, and subsequently reproduced by Jain and Bates[96] in water using poly(butadiene)-*b*-poly(ethylene oxide) (PB-*b*-PEO) copolymers. This 'soft' system organized in remarkably symmetric networks of branched polymer worms, either end-capped with a closed loop or with a spherical 'bulb'. The softness of PB cores was considered responsible for such a high density of branching and for their 'ghost' mirror symmetry. A few years later, Zhang et al.[97] observed similar networks formed by poly(4-vinyl pyridine)-*b*-poly(styrene) (P4VP-*b*-PS) whose P4VP corona was loaded with CdSe nanocrystals. In this case, the core-forming PS block was below its bulk T_g, and the formation of branched worms was promoted by the presence of the nanocrystals, which acted as bridges between individual micelles. Here, we observe a somewhat similar phenomenon (though to a lesser extent of regularity) in the absence of any external 'bridging' agents, and with high T_g core-forming blocks.

Some worm formation is also visible in other copolymers with f_{PDMA} up to ~ 0.30 (Figure 3.4(J)), which may signify that this diblock composition lies on the edge between the range of stability of micelles and worms. However, it is well known that stirring speed affects worm formation, as higher shear stresses cause a higher incidence of micelle-micelle collisions and consequent fusion into cylinders[98]. In our case, stirring speed was kept constant throughout all preparations, so we considered molecular weight and f_{PDMA} the main discriminating parameters. Still, the short PDMA blocks of these predominantly hydrophobic copolymers may have been unable to prevent micelle fusion facilitated by stirring, especially while the solvent mixture composition was such as to allow a fairly high PS block chain mobility. The topic of chain mobility in water-dispersed PS-based nanoparticles is complex and is discussed in Section **Errore. L'origine riferimento non è stata trovata.**.

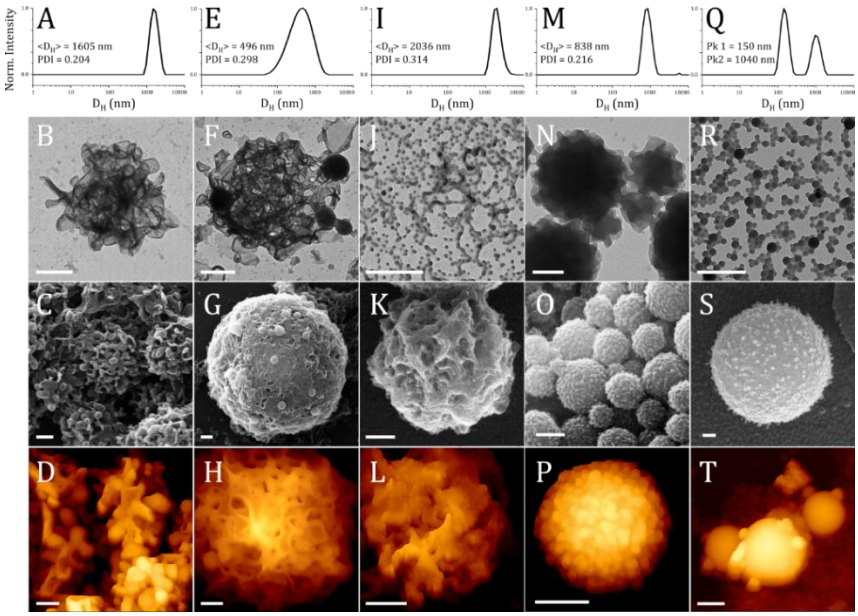

Figure 3.4 - Particle morphology of PS-b-PDMA dispersions after dialysis. (First row) DLS intensity distributions of (A) PS_{81}-*b*-$PDMA_{10}$, (E) PS_{81}-*b*-$PDMA_{17}$, (I) PS_{81}-*b*-$PDMA_{41}$, (M) PS_{97}-*b*-$PDMA_{8}$, (Q) PS_{394}-*b*-$PDMA_{38}$. (Second row) TEM images of (B) PS_{81}-*b*-$PDMA_{10}$, (F) PS_{81}-*b*-$PDMA_{17}$, (J) PS_{81}-*b*-$PDMA_{41}$, (N) PS_{97}-*b*-$PDMA_{8}$, (R) PS_{394}-*b*-$PDMA_{38}$. (Third row) SEM images of (C) PS_{81}-*b*-$PDMA_{10}$, (G) PS_{81}-*b*-$PDMA_{17}$, (K) PS_{81}-*b*-$PDMA_{41}$, (O) PS_{97}-*b*-$PDMA_{8}$, (S) PS_{394}-*b*-$PDMA_{38}$. (Fourth row) AFM height profiles of (D) PS_{81}-b-$PDMA_{10}$, (H) PS_{81}-*b*-$PDMA_{17}$, (L) PS_{81}-*b*-$PDMA_{41}$, (P) PS_{97}-*b*-$PDMA_{8}$, (T) PS_{394}-*b*-$PDMA_{38}$. Scale bar: 500 nm.

Bilayers and compound micelles

Next, we focused on copolymers having hydrophilic volume fractions (f_{PDMA}) lower than 0.30: this compositional range is predicted to allow for the formation of open and closed bilayered morphologies in aqueous environment, since they generate lower elastic strains in the hydrophobic domains compared to spherical micelles. We selected three copolymers with the same PS block length and different f_{PDMA}. The self-assembly behavior of these samples was compared with that of similar values of f_{PDMA} but larger molecular weights.

First, we investigated the self-assembly of copolymers having the same PS block length (DP_{PS} = 81) and different f_{PDMA}. DLS analyses of the aqueous dispersions Figure 3.4(A–C)) reveal the existence of fairly inhomogeneous particles (PDI > 0.2) whose size often exceeds microns. Sonication a few minutes caused no appreciable variation of size distributions, suggesting that the larger particles have a stable morphology that can't be described as the simple coagulation of small particles into larger aggregates.

TEM micrographs of PS_{81}-*b*-$PDMA_{10}$ (Figure 3.4(B)) show micron-sized aggregates of irregularly shaped and seemingly randomly entangled lamellae. Although no stain was

used, PS is generally sufficiently electron dense to provide very good contrast in bright field mode, appearing as dark spots when in compact, micellar/globular form. On the contrary, these aggregates are considerably transparent to the electron beam even for diameters up to 5 µm. This suggests that a rather loose interweave of lamellae extends over the whole particle volume in this size range.

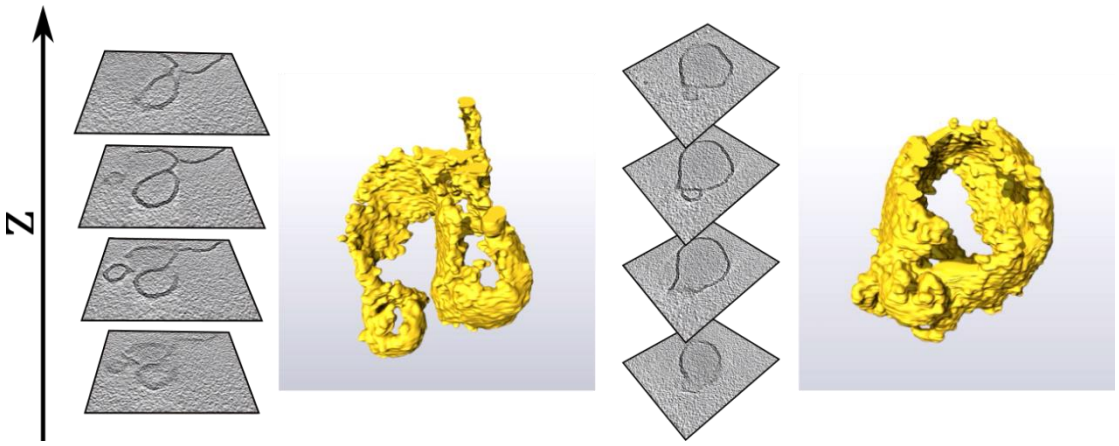

Figure 3.5 - CET slices and three-dimensional reconstruction of two simple bilayered structures (membrane 'clumps') formed by PS_{81}-b-$PDMA_{10}$.

SEM micrographs (Figure 3.4 (C)) and AFM height imaging (Figure 3.4 (D)) show that, at the particle surface, the polymeric membranes fold to form ridges as well as convex vesicle-like protrusions approximately 200 nm in diameter. Nevertheless, the microparticles do not seem to be the product of aggregation of single vesicles, but rather of intertwining of bent lamellae on different hierarchical levels. In fact, smaller, irregularly-shaped membrane 'clumps' coexist with particles of similar constitution but larger size, higher complexity and increasingly spherical shape. In addition, membranes are shared by adjacent particles to form interconnected, hollow systems which can extend over several microns (Figure 3.6(A)). Moreover, a remarkable scarcity of regular spherical vesicles in the dispersion, which would otherwise be expected for this predominantly hydrophobic copolymer, is apparent. Pseudo-vesicular structures are generally oblong and the bilayered wall is often only partially closed. CryoET reveals that these structures are indeed constituted by a single lamella forming a ribbon bending to form a closed loop, rather than polymersomes (Figure 3.5). The bilayer is bicontinuous, i.e. the surfaces on either side of it are continuous.

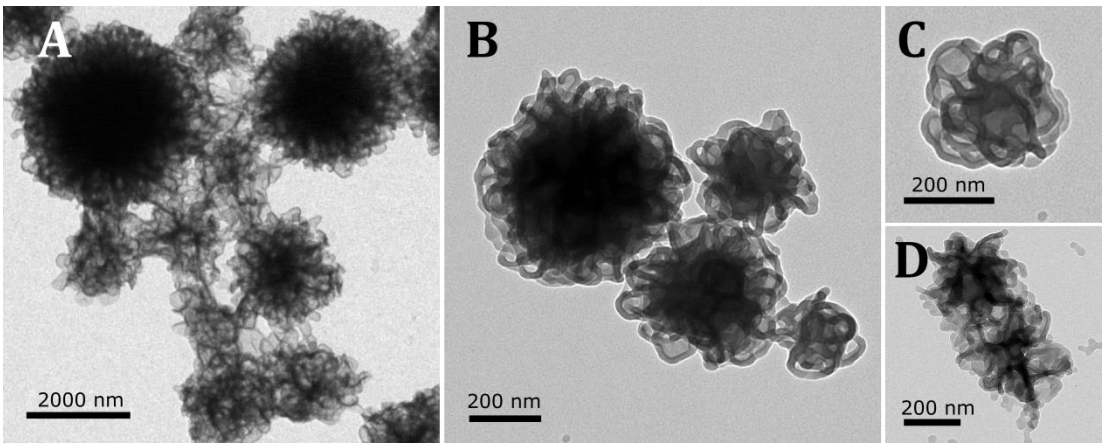

Figure 3.6 - TEM micrographs of PS_{81}-*b*-$PDMA_{10}$ (A) after dialysis, showing membrane sharing between particles, (B, C) in DMF:H_2O solvent mixture, (D) in DMF:H_2O (pH = 4) solvent mixture.

Azzam[76] and Kim[99] have shown that dialysis of organic/aqueous dispersions of self-assembled PS-containing BCPs can induce significant shape deformation in otherwise spherical polymersomes. They reason that the rate of diffusion of organic molecules from the inside to the outside of the vesicle is higher than that of water molecules diffusing from the outside to the inside of the vesicle, due to the presence of the hydrophobic PS constituting the vesicle wall. As long as the concentration of organic solvent in the dispersion is sufficient to swell the PS block, the wall has a high enough mobility to deform under the resulting osmotic pressure. At a certain point, the concentration of organic solvent will be sufficiently low to allow the PS-block to transition to its glassy phase, and the deformed shape becomes irreversible. TEM micrographs of PS_{81}-*b*-$PDMA_{10}$ dispersions before dialysis (i.e. in 1:4 DMF:H_2O mixture) (Figure 3.6) show continuous intact membranes running through the particle and forming closed pockets on its surface, confirming that post-assembly modification has indeed occurred.

In order to observe the inner structure of electron-denser micron-sized particles, we opted for particle sectioning with focused Ga^+ ion beam and imaging with SEM. Given the high polydispersity of the sample, differently sized particles were analyzed. SEM micrographs of 2 µm, 3 µm and 12 µm particles are collected in Figure 3.7(A). All particles have an outer porous crust approximately 500 nm thick, regardless of particle size. This area corresponds to the transparent rim also visible in conventional TEM images. On the contrary, the darker shaded core of the 2 and 3 µm appears denser and more homogeneous. When the particle size increases to 12 µm, the core is revealed to be scattered with pores as well: unlike those found close to the surface, the diameter of these cavities can even reach 1 µm and show a rounder shape, with no sign of deformation. This suggests a collapse of their mostly hollow

architecture due to their larger size. Unfortunately, whether the collapse is induced by the gradual solvent evaporation necessary for sample preparation for SEM or is also occurring in the dispersed state is difficult to determine, since cryoEM is not applicable to particles this large.

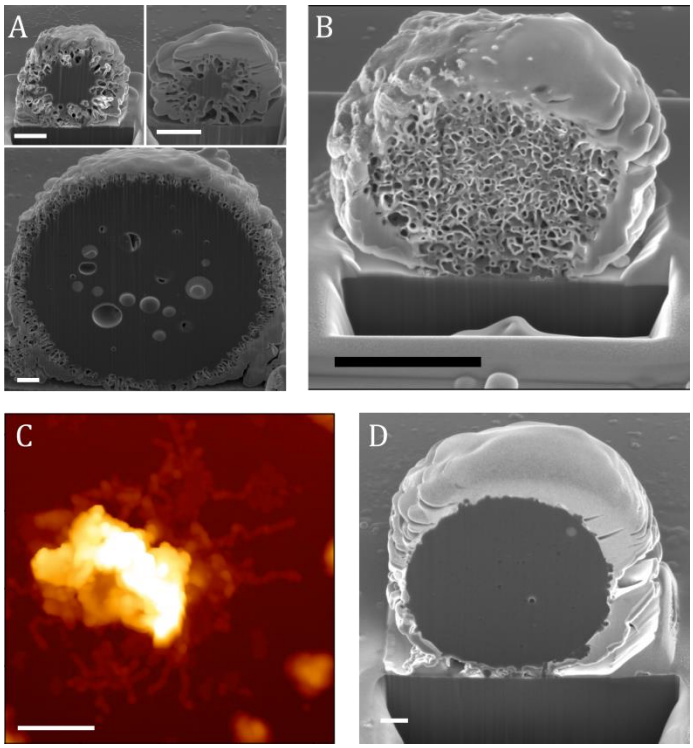

Figure 3.7 - Internal structure of PS-*b*-PDMA microparticles: SEM images after FIB cross sectioning of (A) PS_{81}-*b*-$PDMA_{10}$, (B) PS_{81}-*b*-$PDMA_{17}$, (D) PS_{481}-*b*-$PDMA_{92}$, and (C) AFM height profile of PS_{81}-*b*-$PDMA_{41}$. White scale bar: 500 nm. Black scale bar: 1000 nm.

A relatively small chain extension of the hydrophilic block from 10 to 17 repeating units still yields membranes. Conventional TEM at a moderate magnification shows that almost the whole spectrum of possible morphologies is present: 20 nm micelles, open and bent lamellae, closed vesicles and solid particles (D ~ 300-500 nm) coexist in the sample. This great polydispersity is reflected in the presence of a very broad population in the DLS size distribution (Figure 3.4(B)) that essentially covers the entire region from 100 nm to 1 um (smaller micelles are not detectable due to the substantially higher intensity of light scattered by the larger particles), and a high PDI value of 0.298. However, low magnification SEM images (Figure 3.4) show that spherical microparticles with a corrugated surface are the most common. Membrane ‘clumps’ similar to those observed in PS_{81}-*b*-$PDMA_{10}$ are present, but they tend to form more regular networks with a wider mesh and a higher transparency to the electron beam (Figure 3.4E). The same structure can be discerned in SEM micrographs on the surface of single-standing spherical particles, that bear visible pores of the same size and

appearance of the ‘clump’ mesh (Figure 3.4(H)). They are also similarly decorated with solid particles. The membranes ‘clumps’ can thus be assumed to be precursors of the porous microparticles, or incomplete ones. AFM images (Figure 3.4(K)) provide a more detailed view of the particle surface, constituted by creased membranes over which homogeneous pores are distributed.

In order to investigate its internal architecture, a single particle was selected and imaged by SEM after each removal of 40 subsequent 100 nm-thick slices by FIB (Figure 3.7(B)). The pore structure extends over the whole particle volume in a continuous, yet non-periodic fashion. It bears a strong similarity to the sponge phase, a 3D phase in which two water channels are separated by an uninterrupted, non-ordered polymeric bilayer.[100] This inverse morphology can be assumed by amphiphiles featuring a packing parameter p larger than unity, where p is a dimensionless geometric factor defined by Israelachvili *et al.*[101] as $p = v/a_0 l$ (v is the hydrophobe molar volume, a_0 is the area per chain and l is the hydrophobe length). These microparticles are characterized by a good mechanical stability, showing no change in morphology after lyophilization and redispersion in water (Figure 3.8).

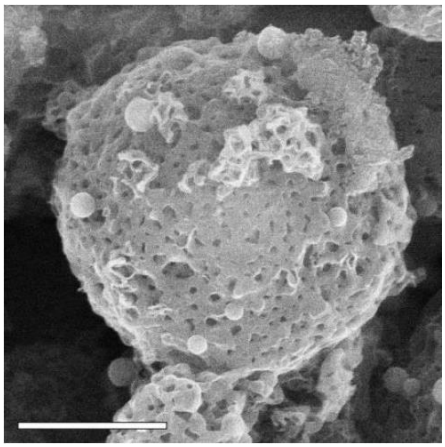

Figure 3.8 – SEM image of freeze-dried PS_{81}-*b*-$PDMA_{17}$ sponge microparticles, showing an intact porous network. Scale bar: 2 μm.

Packing parameter overunity is lost when the number of repeating PDMA units is increased to 41 (f_{PDMA} = 0.29). Micron-sized particles are still formed (Figure 3.4I), but AFM images Figure 3.4L) suggest that they are the product of second-order aggregation of smaller micelles (D_{TEM} = 34 ± 5 nm, D_{AFM} = 57 ± 6 nm). These first fuse together into worms, and finally aggregate in larger ‘yarn-like’ particles (Figure 3.7C). Previous work by our group[85] showed that PS-*b*-PDMA systems have a tendency to organize in hierarchical assemblies. Despite their number, it is evident that the dominant morphology is that of mixed micelles

and worms (Figure 3.4F). According to Israelachvili's theory, the packing parameter *p* is close to ⅓.

Bilayer formation is also prevented by a high molecular weight: PS_{394}-*b*-$PDMA_{75}$, despite having a similar f_{PDMA} as PS_{81}-*b*-$PDMA_{17}$, assembles mainly in spherical solid particles (D_{TEM} = 62 ± 15 nm, D_{AFM} = 120 ± 28 nm). As evidenced by DLS, a minority population of micron-sized particles is also present, and SEM micrographs show some similarity between their surface and that of PS_{81}-*b*-$PDMA_{17}$-based sponges, as indentations similar to pores are visible. The larger particles were also sectioned by FIB, in order to ascertain whether a sponge phase is retained in the larger particles only, suggesting that in these conditions the coexistence of bilayered and micellar structures is (meta)stable. No such structure is visible by subsequent SEM imaging (Figure 3.7(D)), with the exception of a few small pores, suggesting again second-order aggregation of smaller micelles. The aggregation pathway, in this case, does not involve worm formation.

As no individual micelle acting as building block can be clearly discerned in the microparticles by microscopy, AFM in force spectroscopy mode was used to indent the particle and monitor its deformation. A single microparticle was selected, subjected to increasing force loads and imaged again in tapping mode. Applied force loads ranged from 100 to 750 nN.

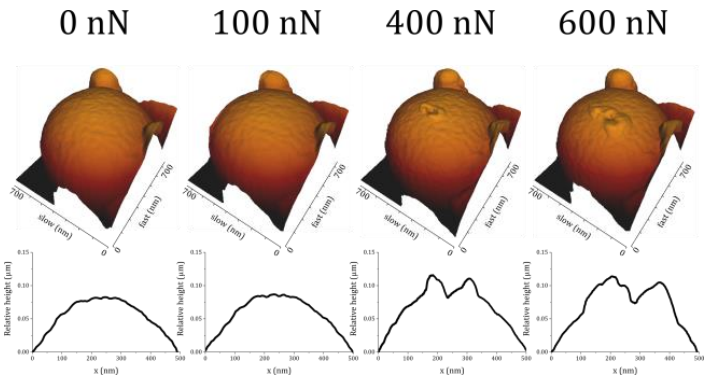

Figure 3.9 – Top: 3D representation of AFM height scans of a single PS_{394}-*b*-$PDMA_{75}$ microparticle before (F = 0 nN) the application of increasing force loads on its summit (cantilever spring constant k = 1.570 N/m). Bottom: height profiles along the particle surface before and after deformation.

Figure 3.9 shows the shape of the indentation caused by the cantilever tip (tip radius: 10 nm) on the particle surface. Some material is displaced and pushed to the outer edge of the approximately 100 nm wide depression, where it forms a ~50 nm-thick ridge. Higher loads lead to a larger amount of displaced material rather than an increase in indentation depth.

This type of plastic deformation is different than that induced by AFM cantilever tips on single PS-based micelles and vesicles, and confirms the hierarchical nature of the aggregate[85].

Interestingly, these second-order aggregates are the predominant morphology assumed by highly hydrophobic PS_{97}-*b*-$PDMA_8$ (f_{PDMA} = 0.06). Despite having such a low f_{PDMA}, and a molecular weight very close to PS_{87}-*b*-$PDMA_{10}$, no bilayers were formed. Single micelles, which very often coexist with other morphologies even in relatively monodisperse dispersions due to their intrinsic thermodynamic stability, were very rare.

3.4 Conclusions and future work

In this Chapter, a complete picture of the previously unreported self-assembly behaviour of PS-*b*-PDMA in water by gradual solvent switching from DMF is drawn. Relatively monodisperse block copolymers with different molecular weights and hydrophilic fraction (f_{PDMA}) were synthesized by sequential RAFT polymerization. A comprehensive sample set was used to prepare nanodispersions which were characterized by DLS and microscopy (TEM, CEM, CET, SEM, AFM). A morphology map is proposed, where predominant morphologies were correlated with copolymer chemical characteristics. For $f_{PDMA} > 0.40$, spherical "star-like" micelles are formed, and micelles/worm mixes are formed by copolymers having $0.25 < f_{PDMA} < 0.40$. For $f_{PDMA} < 0.25$ and low molecular weight, bilayers are formed. In particular, extended lamellae bend and fold to form stable hollow particles with diameters up to several microns. Whereas PS_{81}-*b*-$PDMA_{10}$ (f_{PDMA} = 0.09) organizes in looser lamellar networks, PS_{81}-*b*-$PDMA_{17}$ (f_{PDMA} = 0.15=) yields micron-large porous particles exhibiting a sponge phase which can withstand lyophilisation without any visible structural damage. Higher or lower molecular weight copolymers in the same f_{PDMA} range, have a strong tendency to assemble in compound micellar aggregates.

CHAPTER 4

PEO-*b*-PLA self-assembly from a variety of good solvents

The amphiphilic system poly(ethylene oxide)-*block*-poly(lactic acid) (PEO-*b*-PLA) is one of the most studied for the fabrication of nanoscopic DDSs. PEO's high hydrophilicity, low toxicity, low immunogenicity and capability of preventing opsonization of nanoparticles allowing for improved pharmacokinetics have rendered it the go-to polymeric coating of choice for all kinds of pharmaceuticals, a strategy that is commonly known as PEGylation (from an alternative nomenclature for PEO, poly(ethylene glycol)).[102–105] When a foreign object enters the blood stream, it is quickly covered by a family of proteins, named opsonins, which mark them as target for clearance. The objects can then undergo destruction by phagocytosis or, as in the case of polymeric nanoparticles, be sequestered in mononuclear phagocytic systems (MPS) organs, mainly the spleen and liver[106]. In order to prevent interaction with phagocytes, decades of research has been devoted to finding strategies that would inhibit the adsorption of opsonins on drug carrying particles. Since opsonization occurs more rapidly on hydrophobic[107] and electrostatically charged[108] surfaces, shielding the particle surface with a neutral, hydrophilic layer was recognized as a viable method to slow the process. The effectiveness of PEO in achieving this goal is typically ascribed to the remarkable chain flexibility that is retained in the stretched conformation it assumes in water: when proteins attach to solvated PEO chains, attracted by van der Waals forces, they compress them until they are forced into a collapsed conformation. The higher energy of the collapsed chain state generates a repulsive force that can compensate and finally exceed the attractive force that keeps proteins adsorbed. In order for PEO chains to possess the flexibility necessary for protein repulsion, a minimum molecular weight of 2000 Da is generally required.[109] If this explanation is correct, it is expected that the anti-fouling properties of PEO are more effective when the particle onto which PEO chains are tethered is sufficiently rigid to allow chain compression; PEGylation was predicted to be less efficient on soft hydrogel matrix.[110]

The process of phagocytosis involves the endocytosis of the foreign object and its attempted destruction by enzymatic and oxidative degradation pathways. If these attempts fail, potentially toxic polymer accumulation may occur. Backbone degradable polymers are therefore very interesting as building blocks for DDSs, as they would pose a much lower risk of accumulation in the liver and spleen. The polyesther PLA, used as a hydrophobic block, is

characterized by low toxicity and high biodegradability.[111,112] The main accepted mechanism of degradation is hydrolytic rather than enzymatic, and its rate is enhanced by copolymerization with glycolic acid (GA) to yield poly(lactic-*co*-glycolic acid) (PLGA) systems. Water interacts with PLA by H-bond formation, with one water molecule being able to form one or two hydrogen bonds with lactic acid units, preferentially with carbonyl oxygen atoms.[113] PLA and PLGA systems are able to encapsulate multiple therapeutics by both hydrophobic and hydrogen bonding effects, and pharmaceutical formulations for the treatment of cancer have reached clinical trial.[114,115]

A covalent link between hydrophobic, degradable PLA carriers and 'stealthy' PEO stabilizers prevents the detachment of the hydrophilic coating and provides good DDS stability. PEO-*b*-PLA copolymers couple this advantage with the remarkable morphological variety accessible to self-assembling macromolecular amphiphiles.[116]

Since the shape and size of the NP determine the different interactions with biological systems, including cytotoxicity properties and the ability to cross physiological barriers,[117] it is of extreme importance to have a complete and detailed picture of the PEO-*b*-PLA system behavior to gain predictive power about the morphology of the nanoparticles.[18]

PEO-*b*-PLA NPs were proposed as drug delivery systems for the first time by the group of S.S. Davis in Nottingham,[118] who extensively characterized the NP morphology by several techniques: TEM and NMR[119], viscoelastic measurements,[120] SANS.[121] They describe copolymers constituted by a PEO block with M_w =5 kDa, corresponding to 113 repeating units, and a PLA block with a number of repeating units (m_{PLA}) ranging from 28 to 1540. All these copolymers, dissolved in acetone and assembled in water, form spherical core-shell micelles with a PLA core surrounded by a hydrophilic PEO corona. A clear trend of increasing particle size on increasing the number of PLA repeating units was observed. For copolymers with m_{PLA} up to 417, NP size is solely governed by the length of the PLA block:[119] more precisely, the hydrodynamic radius (R_{hyd}) of the PEO-*b*-PLA NPs scales linearly when plotted versus $N_{PLA}^{1/3}$. These indications of spherical shape were confirmed also by atomistic molecular dynamics simulations:[122] the calculated phase diagram for PEO-*b*-PLA in water, for copolymer concentration in water less than 20% v/v and for the entire range of PLA fraction, predicts only the existence of crew-cut micelles (with large PLA blocks in the core and short PEO blocks in the corona) when the PLA fraction is predominant.

However, Yang et al.[123] later reported a more complex picture for PEO-*b*-PLGA NPs: NP size is dependent on the solvent used for the copolymer dissolution and, on the basis of small angle neutron scattering measurements, the nanoparticles appear to be constituted by 7-9 nm wide PLGA domains interconnected by a complex network of water-swollen PEG

chains. These results, even considering the increased hydrophobicity of PLGA compared to PLA, draw attention to the possibility that more complex nanoparticle morphology can be obtained for PEO-*b*-PLA as well, especially by varying the good solvent used for the dissolution of the copolymer. Other authors describe instead the formation of PEO-*b*-PLA polymersomes,[124–126] typically using THF or dioxane as good solvents.

On the basis of these most relevant papers but also considering the overall literature, to the best of our knowledge, it's difficult to have a comprehensive and self-consistent picture of the self-assembly behavior of PEO-*b*-PLA. In fact each study exploits a different approach for the synthesis of the block copolymer, as well as different methodologies for the self-assembly (e.g.: direct assembly in water, or the use of a good solvent) making a comparison of the results challenging.

Monohydroxyl-terminated PEO has been extensively used to induce ring opening of different lactones to yield linear diblock copolymers with biocompatibility and biodegradability properties suitable for biomedical applications.[127–131~~30–34~~] Whereas $Sn(Oct)_2$ remains perhaps the most commonly used catalyst for alcohol-initiated ROP of lactide and other cyclic esters, transesterification reactions that lead to wider molecular weight distributions and poor control on chain end groups may take place[132]. Although FDA-approved, metal contamination of the final product by residual catalyst can be problematic for drug delivery applications. Organocatalysis has allowed for the development of polymerization protocols that involved minimal reagent cost and waste, thanks to the fact that complete conversion can be achieved in a few hours, at room temperature, and in non-strictly water-free conditions. DBU is a non-toxic,[133] metal-free superbase that allows for remarkable control on molecular weight and molecular weight distributions of different polyesters in mild reaction conditions.[134–136] In this Chapter, synthesis and characterization of a set of PEO_{113}-*b*-PLA copolymers with different compositions obtained by ROP of *rac*-lactide catalyzed by DBU is reported. Their self-assembly into nanoparticles by solvent switching is investigated in depth, with a focus on the effect of the starting non-selective solvent on resulting nanoparticle size and morphology.

4.1 Experimental

Materials

Anhydrous dichloromethane (DCM), acetone (ACT), tetrahydrofuran (THF), dimethylformamide (DMF), 1,4-dioxane (DX), ethyl acetate, toluene, 2-propanol, ethanol and benzoic acid were purchased from Sigma Aldrich and used as received. Poly(ethylene oxide)

monomethyl ether with $\bar{M}_w$=5000 g/mol ($mPEO_{113}$, Sigma Aldrich) was precipitated twice from ethanol, dried by azeotropic distillation from toluene, and stored in a dry nitrogen atmosphere. *rac*-Lactide (*rac*-Lac, Sigma Aldrich) was recrystallized four times from ethyl acetate. 1,8-Diazabicyclo[5.4.0]undec-7-ene (DBU, Sigma Aldrich, 98%) was distilled from CaH_2 under reduced pressure.

4.1.1 Synthesis of PEO_{113}-*b*-PLA copolymers

All reactions were carried out at room temperature under N_2 atmosphere, using dry solvents and reagents. Using PEO_{113}-*b*-PLA_{400} as an example, 0.500 g (10^{-4} mol) of dried $mPEO_{113}$ was dissolved in a Schlenk flask in 1.5 mL of anhydrous DCM. A solution of *rac*-lactide (2.880 g, $2 \cdot 10^{-2}$ mmol) in DCM (2.0 M) was prepared separately and added to the flask. Lastly, DBU (10^{-4} mol, 0.0152 g, 15 µl) was added to the reaction vessel. When different degrees of polymerization of the PLA block were targeted, the ratio of *rac*-lactide to $mPEO_{113}$ was varied accordingly. The resulting solution was allowed to react for 1 hour under magnetic stirring, then quenched by adding 0.028 g ($2.5 \cdot 10^{-4}$ mol) of solid benzoic acid. The resulting polymer was precipitated three times into excess 2-propanol (IPA) to remove any unreacted species and the DBU/benzoic acid salt. The product was then dried under vacuum overnight and stored in sealed screw-capped vials under N_2 at 4 °C.

Degree of polymerization and number-average molecular weight of the PLA block was determined by ^{1}H-NMR from comparison of the PLA methine (δ = 5.10 – 5.28 ppm) and methyl (δ =1.40 – 1.60 ppm) signals with the $mPEO_{113}$ methylene (δ = 3.46 – 3.80 ppm) signal.

Number average molecular weight of PEO_{113}-*b*-PLA_x was calculated from ^{1}H-NMR after purification by comparing integrals d and b (**Errore. L'origine riferimento non è stata trovata.**) according to equation (5):

$$\bar{M}_n = m_{LA} \cdot \frac{I_d}{I_b} \cdot (4N_{EO}) + M_{PEO} \qquad (5)$$

where m_{LA} is lactic acid repeating unit molecular weight (72 g/mol), N_{EO} is the number of ethylene oxide repeating units in $mPEO_{113}$, and M_{PEO} is $mPEO_{113}$ molecular weight (5000 g/mol)

4.1.2 Nanoparticle fabrication by gradual solvent switch method

Typically, 1 mL of copolymer solution (20 mg/mL) in the organic solvent of choice was stirred until completely clear and homogeneous. MilliQ water was added dropwise at the fixed rate of under magnetic stirring until a large excess (4:1 H_2O:organic solvent by volume)

was reached. The resulting turbid dispersion was dialyzed (3500 MWCO) against MilliQ water for up to 48 h. Variations to this protocol are detailed in the main text.

4.2 Results and discussion

4.2.1 Copolymer synthesis and characterization

Synthesis of PEO-*b*-PLA block copolymers was carried out by ROP of racemic lactide initiated by a commercial α-hydroxyl-ω-methyl ether-poly(ethylene oxide) (Mw = 5000 g/mol, PDI_{GPC} = 1.06) (PEO_{113}) (Scheme 4.1). The choice of the racemic mixture instead of one of the pure enantiomeric forms of lactide was motivated by the need to obtain an amorphous PLA polymer, which is better suited to molecule encapsulation compared to crystalline P(L-LA) or P(D-LA).[113] We mainly followed the paper Qian et al.:[132] lactide was recrystallized several times prior to synthesis from toluene or ethyl acetate to minimize acidic impurities and stored at low temperature for two days at most. PEO_{113} was dried by distillation of the toluene-water azeotrope, and immediately used after drying *in vacuo* and redissolution in dry DCM under inert atmosphere. To prevent the formation of DBU-initiated PLA homopolymeric blocks, a fixed [DBU]:[PEO_{113}] ratio of 1 was maintained throughout all polymerizations. PLA block length was modulated by varying the monomer feed and aiming for 100% conversion, which was reached in all cases in ~1 hour. Polymerization quenching was accomplished by DBU poisoning with 2.5 equivalents of benzoic acid.[59] The crude solution was precipitated from excess IPA three times, and the white solid was filtered and dried.

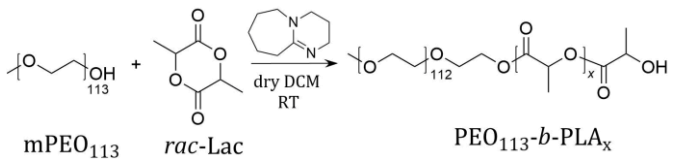

Scheme 4.1 – DBU-catalyzed anionic ring opening polymerization of *rac*-lactide initiated by $mPEO_{113}$.

A representative ^{1}H-NMR spectrum of a typical PEO_{113}-*b*-PLA_x sample is shown in **Errore. L'origine riferimento non è stata trovata.**; the complex signal the lies in the 4.40 – 4.20 ppm region is generated by the terminal methine group on the PLA chain end (1H, f) and the $–CH_2–$ group linking the PEO and PLA blocks (2H, c). In all cases, its integral is consistent with only one terminal group and one linking group per PEO chain.

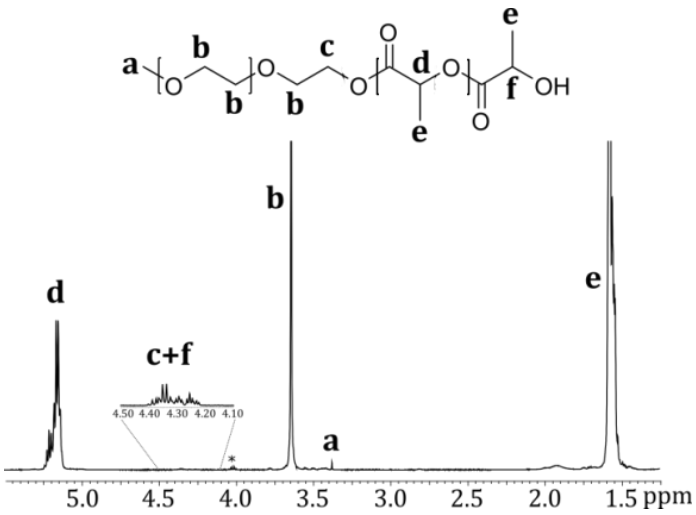

Figure 4.1 – Representative ^{1}H-NMR spectrum of PEO_{113}-*b*-PLA_x ($CDCl_3$, 500 MHz).

Molecular weight distribution PDIs were low and in general accordance with previously reported values, but sometimes asymmetrical (Table 3.1, Figure 4.2). Also, the case of PEO_{113}-*b*-PLA_{1300} was somewhat anomalous: such high PLA degrees of polymerization are generally never achieved by this method. The integral of the (c+f) signal exceeded the expected value by 30%, but this calculation is problematic due to the very low peak intensity compared to main chain protons.

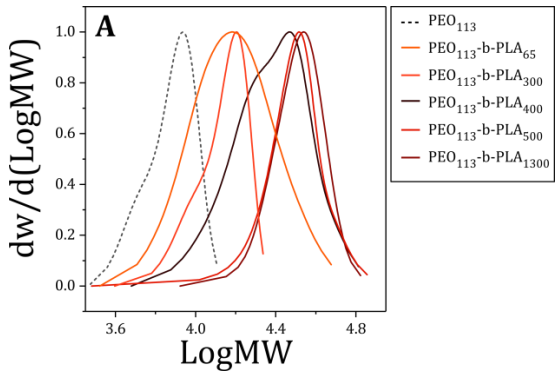

Figure 4.2 – GPC traces of PEO_{113}-*b*-PLA_x samples measured in THF with PS standard calibration.

Despite being used as a catalysts for a few years, comprehensive and quantitative investigation of polymerization mechanisms by DBU and alcohol has been lacking until recently, when Sherck et al.[60] outlined and discussed the main synthetic pathways to ring opening of lactide (Figure 4.3).

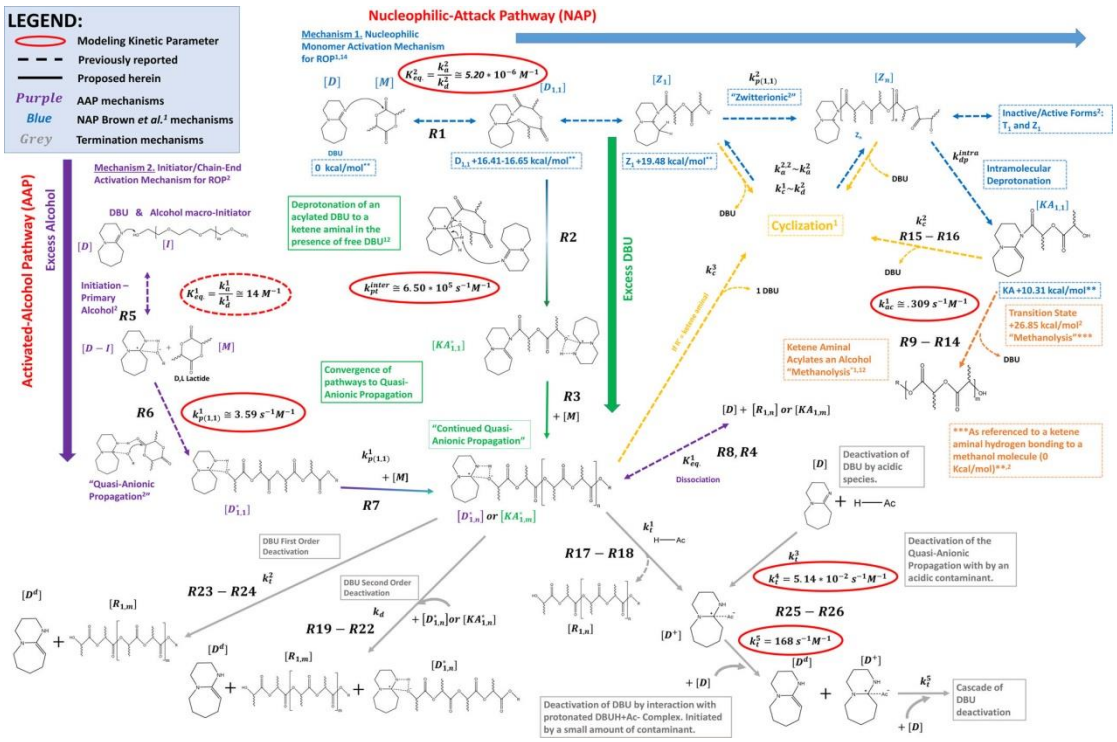

Figure 4.3 - Main lactide ring opening reaction pathways by means of DBU as a catalyst. Reproduced from: N. J. Sherck et al, *Macromolecules* **2016**, 49 (13), pp 4699–4713.

The authors addressed the strong deviation from non-pseudo-first-order kinetics of lactide conversion by DBU catalysis by considering the interplay between two mechanisms originated by the two characteristic features of DBU: basicity and nucleophilicity. Both aspects have been proposed as (almost) singularly responsible of lactide ROP: Lohmeijer et al. hypothesized that polymerization was driven by the activation of alcohol end groups by hydrogen bonding with DBU, in an activated alcohol pathway (AAP) (**Scheme 4.2** – Activated-alcohol pathway (AAP) to ring opening polymerization of lactide.).[137]

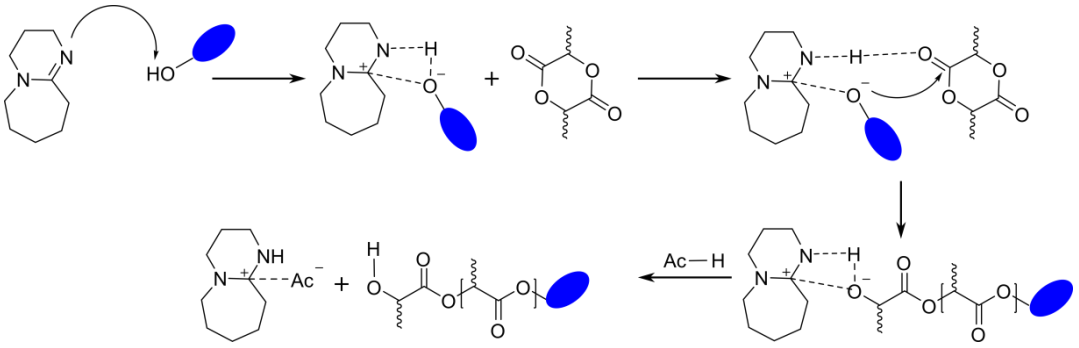

Scheme 4.2 – Activated-alcohol pathway (AAP) to ring opening polymerization of lactide.

DBU nucleophilicity[138], on the other hand, was shown able to initiate ROP of lactide even in the absence of any alcohol initiator, in a nucleophilic attack pathway (NAP) (Scheme 4.3), even though no correlation between initial monomer feed and final molecular weight was found.[139] The complex interaction of the two mechanisms was finally exploited by Bibal et al,[58] who used two nucleophilic co-catalysts (substituted phenols and DBU) with opposed H-bonding capabilities to synthesize monodisperse homo- and block copolymeric PLA, PCL and PVL.

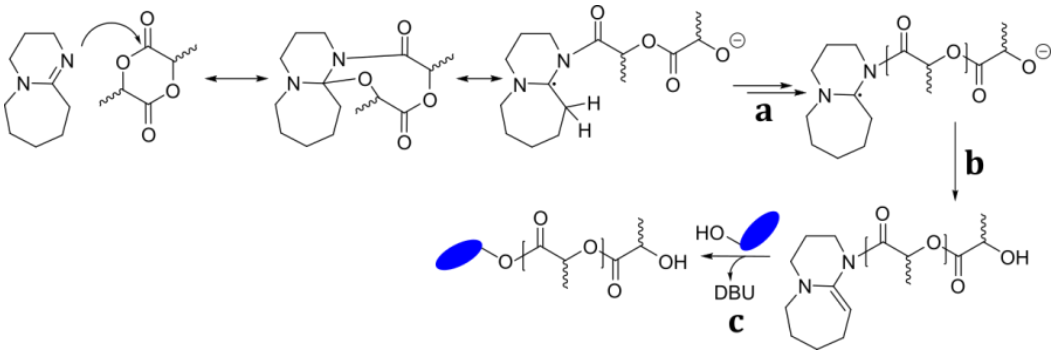

Scheme 4.3 – Nucleophilic attack pathway (NAP) to ring opening polymerization of lactide. (a) Pseudo-zwitterionic mechanism, (b) ketene-aminal formation by intramolecular deprotonation. Possible acylation of an alcohol by ketene-aminal ended chains (c).

The compresence of the two viable pathways is, of course, problematic when the goal is to introduce a desired terminal functionality on the polyester by using a suitable alcoholic initiator. The formation of amphiphilic block copolymers where one block is PLA and the other is PEO is commonly achieved by this strategy, using a –OH mono- or bifunctionalized preformed PEO polymer as initiator. Sherck and collegues effectively show the detrimental effect of DBU attack on lactide on the formation of PEO-b-PLA copolymers; SEC analysis of copolymers during LA polymerization with a two-fold excess of PEO-OH initiator with respect to DBU shows a clear translation to higher molecular weights and no significant peak broadening relative to the starting PEO block. On the contrary, when DBU is used in excess relative to PEO-OH, multimodal, broad peaks testify the presence of multiple molecular weight distributions, generated by NAP as well as acylation reactions.

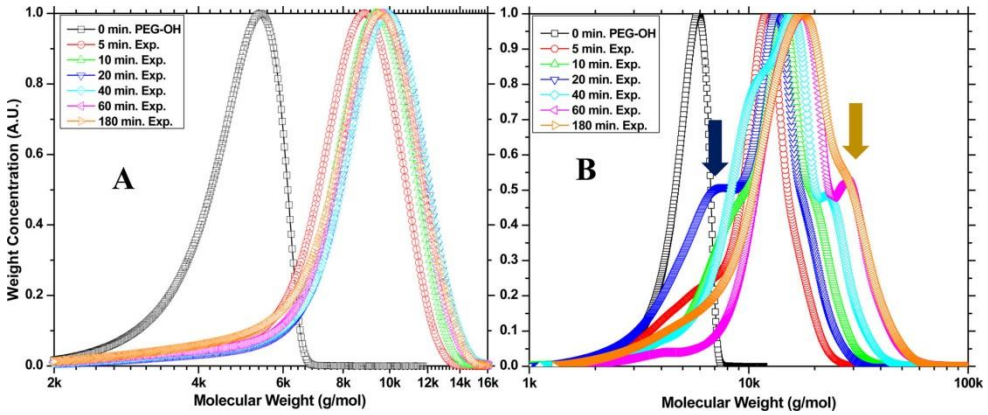

Figure 4.4 – GPC traces of PLA copolymers initiated by monohydroxylated PEO at various reaction times. (A) [LA]:[PEO]:[DBU] = 72.3 : 2.1 : 1, (B) [LA]:[PEO]:[DBU] = 72.3 : 0.4 : 1. Arrows highlight the emergence of spurious low (black) and high (yellow) molecular weight populations. Reproduced from: Sherck, N. J.; Kim, H. C.; Won, Y. Y. *Macromolecules* **2016**, *49* (13), 4699–4713.

These undesired processes which can occur in excess DBU conditions, do not necessarily involve alcohol species and can lead to PLA cyclization or combination via a pseudo-zwitterionic process or ketene-aminal[140] formation, and can give rise to lower or higher molecular weight populations.

In this very complex synthetic framework, Sherck et al. built maps based on simulated reactions by modeling all kinetic pathways (except for catalyst poisoning), in which optimal [LA]:[PEO]:[DBU] ratio regions are outlined (Figure 4.5).

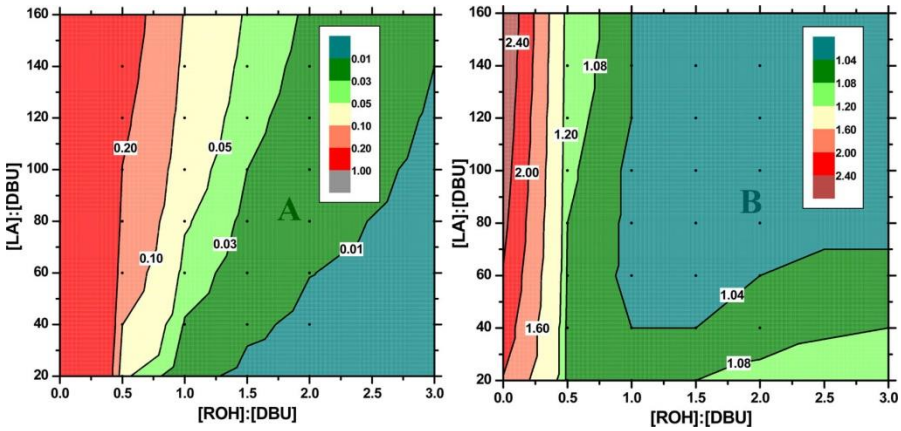

Figure 4.5 – *In silico* maps of (A) fraction of ketene-aminal ended chains and (B) copolymer PDI as a function of [LA]:[DBU] and [ROH]:[DBU] ratios. Reproduced from: Sherck, N. J.; Kim, H. C.; Won, Y. Y. *Macromolecules* **2016**, *49* (13), 4699–4713.

According to Figure 4.5, our synthetic conditions put us at risk of formation of a fraction of ketene-aminal ended chains comprised between 0.05 and 0.10. A closer analysis of PEO_{113}-b-PLA_{1300} proton spectra revealed the presence of a peak at 2.80 (Figure 4.6), and compatible

with the ketene aminal form of DBU. The signal of the protons on the corresponding carbon of pure DBU was not detected, suggesting that no free DBU is present. It is therefore possible that a fraction of chains were ketene-aminal ended. Nonetheless, its GPC curve (Figure 4.2) was narrow and fairly symmetrical, so we estimated the fraction to be small.

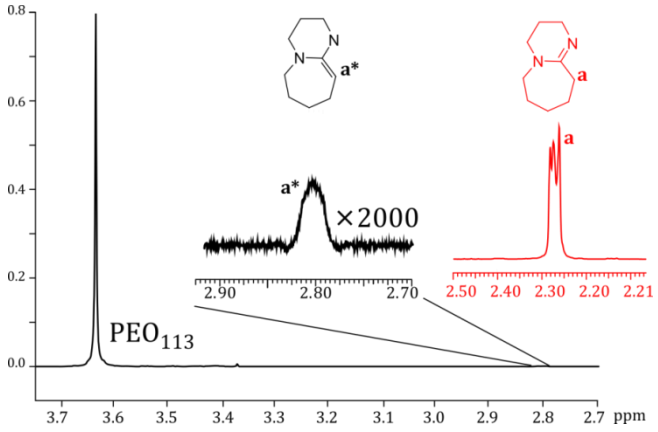

Figure 4.6 – ^{1}H-NMR spectrum of PEO_{113}-*b*-PLA_{1300} ($CDCl_3$, 500 MHz). A small peak at 2.80 suggests the formation of keten aminal derivative of DBU. The peak generated by the protons on the corresponding carbon of DBU is also reported (red lines).

Attempts at separation of non-PEO-terminated PLA chains from actual diblock copolymers by precipitation and dialysis were not successful. Contrarily, no precipitation was observed even in water, where a rather stable dispersion was formed. It is therefore reasonable to assume that any homopolymeric PLA present in the sample interacts with the PLA block in PEO-*b*-PLA. For this reason, volumic PEO fraction, $f_{PEO,}$ was calculated from m_{PLA} obtained from NMR, and varied from 0.05 to 0.52 (Table 4.1).

Table 4.1 – Composition, molecular weight, PDI and glass transition temperature of the PEO-b-PLA copolymers. [a]Number of repeating PLA units calculated from ^{1}H-NMR spectra. [b]Calculated using $\rho_{PEO} = 1.21\ g/cm^3$ and $\rho_{PLA} = 1.25\ g/cm^3$.

Label	$N_{LA}{}^{a}$	$f_{PEO}{}^{b}$	$M_n{}^{NMR}$ (Da)	PDI^{GPC}	T_g (°C)
PEO_{113}-*b*-PLA_{65}	65	0.52	9650	1.27	-33
PEO_{113}-*b*-PLA_{300}	305	0.19	26930	1.13	19
PEO_{113}-*b*-PLA_{400}	417	0.15	35000	1.21	32
PEO_{113}-*b*-PLA_{500}	486	0.13	39960	1.10	33
PEO_{113}-*b*-PLA_{1300}	1359	0.05	102830	1.10	45

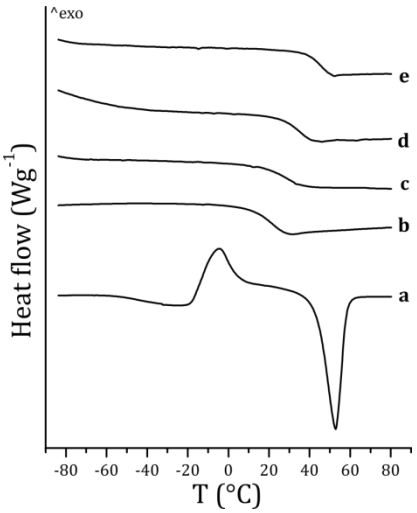

Figure 4.7 - DSC curves of PEO-*b*-PLA samples. (a). PEO_{113}-*b*-PLA_{65}, (b) PEO_{113}-*b*-PLA_{300}, (c) PEO_{113}-*b*-PLA_{400}, (e) PEO_{113}-*b*-PLA_{500}, (f) PEO_{113}-*b*-PLA_{1300}.

Regarding the phase separation properties of PEO and PLA, literature reports they are at least partially miscible in the bulk.[141] DSC traces of PEO_{113}-*b*-PLA_x samples freeze dried after dialysis are depicted in Figure 4.7: with the exception of the copolymer with the shortest PLA block (m_{PLA} = 65), the thermograms show a single glass transition, with T_g values always lower than those expected for a PLA homopolymer with the same molecular weight. On the other hand, PEO_{113}-b-PLA_{65} (Figure 4.7(a)) features a broad glass transition starting at -50 °C partially overlapping with an exothermic peak at 0° C, and finally an endothermic peak at 52 °C, compatible with PEO_{113} melting. The presence of a crystallization event during heating, at a higher temperature compared to homopolymeric PEO_{113}, can be explained considering that the reported thermogram is recorded after a first heating and subsequent cooling at 20 °C/min, a rate sufficiently fast to cause a quenching of the sample in a complete glassy state. Only after the glass transition of copolymer occurs at -33 °C the polymer gains enough mobility to crystallize and finally melt.[142] The absence of any melting events in these copolymers suggests that PEO crystallization is frustrated by the presence of PLA, indicating no phase separation between the blocks for f_{PEO} lower than 0.20, as seen in other PEO based block copolymers.[143]

Although inclusion of PLA chains in the PEO domains is negligible in aqueous dispersions (unless for very low m_{PLA}),[144] the effect of the organic solvent on phase separation of low-χ blocks is expected to be greater. Moreover, though effectively hydrophobic, PLA is rich in H-bond accepting moieties, which could influence its interaction with non-selective solvents and, in the end, aggregation. Finally, PEO-*b*-PLA systems attract interest as carriers

for hydrophobic drugs, which are often loaded into nanoparticles by physical encapsulation starting from a copolymer/drug solution in a suitable organic solvent. It is therefore important to investigate the effect of such solvents on the final size and shape of nanoparticles, as both features are strongly linked to cell toxicity and circulation times.

4.3 Effect of good solvent on PEO-*b*-PLA self-assembly

Both theory[92] and experiments show that the most stable nanoparticle morphology for predominantly hydrophilic ABCs in a polar solvent is that of a spherical ("star-like") micelle, where the hydrophobic block is segregated in the core and the long hydrophilic block acts as a stabilizing solvated corona. In predominantly hydrophobic ABCs, the hydrophilic block is too short to balance the elastic and interface energy of the solvophobic block by solvation, so relative energy minima can be reached by arrangement in different geometries, generally transitioning from spherical micelles to bilayered structures like vesicles. While different particle morphologies usually coexist, PEO-*b*-PLA copolymer composition ranges that preferably yield a specific architecture have been proposed, i.e. $f_{PEO} > 0.42$ for spherical and cylindrical micelles, $\sim 0.20 < f_{PEO} < 0.42$ for vesicles and $f_{PEO} < 0.20$ for solid-like particles.[125]

However, copolymer composition is only one of many parameters that regulate macromolecular self-assembly: due to the high molecular weight of polymers, transient morphologies are often kinetically frozen in thermodynamically unstable architectures, and the kinetic path undertaken by polymer chains during aggregation is affected by the dispersant properties. In order to study the interplay of these effects, aliquots of each copolymer were dissolved in different nonselective solvents at a concentration of 20 mg/mL. Then, deionized water was filtered and added dropwise at a constant flow of 4 mL/h, at room temperature and under stirring, until a large excess with respect to the organic solvent was reached. The remaining organic solvent was removed by 48 h of dialysis against water.

Dynamic Light Scattering was applied to characterize nanoparticle size distribution on all dispersions immediately after dialysis. In Figure 4.8 hydrodynamic diameter (D_H) distributions are reported. The most evident feature is the great variation in size and distribution of the nanoparticles, the smallest ones having D_H of 21 nm whereas the largest ones reach D_H values of more than 1000 nm. As expected, NP size increases with m_{PLA}, but, more interestingly, the effect of the starting solvent is also quite clear. Most striking is the case of PEO_{113}-*b*-PLA_{300}, where NP size undergoes a 4-fold increase when the solvent is changed from ACT ($\langle D_H \rangle$ = 33 nm) to DMF ($\langle D_H \rangle$ = 134 nm) (Table 4.2). As a general trend, $\langle D_H \rangle$ values increase in the order: ACT < DX < THF ~ DMF, while distributions tend

to have a higher polydispersity, transitioning from single monodisperse to polydisperse populations. This effect is less pronounced for PEO_{113}-*b*-PLA_{65}, whose composition lies in the range where spherical star-like micellar morphology is strongly favored by thermodynamics. Interestingly, the effect of DMF on nanoparticle size is in opposition with that reported by Eisenberg's group on PS-*b*-PAA crew-cut copolymers, where it lead to smaller particles compared to THF and DX.[145] This suggests the presence of a specific solvent-PLA interaction in the case of DMF.

During the nanoprecipitation process, polymer chains need to migrate within the liquid phase and organize into compartmentalized aggregates by virtue of the blocks' opposite affinity with the surrounding solvent. It is expected, therefore, that parameters such as the solvent's viscosity (η), and all the relevant interaction parameters ($\chi_{S\text{-}W}$, $\chi_{PLA\text{-}S}$, $\chi_{PLA\text{-}W}$, $\chi_{PEO\text{-}S}$, $\chi_{PEO\text{-}W}$, $\chi_{PEO\text{-}PLA}$, where S = organic solvent, W = water) will influence the assembly process in a complex way.

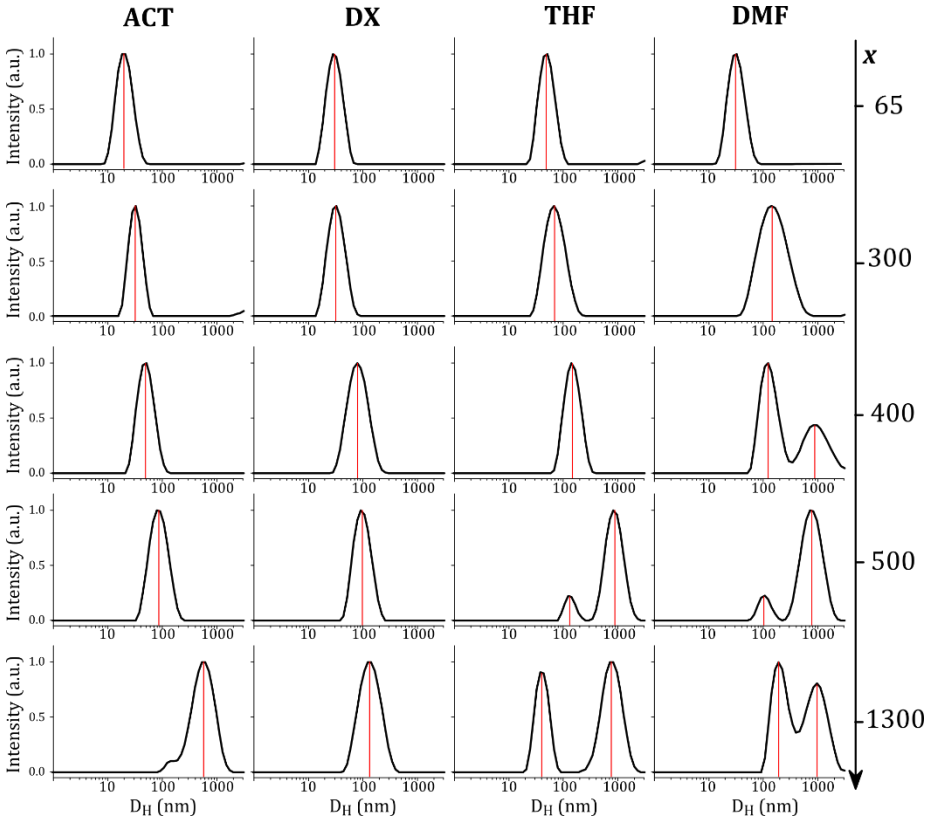

Figure 4.8 - Hydrodynamic diameter distributions of PEO_{113}-*b*-PLA_x nanoparticles assembled in water from different organic solvents. Copolymer labels are reported on the right.

Table 4.2 - Average hydrodynamic diameters (<D_H>) and PDIs of copolymer dispersions obtained from the four different solvents after dialysis. When multiple NP populations are present, each peak was considered separately.

Label	Solvent	<D_H>$_1$ (nm)	PDI_1	<D_H>$_2$ (nm)	PDI_2
PEO_{113}-*b*-PLA_{65}	ACT	21	0.111	–	–
	DX	31	0.098	–	–
	THF	41	0.053	–	–
	DMF	34	0.112	–	–
PEO_{113}-*b*-PLA_{300}	ACT	33	0.070	–	–
	DX	34	0.114	–	–
	THF	65	0.143	–	–
	DMF	134	0.240	–	–
PEO_{113}-*b*-PLA_{400}	ACT	47	0.096	–	–
	DX	74	0.140	–	–
	THF	139	0.096	–	–
	DMF	138	0.161	1064	0.307
PEO_{113}-*b*-PLA_{500}	ACT	80	0.121	–	–
	DX	92	0.109	–	–
	THF	136	0.046	912	0.128
	DMF	109	0.062	831	0.173
PEO_{113}-*b*-PLA_{1300}	ACT	620	0.194	–	–
	DX	123	0.150	–	–
	THF	42	0.075	832	0.168
	DMF	219	0.208	994	0.364

Among others, Hansen solubility parameters can be used to estimate the Flory-Huggins interaction parameters, χ, between PEO and PLA blocks and between each block and a selected solvent:[146]

$$\chi_{P-S} = \left(\frac{V_m}{RT}\right)\left[\left(\delta_D^S - \delta_D^P\right)^2 + 0.25\left(\delta_P^S - \delta_P^P\right)^2 + 0.25\left(\delta_H^S - \delta_H^P\right)^2\right] \qquad (6)$$

where δ_D, δ_P and δ_H are the contributions of dispersion forces, polar interactions and hydrogen bonds to solubility, respectively, V_m is the molar volume of the solvent, T is temperature and R is the gas constant. Solubility parameters and Flory-Huggins values

Among the solvents used in our study, dioxane has the highest χ with either block: $\chi_{PLA\text{-}DX}$ is close to 0.5, whereas $\chi_{PEO\text{-}DX}$ is 0.84, so PEO chains in this solvent tend to shrink compared to the unperturbed state. Dioxane is also the solvent with highest viscosity. The other three solvents have variable viscosity and $\chi_{P\text{-}S}$ significantly lower than 0.5 for both blocks, thus polymer chains are considerably swollen by them (Table 4.3). Predicted values of χ can be significantly different from the experimental ones, as in the case of acetone, which has been found to act as theta solvent for PLA;[147] however, in absence of comprehensive set of experimental data, predicted values of χ are a useful tool for comparing the solubility behavior in differ solvents.

Table 4.3 – Viscosity η (at 20 °C), Hansen solubility parameters and Flory-Huggins interaction parameters between each organic solvent and PEO and PLA homopolymeric blocks ($\chi_{S\text{-}PEO}$ and $\chi_{S\text{-}PLA}$, respectively), estimated from Hansen solubility parameters according to equation (6).

	η (cP)	**δ_D [MPa]$^{0.5}$**	**δ_P [MPa]$^{0.5}$**	**δ_H [MPa]$^{0.5}$**	**δ_T [MPa]$^{0.5}$**	**$\chi_{PEO\text{-}S}$**	**$\chi_{PLA\text{-}S}$**
Acetone	0.36	15.5	10.4	7	19.9	0.094	0.125
Dioxane	1.37	19	1.8	7.4	20.5	0.84	0.588
THF	0.55	16.8	5.7	8	19.5	0.212	0.138
DMF	0.92	17.4	13.7	11.3	24.9	0.12	0.263
PEO[148]		17	10.7	8.9	22.0		
PLA[130]		17.5	9.5	7.3	21.2		

Considering polymer-solvent interaction, on the basis of the calculated values of polymer-solvent interaction parameters $\chi_{P\text{-}S}$ for the solvents used, no specific trend can be discerned, in fact acetone and dioxane have a similar effect on the formation of the nanoparticles despite having the lowest and highest values of $\chi_{P\text{-}S}$, respectively (Table 4.3). The affinity of the organic solvent with the selective solvent is also considered to play a role in the NP size: an increased organic solvent/water affinity was reported to result in a smaller average nanoparticle size, allegedly due to more efficient solvent diffusion and polymer dispersion into water.[123,149] Solvent mixture viscosity can also hamper or facilitate the diffusion of polymer chains within the continuous phase, with less viscous solvents yielding smaller, more monodisperse nanoparticles. Again, our results contrast with these predictions,

as acetone and dioxane, with lowest and highest viscosities respectively, yield similarly small and homogeneous dispersions.

Albeit a complex combination of all these factors is possibly responsible for the observed trend, it's interesting to notice a simpler correlation between nanoparticle size and solvent hydrogen bonding ability δ_H, the hydrogen-bonding contribution to the total solubility parameter according to Hansen: it increases in the order ACT < DX < THF < DMF (Figure 4.8) with a corresponding increase in nanoparticles dimension and polydispersity. In fact PLA films are swollen to a higher degree by organic solvents with a high δ_H.[150]

However DLS provides just an evaluation of the size of the nanoparticles but has no insight on their actual morphology, so we selected representative dispersions to be studied by TEM and cryo-EM (CEM). PEO_{113}-*b*-PLA_{65}, as expected, always presents spherical dense objects with diameters quite close with those measured by DLS, confirming the core-corona morphology, as shown in the representative CEM micrograph of PEO_{113}-*b*-PLA_{65} self-assembled from acetone reported in Figure 4.9.

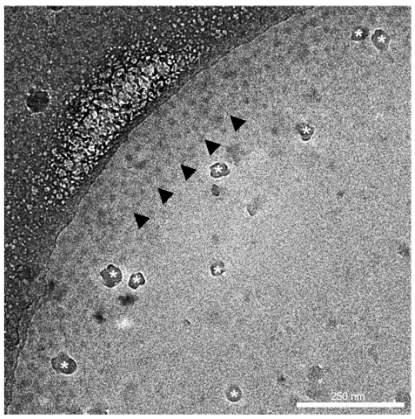

Figure 4.9 - Single projection image of PEO_{113}-*b*-PLA_{65} micelles (arrowheads) close to the carbon film. The asterisks point to ice contaminations. Scale bar: 250 nm.

Considering PEO_{113}-b-PLA_{500} self-assembled from dioxane ($\langle D_H \rangle$ = 92 nm, PDI = 0.109), CEM and cryo-electron tomography (CET) analyses clearly indicate that the sample is constituted by two populations of particles differing in both size and morphology (Figure 4.10). The first population is constituted by small micelles (average diameter = 55 ± 6 nm, number of objects measured n = 37) that appear as dark roundish spots in CET images (Figure 4.10(A–B)). When observed in tomographic sections, the micelles reveal an electron-dense core and a well-defined darker outer shell, as also shown by their characteristic intensity profile (Figure 4.10(D), solid blue line). The other nanoparticles are instead larger vesicles (polymersomes) (average diameter = 83 ± 11 nm, n = 77) that in CET appear to have an

electron transparent core surrounded by a more electron-dense corona (Figure 4.10(A,C)). Single tomographic sections through the polymersomes reveal the presence of a (19 ± 3) nm thick intact electron-dense external membrane surrounding a water filled central cavity. The thick membrane is confined by two concentric highly dense regions, as visible in their characteristic intensity profile (Figure 4.10(D), solid orange line).

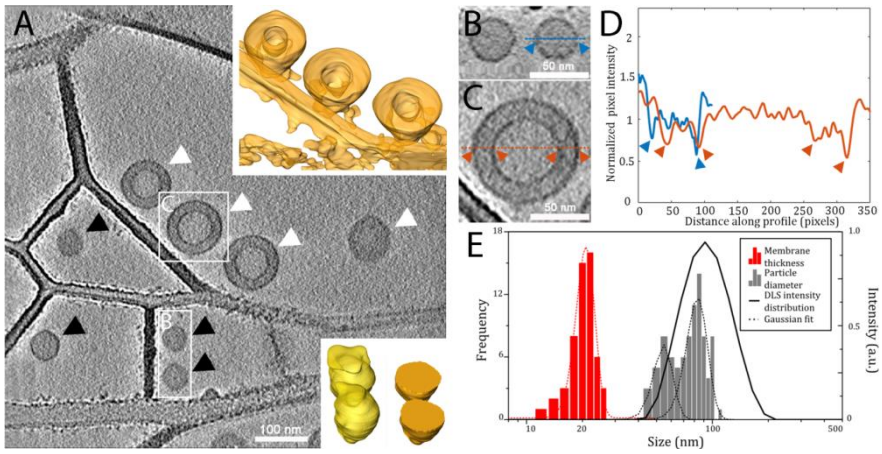

Figure 4.10 - Nanoparticle morphology of PEO_{113}-*b*-PLA_{500} assembled from dioxane as revealed by CET: (A), averaged tomographic slice showing micelles (black arrowheads) and polymersomes (white arrowheads). The insets show the 3D models of cross sectioned polymersomes (upper left) and micelles (bottom left: whole micelles are yellow; cross sectioned micelles are in orange). (B), high magnification of the corresponding boxed region in A (micelles). (C), high magnification of the corresponding boxed region in C (polymersomes). (D), Electron density (plotted as pixel light intensity) measured along the diameter of micelles (blue line) and polymersomes (red line). The blue and orange arrowheads point to corresponding points in B and C respectively. (E), Particle size distribution calculated by DLS (solid line) and CEM (grey histogram), and polymersome membrane thickness measured by Cryo-EM (red histogram).

PEO_{113}-*b*-PLA_{1300} due to the large predominance of the hydrophobic block can be considered to be in the crew-cut micelle forming compositional range; when self-assembled from THF, DLS size distribution has two populations: one with $\langle D_H \rangle$ below the 50 nm and the other with $\langle D_H \rangle$ above 500 nm. In CET micrographs (Figure 4.11) it is possible to appreciate the presence of dark circular spots of diameter of 31 ± 4 nm (n = 287) that are compatible with the first population of nanoparticles in the DLS. In tomographic slices it appears that the NPs exhibit a dense core and a thin electron-dense outer shell, as visible in their characteristic intensity profile (Figure 4.11(D)). Although such a micellar morphology in principle is less favored than lamellar structures in case of crew-cut polymers, it can be anyway favored for kinetic reasons, especially in low χ systems such as PEO and PLA. Interestingly in cryo-EM conditions the second population seen in the DLS is not visible,

while by TEM at room temperature spherical objects larger than 500 nm are clearly distinguishable (Figure 4.12), providing a morphological picture compatible to that of the composite micelles, generated by a hierarchical self-assembly. This process initially comprises the formation of core-corona micelles, in which the corona is too thin to completely stabilize the dispersion: thus some micelles tend to aggregate into larger systems, where there is a considerable decrease of the specific surface area. An early onset of this phenomenon may be represented by the formation of necklace-like aggregates depicted in Figure 4.11(C). Failure to observe these particles in CEM is possibly due to the thickness of vitrified water film suspended in the grid holes, which may be too thin to host objects this large.

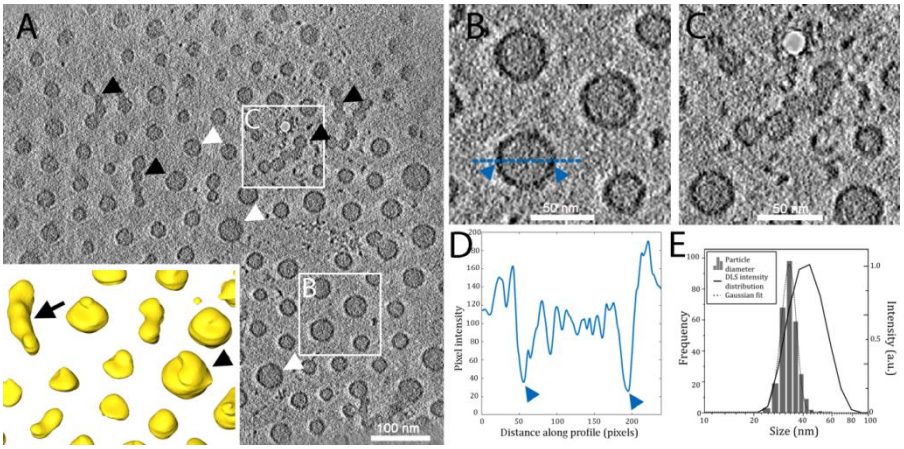

Figure 4.11 – Nanoparticle morphology of PEO_{113}-*b*-PLA_{1300} assembled from THF as revealed by CET (A). The inset shows the 3D models of single micelles (arrowhead) and necklace-like aggregates (arrow). (B), high magnification of the corresponding boxed region in A (single micelles). (C), high magnification of the corresponding boxed region in A (necklace-like aggregates). (D), Electron density (plotted as pixel intensity) measured along a micelle diameter. The blue arrowheads point to corresponding points in B. (E), Particle size distribution calculated by DLS (solid line) and Cryo-EM (histogram).

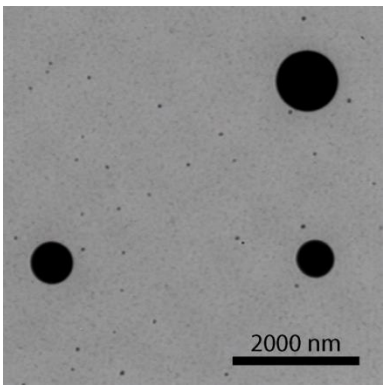

Figure 4.12 - Room temperature TEM micrograph of large compound aggregates in PEO_{113}-*b*-PLA_{1300} self-assembled from THF.

The same copolymer self-assembled from DMF confirms the existence of two types of objects, one with $<D_H>$ = 219 nm and the other with the same dimension of the large objects obtained from THF. In this case, CEM micrographs reveal the presence of a large variety of shape and dimensions: in Figure 4.13 single or partially fused micelles ranging from 100 nm to 300 nm are visible. Electron density profiles (Figure 4.13(C)) highlight uniformly dense objects whose inner structure can be ascribed to hierarchical aggregation. CET reported in Figure 4.13(E) and (F) reveal a further process of fusion of the particles forming low symmetry objects of about 1000 nm. Upon coalescence, particles seem to assume an ellipsoidal shape. These characteristics suggest a certain softness of the particle texture.

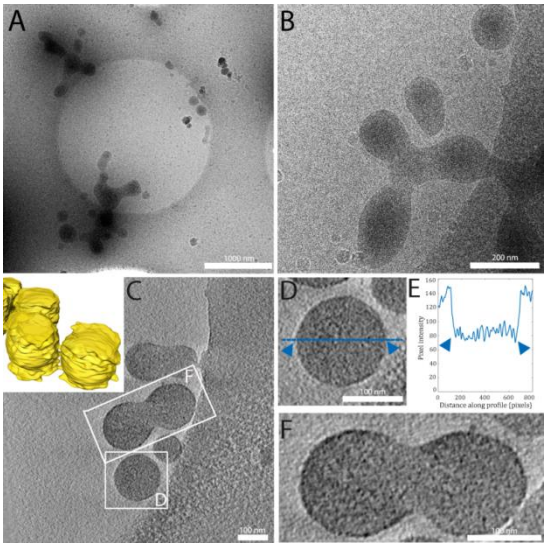

Figure 4.13 - Nanoparticle morphology of PEO113-b-PLA1300 assembled from DMF as revealed by cryo-EM and CET: (A), low magnification projection image showing the polymer in different morphologies. (B), projection image showing fused large compound micelles

(LCM). (C), averaged tomographic slice through single (D) and fused (F) LCM. The inset shows the 3D model both large compound micelles. (D) high magnification of the corresponding boxed region in C showing a single LCM. (E), Electron density (plotted as pixel intensity) measured along the diameter of the single LCM in D. The blue arrowheads point to corresponding points in D. (F) high magnification of the corresponding boxed region in C showing a fused LCM.

CEM results therefore confirm that the products of the self-assembly of the same polymer, PEO_{113}-b-$PLA_{1300,}$ starting from two different non-selective solvents, THF and DMF present significant differences in their precise morphology.

We tried to generalize the correlation between the morphology evaluated by DLS, CEM and CET; all the NPs characterized by DLS are marked in a PDI vs $<D_H>$ plot in Figure 4.14. the overall space is divided into three regions in which different morphologies are *preferentially* formed, based on microscopy data: core-corona micelles for low size and low PDI, polymersomes for medium size and medium PDI, and hierarchical aggregates (collectively labeled as large compound micelles) for large size and large PDI. It should be noted that the edges of these areas are not sharp, and considerable overlap is possible (as is the case of polymersome and micelle mix formed by PEO_{113}-*b*-PLA_{500}). Individual peaks in nanodispersions are grouped together in colored areas based on the starting solvent used: nanoparticles assembled from ACT and DX roughly occupy the same area in the bottom left corner of the plot, while DMF leads mainly to the formation of hierarchically structured particles. Finally, THF has the least constraining effect on particle morphology. The two outlying data (PEO_{113}-*b*-PLA_{65} from DMF and PEO_{113}-*b*-PLA_{1300} from ACT) correspond to the lowest and highest molecular weight and f_{PEO}, respectively, were solvent may not be exert the dominant effect.

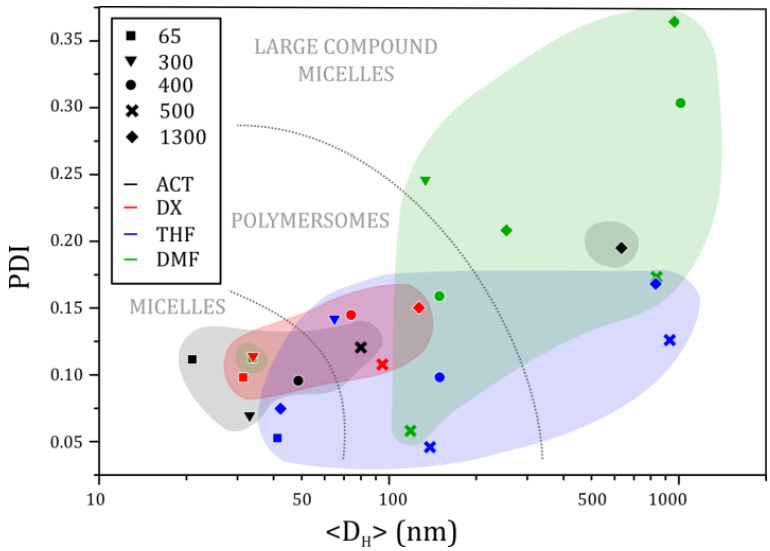

Figure 4.14 – PDI vs average D_H plot of all copolymer dispersions obtained by DLS from different organic solvents. Dashed grey lines outline size ranges where different morphologies are preferentially formed, as assessed by CEM and CET. Colored areas encompass nanodispersions prepared from the same non-selective solvent: ACT (grey), DX (red), THF (blue), DMF (green).

4.4 Conclusions

In this Chapter, the overall picture of PEO-b-PLA self-assembly by gradual solvent switch in water was enriched by the investigation of the effect of the starting common solvent on nanoparticle size and morphology. A sample set of PEO_{113}-based copolymers were synthesized by ring opening polymerization of *rac*-lactide catalyzed by metal-free, non-toxic DBU. Water free, but otherwise mild reaction conditions yielded monodisperse amphiphilic diblock copolymers of various f_{PEO}, though there was evidence of the formation of undesired ketene-aminal ended PLA chains. Each sample was dissolved in four organic solvents (ACT, DX, THF, DMF) and nanodispersions obtained after gradual addition of water were analyzed by DLS and CEM. Except for the diblock with the shortest PLA block (PEO_{113}-*b*-PLA_{65}), the effect of solvent on nanoparticle size and polydispersity was apparent; in particular, both size and polydispersity increased in the order ACT < DX < THF ~ DMF. These data are only in partial agreement with literature reported trends and models, and warrant further investigation. CEM and CET were used to image selected nanodispersions and classify DLS data into three regions, labeled micelles (small size, low PDI), polymersomes (medium size, medium-low PDI) and large compound micelles (large size, large PDI). While ACT and DX yielded mostly micelles, THF allowed to access a much broader morphological space. Finally, DMF favoured second-order aggregation phenomena.

CHAPTER 5

Poly(2-ethyl-2-oxazoline)-based block copolymers self-assembly

5.1 Introduction

Although being so far the unparalleled 'golden standard' of drug and drug carrier coatings for biomedical applications, a few drawbacks of PEO (and a strained patent situation) have lead researchers to seek alternatives. Low-molecular weight PEO was found to interact non-specifically with blood cells favoring the formation of dangerous clots that could lead to embolism.[151] Hypersensitivity reactions in patients to whom PEG-containing formulations were administered either intravenously, orally or dermally has been observed, although the mechanism of sensitization and its correlation with PEO have not been conclusively elucidated yet.[152–155] 4 kDa PEO can also cause specific response by the immune system, with the associated production of PEO antibodies.[156] Furthermore, PEGylation doesn't always result in improved pharmacokinetics;[157] on the contrary, it was found to induce accelerated blood clearance (ABC) of previously injected PEGylated liposomes, and also decreased the selectivity of passive targeting.[158] These immunogenic and antigenic effects are generally induced by low molecular weight PEO (< 1000 Da), so higher molecular weights should be considered for medical applications; on the other hand, since PEO is non-biodegradable, accumulation in the liver can occur if molar masses exceed 60 kDa.[105] Finally, due to its polyether structure, PEG is more sensitive to degradation than vinylic polymers.[159]

Although the discovery of poly(oxazoline)s (POx) dates back to the 1960s,[160,161] their potential in drug delivery applications has arisen only recently.[162] A major limitation to commercial application was represented by slow reaction kinetics: polymerizations can take hours to days in reflux conditions; development of POx-based materials has considerably sped up after the advent of microwave reactors, that allow reaction times on the minutes scale.[65,163] POx are structural isomers of polyacrylamides and polypeptides, and are often termed 'pseudopeptides',[164] despite lacking any stereogenic centers that would allow secondary structure formation. Tests in mice showed that both PEtOx and PMeOx are rapidly cleared from the bloodstream without substantial accumulation for molecular weights around 4500 Da.[165,166] Their potential role as PEO substitutes emerged when it was found that hydrophilic coating of liposomes with poly(2-methyl-2-oxazoline) (PMeOx) and poly(2-ethyl-2-oxazoline) (PEtOx) had a comparable efficiency at prolonging circulation times as PEO.[167,168] Furthermore, a PEtOx layer grafted onto a glass surface promoted growth of healthy endothelial cells, confirming its biocompatibility.[169]

5.2 Experimental

Materials

Dry dichloromethane (DCM), diethyl ether, tetrahydrofuran (THF), methanol (MeOH), N,N'-dimethylformamide (DMF) and ethanol (EtOH) were purchased from Sigma Aldrich and used as received. Acetonitrile (AN) (Sigma Aldrich) was distilled and stored on activated zeolites (3 Å) under dry argon prior to use. 2-Ethyl-2-Oxazoline (EtOx) and 2-methyl-2-oxazoline (MeOx) (Sigma Aldrich) were stirred over CaH2 overnight and distilled. Methyl-p-toluene sulfonate (MeTos) (Alfa Aesar) was distilled and stored at -20 °C under argon. Styrene (Sty) and tert-butyl acrylate (*t*BA) (Sigma Aldrich) were passed through a column of activated alumina to remove the inhibitor. Azobisisobutyronitrile (AIBN) (Sigma Aldrich) was crystallized from MeOH at 4 °C. DDAT was synthesized as described elsewhere[8] and recrystallized from *n*-hexane before use.

5.2.1 Synthesis of $PEtOx_{25}$-OH, $PEtOx_{25}$-DDAT, $PEtOx_{25}$-AA

5.2.2 Synthesis of $PEtOx_{25}$-*b*-PS_{50}

5.2.3 Synthesis of $PEtOx_{25}$-*b*-PS_{50}-b-P*t*BA_{35}

5.3 Results and discussion

In previous Chapters, the main focal point regarding the effect of polymer-solvent interaction on self-assembly was placed on the core-forming block (PS or PLA, respectively). This reflects the general trend that emerges from the literature, where the hydrophilic block is thought of as being completely solvated by water and, as such, their interaction with the solvent mixture is seldom given much importance. Exceptions are related to stimuli-responsive hydrophilic blocks, e.g. polymers with lower critical solution temperature (LCST) or upper critical solution temperatures (UCST) values in water close to ambient or body temperature such as poly(N-isopropylacrylamide) (PNIPAM) or poly(N-acryloylasparaginamide) (PNAAM),[170] or protic polymers which can switch between protonated and deprotonated states at pH values not far from 7, such as PAA. As a nonionic hydrophilic block, PEO has been extensively studied,[171,172] but direct evaluation of its effect on self-assembly by comparison with other non-ionic hydrophilic blocks is rare. With the perspective goal of examining this topic in depth, poly(2-ethyl-2oxazoline) (PEtOx) was

selected as a hydrophilic block for PS; this way, comparison with our study on PS-*b*-PDMA and data available from the literature on PS-b-PEO is possible.

5.3.1 Synthesis and end functionalization of $PEtOx_{25}$

The two main strategies for the formation of PS-*b*-PEtOx block copolymers are: i) linking of preformed blocks (by coupling reactions, click reactions, and so on) or ii) polymerization of one of the blocks on a suitably functionalized preformed first block. We decided to undertake the second pathway, in particular to synthesize a PEtOx macroCTA for the subsequent RAFT functionalization of PS; hydrophilic macroCTAs are also interesting for RAFT polymerization in PISA conditions. In this initial part of the project, we focused on the chain-end functionalization of PEtOx. In order to study terminal groups precisely, low molecular weights were targeted.

For the polymerization of EtOx, the same procedure devised by Hoogenboom[65] was followed. All reagents were distilled freshly before use, all glassware was dried in the oven at 120 °C the night before polymerizations were carried out, and inert and dry atmosphere was used. Three parallel reactions were performed; methyl-*p*-toluene sulfonate was used as CROP initiator of EtOx in dry acetonitrile at 80 °C, at an initiator-to-monomer ratio of 1:25 (complete monomer conversion was targeted in analogy to ROP of lactide). After 24 hours, flasks were removed from the oil bath, and a different terminating agent was added to each flask: methanolic KOH, RAFT agent DDAT (dissolved in dry DCM) and acrylic acid (dissolved in dry acetonitrile) (Scheme 5.1). AA-terminated PEtOx is interesting as it would allow the synthesis of brush PEtOx homopolymers and copolymers by RAFT. Reaction solutions were left stirring overnight at 50 °C.

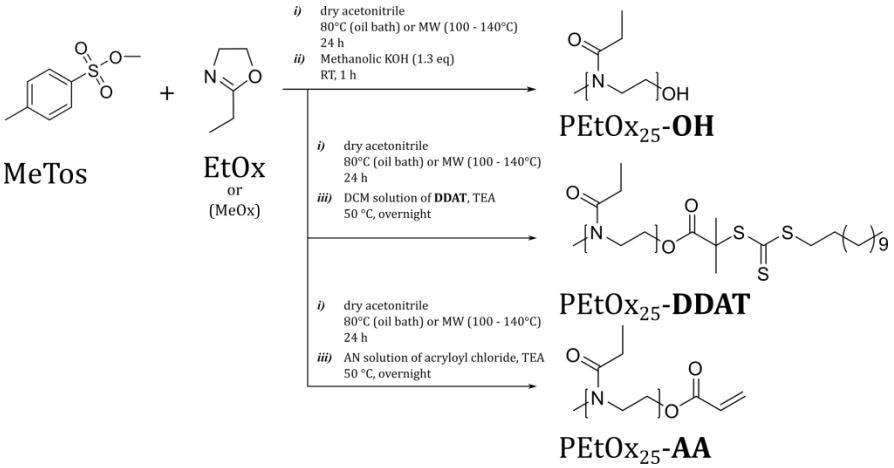

Scheme 5.1 – Chain end functionalization reaction scheme of PEtOx to yield $PEtOx_{25}$-OH, $PEtOx_{25}$-DDAT and $PEtOx_{25}$-AA.

After allowing to return to room temperature, aliquots were withdrawn, diluted in $CDCl_3$ and analyzed by ^{1}H-NMR to calculate EtOx conversion. In all cases, no monomer signals were visible, indicating complete monomer conversion.

Polymers were initially precipitated into cold diethyl ether twice. In the case of $PEtOx_{25}$-DDAT and $PEtOx_{25}$-AA, extraction with saturated $NaHCO_3$ from chloroform was necessary in order to completely remove TEA. This step affected the gravimetric yield of the reaction, as $PEtOx_{25}$ is hydrophilic and a portion of it is also retained in the aqueous phase. (Dialysis was not a safe option due to the very low molecular weight of PEtOx25.)

After purification, ^{1}H-NMR analysis in $CDCl_3$ was repeated to evaluate their chain end functionality. Figure 5.1 shows assignments for $PEtOx_{25}$-OH signals, where the terminal hydroxyl group generates a rather broad peak at 1.84 ppm. All signals generated by $PEtOx_{25}$-DDAT's protons are assigned in Figure 5.2 and Table 5.1 – Assignment of signals in the ^{1}H-NMR spectrum of $PEtOx_{25}$-DDAT (**Figure 5.2**).: measured integrals are consistent with one DDAT molecule per $PEtOx_{25}$ chain. If only a portion of chains were end-capped with DDAT, it is reasonable to expect that exposure to air humidity would introduce a –OH terminus on unfunctionalized chains; contrarily, no –OH signal is observed in the spectrum.

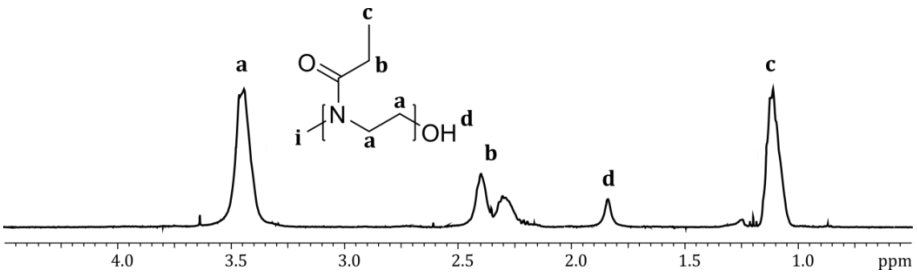

Figure 5.1 -^{1}H-NMR spectrum of PEtOx$_{25}$-OH with assignments ($CDCl_3$).

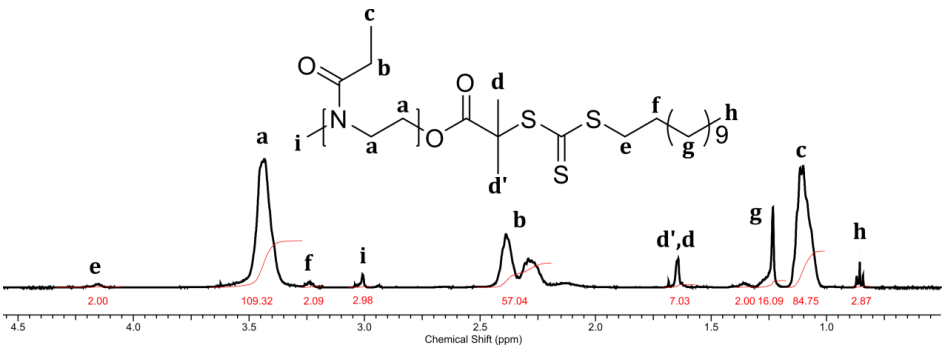

Figure 5.2 – ^{1}H-NMR spectrum of PEtOx$_{25}$-DDAT with assignments ($CDCl_3$).

Table 5.1 – Assignment of signals in the ^{1}H-NMR spectrum of PEtOx$_{25}$-DDAT (**Figure 5.2**).

Chemical shift (ppm)	Assignment	Integral
4.15	2H, e	2.00
3.70 – 3.30	100H, a	109
3.24	2H, f	2.09
3.01	3H, i	2.98
2.49 – 2.19	50H, b	57.0
1.64	6H, d+d’	7.03
1.39 – 1.18	18H, g	18.1
1.18 – 1.00	75H, c	84.7
0.86	3H, h	2.87

In the case of PEtOx25-AA, integrals of vinyl peaks of the acrylate functionality are lower than expected for complete functionalization (Figure 5.3 and TABLE), indicating that only ~75% of PEtOx chains are end-capped with AA. Despite no –OH peak is visible at 1.84 ppm, the shape of signal b is different compared to that observed in Figure 5.1 and Figure **5.2**, and its integral is larger than expected. It is possible that the –OH peak is shifted to higher chemical shifts, partially overlapping with signal b, due to sample contamination with ethanol, whose -CH_2- and CH_3- signals are visible at 3.15 and 1.37 ppm, respectively: –OH

protons are known to undergo proton exchange with other protons bound with heteroatoms, leading to a peak shift. The reason for this reduced functionalization could be ascribed to contamination of acrylic acid with water: acrylic acid was not purified by distillation prior to use in order to avoid the removal of the inhibitor it contains. Radical polymerization inhibition was indeed desired, since the functionalization reaction was carried out at 50 °C for several hours. Importantly, no free acrylic acid was observed.

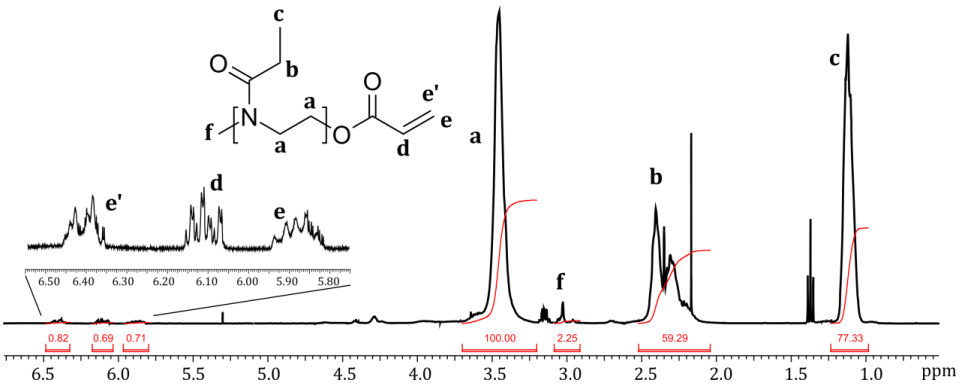

Figure 5.3 – ^{1}H-NMR spectrum of PEtOx$_{25}$-AA with assignments ($CDCl_3$).

Table 5.2 - Assignment of signals in the ^{1}H-NMR spectrum of PEtOx$_{25}$-AA (**Figure 5.3**).

Chemical shift (ppm)	Assignment	Integral
6.46 – 6.34	1H, e’	0.82
6.17 – 6.05	1H, d	0.69
5.95 – 5.81	1H, e	0.71
3.70 – 3.30	100H, a	100
3.01	3H, i	2.25
2.49 – 2.19	50H, b	59.3
1.18 – 1.00	75H, c	77.3

All samples were analyzed by GPC in THF (Figure 5.4(A)). Whereas PEtOx$_{25}$-OH shows some tailing at low molecular weights, PEtOx$_{25}$-DDAT and PEtOx$_{25}$-AA have rather symmetrical peaks with low polydispersity. The (small) difference in measured molecular weight of PEtOx$_{25}$-DDAT could be caused by the C_{12} aliphatic tail of DDAT influencing the solubility of PEtOx in THF.

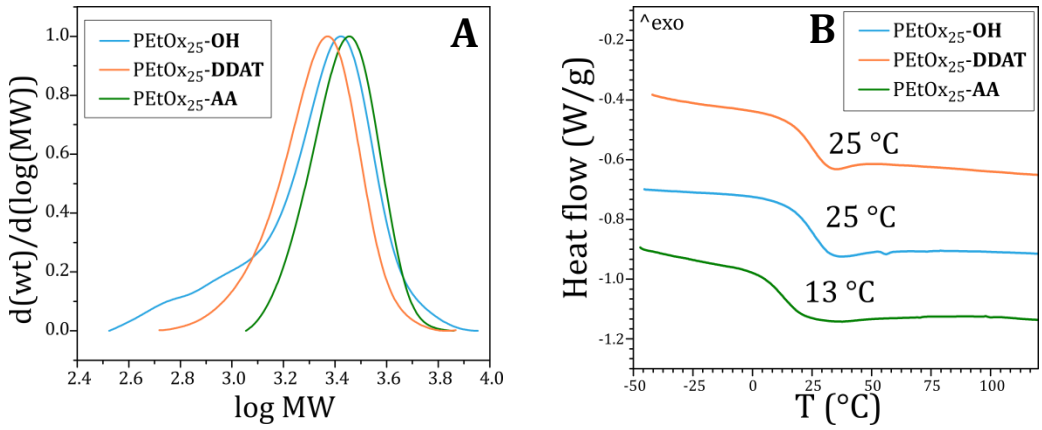

Figure 5.4 – (A) GPC curves and (B) DSC thermograms (second heating) of $PEtOx_{25}$-OH, $PEtOx_{25}$-DDAT and $PEtOx_{25}$-AA.

Tg values measured by DSC (20 K/min) are reduced with respect to the $T_{g,bulk}$ value of PEtOx (54 °C)[173] due to the polymer's low molecular weight. Surprisingly, while they are identical for –OH and –DDAT terminated PEtOx, T_g is even lower for $PEtOx_{25}$-AA. Given the very low molecular weight of PEtOx, the effect of chain end groups on chain mobility could be amplified; still, the larger dodecyl residue on $PEtOx_{25}$-DDAT would be expected to have a greater influence on thermal properties than the acrylate moiety. No exothermic event compatible with acrylate polymerization were detected in the first DSC heating scan. As will be discussed later in the Chapter, PEtOx T_g also varies significantly when incorporated in block copolymers. A more systematic study of thermal properties of low-molecular weight PEtOx is needed, yet outside the scope of this project.

5.3.2 Synthesis of $PEtOx_{25}$-*b*-PS_{50} and $PEtOx_{25}$-*b*-PS_{50}-*b*-$PtBA_{25}$

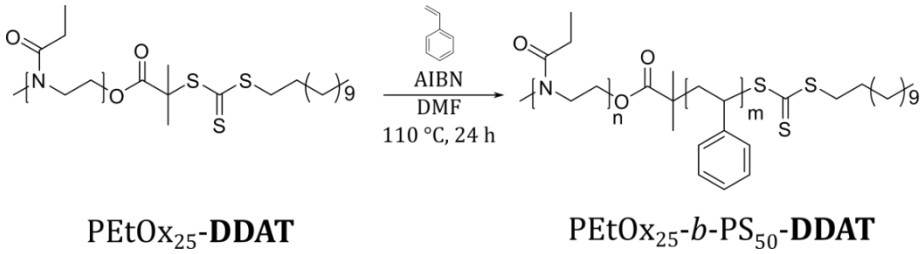

Scheme 5.2 – RAFT polymerization of PS using $PEtOx_{25}$-DDAT as macroCTA.

As-synthesized $PEtOx_{25}$-DDAT was used as a macroCTA for chain extension with hydrophobic PS (Scheme 5.2). Styrene monomer, macroCTA and initiator were added in a Schlenk flask in a [Sty]:[$PEtOx_{25}$-DDAT]:[AIBN] = 103:1:0.1 ratio, and polymerization was

carried out in DMF at 110 °C for 24 hours, targeting a 50% styrene conversion in order to preserve the macroCTA functionality for later chain extension. Conversion was calculated by ^{1}H-NMR of the crude solution, by comparing integrals of styrene monomer vinyl signals at (5.49 and 4.99 ppm) and those of PS, and was found to be 48%. ^{1}H-NMR spectrum in $CDCl_3$ of the compound after purification by dialysis against ethanol is reported in Figure 5.5.

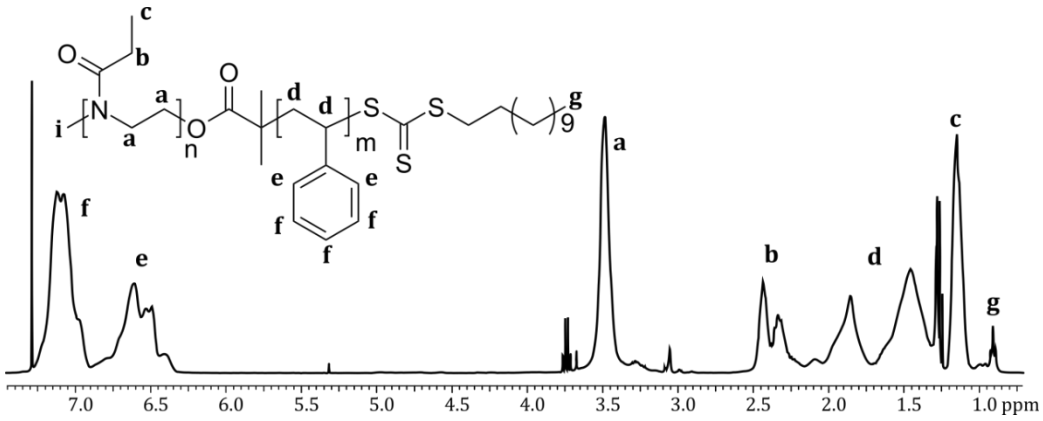

Figure 5.5 – ^{1}H-NMR spectrum of $PEtOx_{25}$-*b*-PS_{50} with assignments ($CDCl_3$).

Chain extension with *tert*-butyl acrylate (*t*BA) was carried out in DMF at 70 °C (Scheme 5.3). A [*t*BA]:[$PEtOx_{25}$-*b*-PS_{50}]:[AIBN] = 26:1:0.2 ratio was used. This time, 100% conversion was reached by allowing the solution to react overnight. ^{1}H-NMR spectrum of $PEtOx_{25}$-*b*-PS_{50}-*b*-P*t*BA_{25} after purification is reported in Figure 5.6.

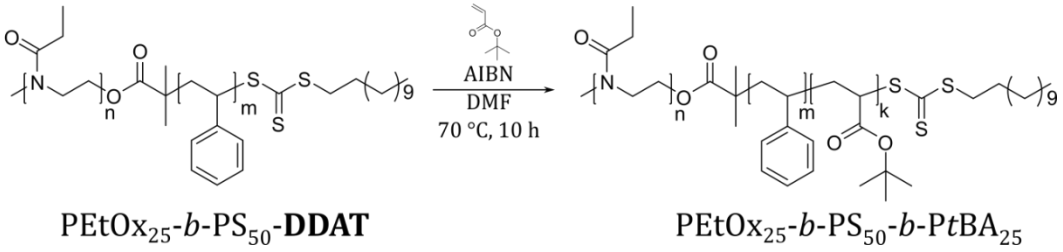

$PEtOx_{25}$-*b*-PS_{50}-**DDAT** → $PEtOx_{25}$-*b*-PS_{50}-*b*-P*t*BA_{25}

Scheme 5.3 – RAFT polymerization of *t*BA using $PEtOx_{25}$-*b*-PS_{50} as macroCTA.

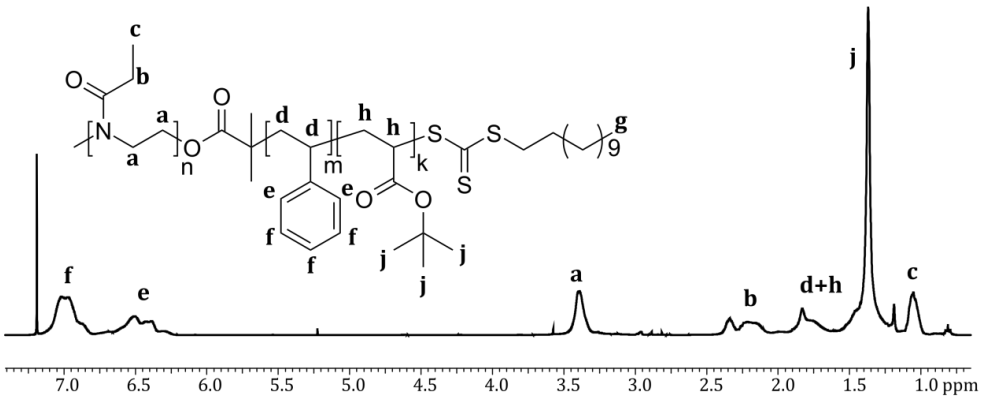

Figure 5.6 – ^{1}H-NMR spectrum of PEtOx$_{25}$-*b*-PS$_{50}$-*b*-PtBA$_{25}$ with assignments ($CDCl_3$).

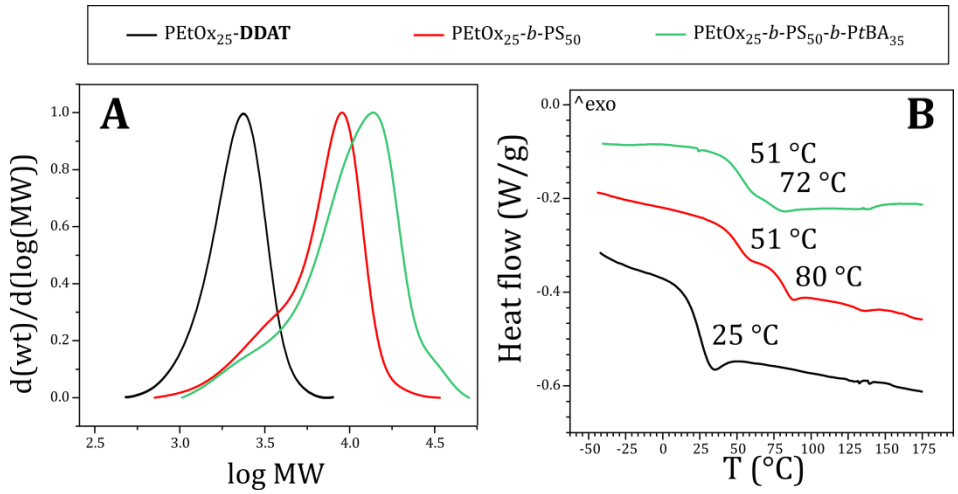

Figure 5.7 – (A) GPC and (B) DSC curves of PEtOx$_{25}$-DDAT, PEtOx$_{25}$-*b*-PS$_{50}$ and PEtOx$_{25}$-*b*-PS$_{50}$-*b*-PtBA$_{25}$.

GPC in THF (**Figure 5.7**(A)) shows a clear shift to higher molecular weights, with PDI of 1.23 for the diblock and 1.31 for the triblock, although some tailing at lower molecular weights was observed. DSC thermogram of PEtOx$_{25}$-*b*-PS$_{50}$ showed two separate glass transitions: one at 80 °C that can be assigned to the PS block (showing a reduced glass transition temperature compared to $T_{g,bulk}$(PS) = 105 °C[174] due to low molecular weight). Unexpectedly, the second T_g occurs at 51 °C, roughly double that of PEtOx$_{25}$-DDAT. After chain extension, no additional thermal event is observed, but the higher T_g is shifted to 72 °C, suggesting that P*t*BA ($T_{g,bulk}$(P*t*BA) = 43 °C) is miscible with PS in bulk. Contrarily, PEtOx and P*t*BA appear to be immiscible.

5.3.3 Self-assembly of PEtOx$_{25}$-*b*-PS$_{50}$ and PEtOx25-*b*-PS$_{50}$-*b*-P*t*BA$_{25}$

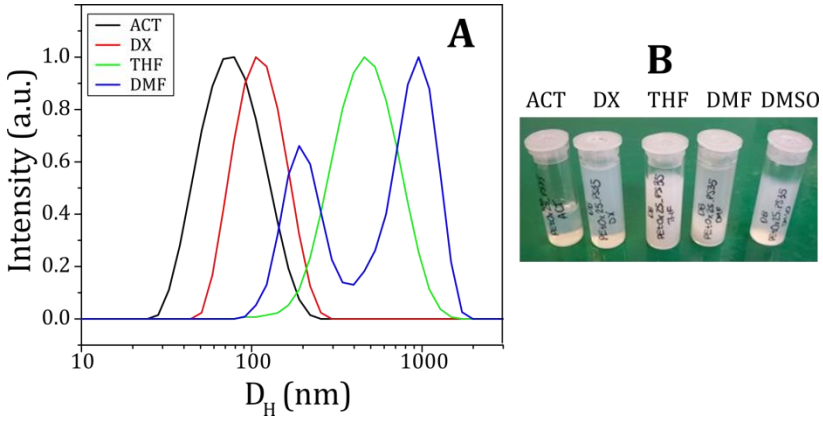

Figure 5.8 – (A) Normalized DLS intensity distributions of PEtOx$_{25}$-b-PS$_{50}$ self-assembled from ACT, DX, THF and DMF after dialysis. (B) Physical appearance of the dispersions before dialysis.

Diblock PEtOx$_{25}$-*b*-PS$_{50}$ was self-assembled from five common solvents: ACT, DX, THF, DMF and DMSO. DX, ACT and THF yielded stable nanodispersions, with size increasing in the order ACT < DX < THF (Table 5.3). Estimated interaction parameters between PS and each organic solvent by equation (6) are $\chi_{PS\text{-}ACT}$ = 1.205, $\chi_{PS\text{-}DX}$ = 0.403 and $\chi_{PS\text{-}THF}$ = 0.773. According to these data, ACT should yield the smallest particles and DX the largest, with THF in between. Yu et al.[145] also found that smaller PS-*b*-PAA particles are formed from DX compared to THF, and supported their findings by directly comparing the total (Hildebrand) solubility parameters of PS and the two solvents, a method frequently used in the literature, according to which PS has a stronger affinity with THF than with DX. It should be noted that they recorded only small differences between nanoparticle radii fabricated from different solvents; instead, we observed a 1.5-fold increase in $\langle D_H \rangle$ from ACT to DX, and a 3-fold increase from DX to THF. The relatively large values of $\langle D_H \rangle$ suggest that the formed nanoparticles are not micelles, but possibly bilayered or hierarchical structures. In fact, PEtOx volume fraction f_{PEtOx} = 0.30 (calculated using ρ_{PEtOx} = 1.14 g/mL) puts this copolymer between the "crew-cut" and the "star-like" micelle forming composition.

In opposition with PS-b-PDMA systems, DMF did not yield stable dispersions: substantial precipitation occurred shortly after stirring was interrupted (Figure 5.8(B)). Varying water addition rate had little impact on dispersion stability (see Chapter 6 for further discussion on the effect of solvent switching rate on self-assembly). PS$_{65}$-*b*-PDMA$_{10}$, a copolymer with a relatively similar molecular weight and composition compared to PEtOx$_{25}$-*b*-PS$_{50}$, was instead stable in DMF/H_2O mixtures.[85] This could be a first indication of the effect of the nature of the hydrophilic block on self-assembly, although a more

comprehensive sample set is necessary to draw any conclusion. The supernatant suspension was withdrawn and dialyzed against water: DLS showed the presence of two nanoparticle populations, one at $<D_H>_1$ = 190 nm, and the second at $<D_H>_2$ = 956 nm. In analogy to what was observed in PEO_{113}-b-PLA copolymers, DMF yielded polydisperse nanoparticles.

Finally, $PEtOx_{25}$-*b*-PS_{50} nanoparticles were not stable in DMSO/H_2O mixture, from which they quickly separated (Figure 5.8(B)). DLS measurements were also unstable and not reproducible.

Table 5.3 – Average hydrodynamic diameters and PDI values of obtained $PEtOx_{25}$-*b*-PS_{50} and $PEtOx_{25}$-*b*-PS_{50}-*b*-P*t*BA_{25} nanodispersions measured by DLS after dialysis. (a) Measurement in EtOH as selective solvent. (b) Measurement of dispersion after water addition and dialysis agains water.

Common solvent	**$<D_H>$**	**PDI**	**$<D_H>$**	**PDI**
	$PEtOx_{25}$-*b*-PS_{50}		$PEtOx_{25}$-*b*-PS_{50}-*b*-P*t*BA_{25}	
ACT	70	0.136	203	0.130
DX	106	0.086	155	0.059
THF	325	0.175	460	0.150
DMF	190, 956	polydisperse	Unstable	
DMSO	Unstable		--	
EtOH[a]	33	0.101	17, 397	
EtOH, d[b]	--		Mostly out of range	

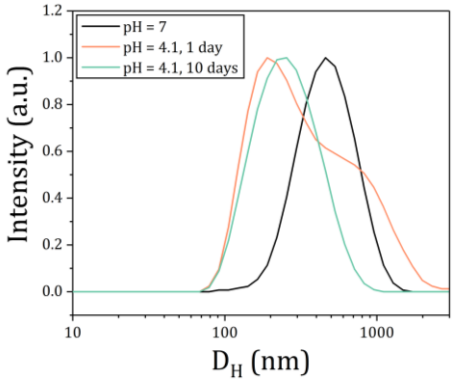

Figure 5.9 – Normalized DLS intensity distributions of $PEtOx_{25}$-*b*-PS_{50} dispersions self-assembled from THF and dialyzed against MQ at neutral pH (black line), at pH = 4.1 (orange line) and at pH = 4.1 after 10 days.

A known feature of poly(2-oxazolines) is that they can act as precursors for poly(ethylene imine)s (PEI), linear polymers bearing a secondary amine on their backbone with interesting pH and temperature sensitivity properties: linear PEIs are soluble in water at

elevated temperatures and insoluble in water at room temperature.[175] PEIs can be obtained by deacetylation of oxazoline repeating units in acidic or basic hydrolytic conditions, generally at high temperatures (> 100 °C), in a few hours.[176–178] We repeated the self-assembly of $PEtOx_{25}$-b-PS_{50} from THF and dialyzed the dispersion against a HCl solution at pH = 4.1 (molar ratio between HCl and EtOx, considering a total dispersion volume of 3 mL: 1:2.4). The dispersion was left stirring at room temperature for a few days. Due to the relatively low concentration of the acid solution and the low temperature, hydrolysis was expected to have rather slow kinetics; such mild conditions were necessary in order to avoid the risk of cleaving the ester bond linking PEtOx and PS blocks. DLS distributions obtained right after dialysis showed an asymmetrical peak possibly indicating the overlapping of two nanoparticle populations; after 10 days at pH = 4.1, only the smallest population ($<D_H>$ = 185 nm) was observed.

Self-assembly of $PEtOx_{25}$-*b*-PS_{50}-*b*-P*t*BA_{25} was studied in four different solvents. Although P*t*BA and PS are miscible in bulk in this molecular weight range, their interaction with water and organic solvents is different: the ester moiety on *t*BA units can act as a H-bond acceptor, which renders it partially soluble in protic solvents. P*t*BA total solubility parameter δ was estimated to be 16.4 $MPa^{0.5}$.[179] DLS analysis of nanoparticles obtained from ACT, DX and THF are represented in Figure 5.10(A), and average hydrodynamic diameters and PDI values are listed in Table 5.3. Overall, size increased from diblock to triblock copolymer, with the major difference in nanoparticle size being is in ACT. Triblock copolymers grant an additional degree of freedom in self-assembly from solvent switching, as selective solvents for one or two blocks can be chosen to drive it. $PEtOx_{25}$-*b*-PS_{50} proved to form stable 33 nm nanoparticles in EtOH as selective solvent for PEtOx; a sample of P*t*BA_{30}-*b*-PS_{36} also formed small micelles in EtOH, which were stable although only for a few hours. Therefore, $PEtOx_{25}$-*b*-PS_{50}-*b*-P*t*BA_{25} was dissolved in DCM as non-selective solvent (20 mg/mL), and EtOH was added dropwise at a 4 mL/h rate as a selective solvent for PEtOx and PtBA. After a volumic ratio of EtOH:DCM 1:1 was reached, DCM was allowed to evaporate under N_2 flux. DLS showed a dominant population with $<D_H>$ = 17 nm, consistent with the formation of PS cores with PEtOx/P*t*BA mixed coronas (Figure 5.10(B)). Water was then added as a selective solvent for PEtOx only: the obtained dispersion featured a higher viscosity, and most of the particles were outside the DLS measuring range (> 6000 nm).

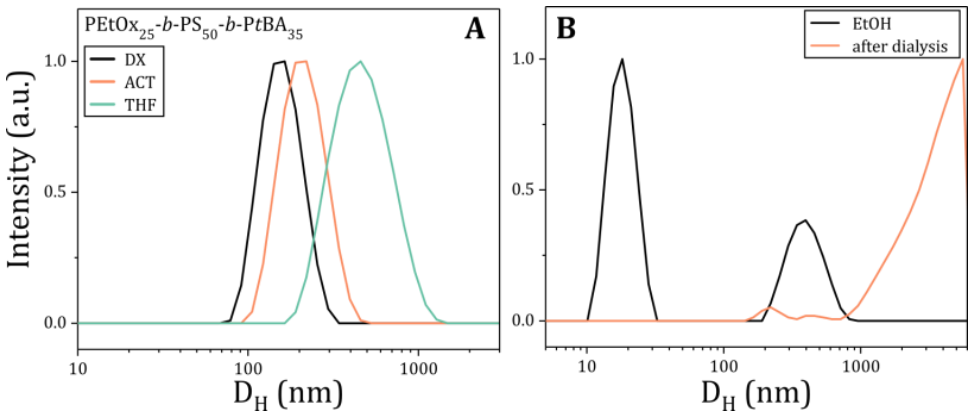

Figure 5.10 – (A) Normalized DLS intensity distributions of $PEtOx_{25}$-*b*-PS_{50}-*b*-P*t*BA_{35} dispersions obtained from DX, ACT and THF, after dialysis against water. (B) Normalized DLS intensity of $PEtOx_{25}$-*b*-PS_{50}-*b*-P*t*BA_{25} in EtOH (black line) and after water was added and EtOH was removed by dialysis (orange line).

5.4 Conclusions

Biocompatible $PEtOx_{25}$ blocks were successfully synthesized by CROP of 2-ethyl-2-oxazoline in anhydrous conditions with good control. Chain end functionalization with –OH, RAFT agent DDAT and acrylic acid was achieved by direct polymerization termination with the corresponding compounds. $PEtOx_{25}$-DDAT was used as a macroCTA for the polymerization of a hydrophobic PS block, yielding an amphiphilic $PEtOx_{25}$-*b*-PS_{50} copolymer that was self-assembled from ACT, DX, THF, DMF and DMSO. Interestingly. nanoparticle size and PDI followed the same trend observed in PEO_{113}-*b*-PLA_x nanoparticles: both characteristics increased in the order ACT < DX < THF < DMF; self-assembly from DMSO resulted in polymer precipitation. Nanodispersions from DMF were also unstable over time, with substantial sedimentation occurring after tens of minutes, although a stable suspension persisted in the supernatant mixture. $PEtOx_{25}$-*b*-PS_{50} nanoparticles evolved in time under the effect of acidic pH, with average size shrinking by a factor of 2 over a period of 10 days at a pH value of 4.1. $PEtOx_{25}$-*b*-PS_{50} was further chain extended with *tert*-butylacrylate to yield $PEtOx_{25}$-*b*-PS_{50}-*b*-P*t*BA_{25} triblock copolymer. DSC suggested that, in bulk, P*t*BA and PS blocks are miscible. Self-assembly from the same organic solvents used before yielded larger particles compared to the diblock. Using ethanol as a selective solvent for both PEtOx and PtBA, but not for PS, yielded small micelles which then underwent a dramatic transition to much larger particles upon the addition of water.

CHAPTER 6

TRPL study of the in situ incapsulation of a molecular rotor into self-assembled PS-PDMA, PEO-PLA and PEtOx-PS

6.1 Introduction

Steady-state photoluminescence spectroscopy has been a fundamental tool for the understanding of material properties for the past 150 years. Dynamic optical and energy processes have been outside its grasp until faster detectors and light sources became available, and prompted the development of a variety of techniques that could monitor the evolution of photoluminescence with time.

The sensitivity of luminescence behavior of several classes of organic dyes to specific properties of the environment that surrounds them has allowed researchers to use them as probes of the materials in which they are encapsulated. For example, surfactant and polymer critical micelle concentration (CMC) assessment in water by fluorescence measurements of pyrene (benzo[def]phenanthrene) and pyrene derivatives is now an established method in the literature[180–183]. The ratio between the first and third vibronic peaks (I_3/I_1) of pyrene emission spectra is polarity-dependent, and can therefore indicate whether the dye is in aqueous environment or located within newly formed hydrophobic cores.

Another interesting property to study is local viscosity. In the biomedical field, enhanced or reduced viscosity in cells[184] or bodily fluids compared to their physiological level is often associated with pathologic conditions. Many diseases may induce a 'thickening' or 'thinning' of blood[185–187] or lymphatic fluid[188] caused by off-balance protein levels and perturbations in diffusion of chemicals in and out of the cells. Viscosity changes are also characteristic of dynamic processes in (polymer) chemistry, i.e. monomer reaction rates, glass transitions or crystallization, or polymer swelling rates.

Molecular rotors are fluorescent molecules whose emissive properties vary as a function of the viscosity of their environment. The term 'rotor' refers to the formation upon excitation of an intramolecular twisting between at least two rigid molecular portions along the σ-bond that connects them. They typically consist of an electron-donating and an electron-accepting subunits spaced by a conjugated spacer. The latter ensures electron transfer from donor to acceptor, but prevents orbital overlapping between the two; when the molecule is photoexcited, a donor-to-acceptor charge transfer occurs, and a rotation of a subunit relative

to the other is induced by electrostatic forces. This non-emissive twisted intramolecular charge transfer (TICT) state can then relax by (i) adiabatic transition to an emissive state or (ii) non-radiative relaxation by untwisting. If local viscosity is high, intramolecular rotations are hampered, and the probability of non-radiative relaxation is reduced, resulting in longer luminescence lifetimes and quantum yields (ϕ_F).

The relationship between luminescence quantum yield and local viscosity η is described within the framework of the Förster-Hoffmann model by the following equation:

$$\log \phi_F = C + x \cdot \log \eta, \quad (7)$$

where *C* and *x* are constants related to the environment and dye, respectively.[189] Since ϕ_F is related to the excited state lifetime τ_F by:

$$\phi_F = \tau_F / \tau_0 , \quad (8)$$

where τ_0 is the rotor's viscosity-independent radiative lifetime, τ_F measurement by TRPL spectroscopy can be quantitatively related to the local viscosity of the matrix in which the rotor is located.

Local (or micro) viscosity detected by molecular rotors is related to the free volume of the surrounding fluid; an empirical relationship between the two was proposed by Doolittle[190]:

$$\eta = A \cdot \exp\left(B \frac{v_0}{v_F}\right), \quad (9)$$

where A and B are solvent-related constants, v_0 is the occupied volume and v_F is the free volume. Free volume is particularly important in amorphous polymers: the glass transition occurs when the free volume is so low as to impede chain translational mobility.

Other parameters affect the luminescence of molecular rotors: dispersant polarity, hydrogen bond formation, excimer formation. Nonetheless, rotational diffusivity is the predominant cause of ϕ_F variation if dispersant viscosity is not very low (Figure 6.1), which makes molecular rotors suitable to study polymer chain dynamics.

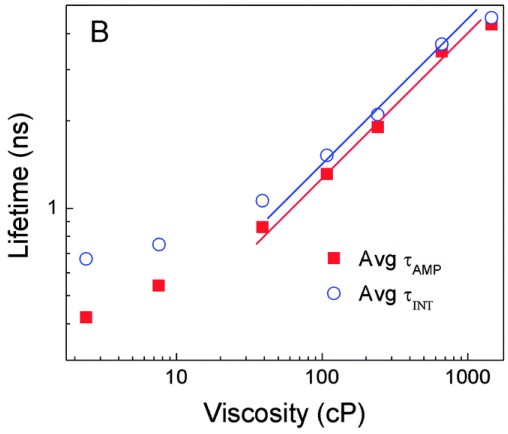

Figure 6.1 – Log/log plot of average fluorescence lifetime as a function of viscosity of homodimeric BODIPY molecular rotor in different viscosity mixtures of ethanol:glycerol. Deviation from linearity only occur for very low solvent viscosity. Reproduced from Raut et al.[191]

AzeNaph-1 characterization as a molecular rotor for self-assembly monitoring

Figure 6.2 - Structure and UV-Vis Absorption/Steady State fluorescence of AzeNaph1 in a 10^{-5} M MMA solution. shows the molecular structure, UV-Vis absorption and steady state emission of molecular rotor AzeNaph-1. AzeNaph-1 is constituted by an electron-rich dibenzoazepine unit (donor) and an electron-poor naphthaleneimide unit (acceptor), connected by a single -C–N- bond that allows for intramolecular twisting. The antiaromaticity of the azepine ring makes its N atom a particularly efficient electron donor. The rotor features a moderate luminescence quantum yield (around 20%) in organic solvents and a large Stokes shift (λ_{abs} = 410 nm, λ_{em} = 500 nm) that minimizes readsorption. Its hydrophobicity makes it insoluble in water and only sparingly soluble in alcohols.

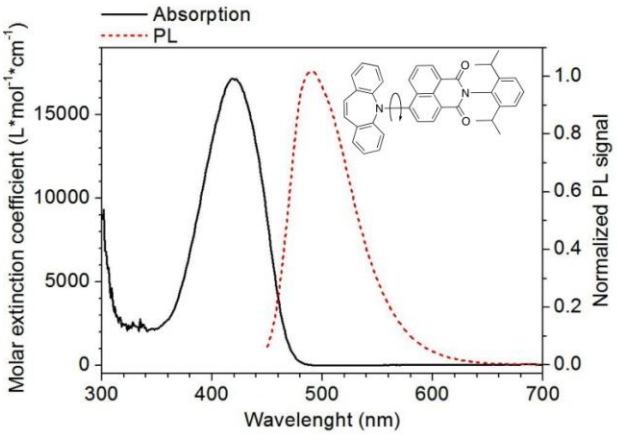

Figure 6.2 - Structure and UV-Vis Absorption/Steady State fluorescence of AzeNaph1 in a 10^{-5} M MMA solution.

Another favorable feature of AzeNaph-1 as a rotor is the sensitivity its fluorescence lifetime to local viscosity, varying from < 1 ns in liquids and rubbery polymers to 6–8 ns in glassy polymers (Figure 6.3). Furthermore, its emission decay follows a perfect single exponential in homogeneous samples, regardless of local viscosity. This aspect is of particular importance, as it allows to detect sample inhomogeneity and provide additional information compared to other commonly used molecular rotors, which exhibit biexponential decays. Finally, its large Stokes' shift prevents self-absorption.

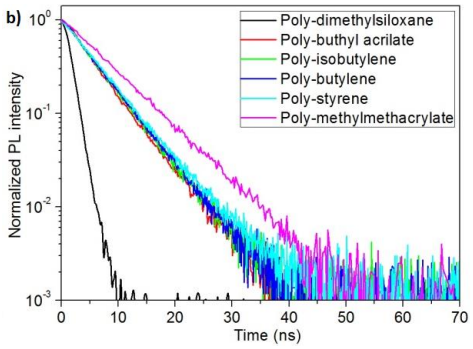

Figure 6.3 – Decay profiles of AzeNaph-11dispersed in different polymers at room temperature. Reproduced from Vaccaro et al.[84]

In conclusion, AzeNaph-1's spectroscopic properties make it a promising tool to model hydrophobic drug uptake in polymeric nanoparticles. In this Chapter, the applicability of its spectroscopic study as a characterization technique in a wider range of experimental conditions is assessed and its scope broadened. The molecular rotor was loaded into forming PS-*b*-PDMA and PEO-*b*-PLA copolymer nanoparticles during self-assembly, and the effect of non-selective solvent and rotor concentration was evaluated.

6.2 Experimental

AzeNaph-1 was added to the organic solvent of choice in a volumetric flask (final concentration: $1.885 \cdot 10^{-5}$ M), that was sealed and left stirring overnight to achieve maximum homogeneity. 10 mg of dry polymer was weighted in a flat-bottomed cylindrical glass vial. 500 µl of AzeNaph-1 stock solution was added, along with a stir bar, and left stirring in the spectroscopic setup sample holder for 20 – 30 minutes, under constant stirring. The vial was closed with a plastic cap in which a small hole was pierced to allow water addition. A 405 nm pulsed laser (100 ps pulse, overall time resolution < 1 ns) at 500 ns pulse period was used. The laser beam was attenuated by a filter and reflected on the sample vial by a mirror. The

emitted light was collimated by a lens and collected by a photomultiplier. Time-resolved spectra were collected at λ_{em} = 500 nm, and integrated over time for 20 seconds. An aliquot (35 µL) of filtered (filter pore size: 200 nm) MQ water was added to the sample vial by micrometric pipette, and the dispersion was left stirring for 2 minutes, after which a spectrum was acquired. TRPL spectra were processed and fitted with Origin 2017 software. Overall decay times were calculated by equation (10):

$$\tau_{overall} = \int_0^\infty f(t)dt = \int_0^\infty \exp\left(-\frac{t}{\tau}\right) dt, \quad (10)$$

where $f(t)$ is the normalized TRPL decay. Normalized TRPL curves were fitted with monoexponential (equation (11)) or biexponential (equation (12)) functions:

$$f(t) = \exp\left(-\frac{t}{\tau}\right) \quad (11)$$

$$f(t) = (1 - \mathrm{A}) \cdot \exp\left(-\frac{t}{\tau_{fast}}\right) + A \cdot \exp\left(-\frac{t}{\tau_{slow}}\right). \quad (12)$$

where amplitude A ranges from 0 to 1, and $\tau_{slow} > \tau_{fast}$.

6.3 Spectroscopic behavior of AzeNaph-1 in different organic solvent/water mixtures

Since block copolymer self-assembly would be carried out in mixtures of organic solvents and water, AzeNaph-1 solubility in relevant solvent mixture composition ranges were further tested.

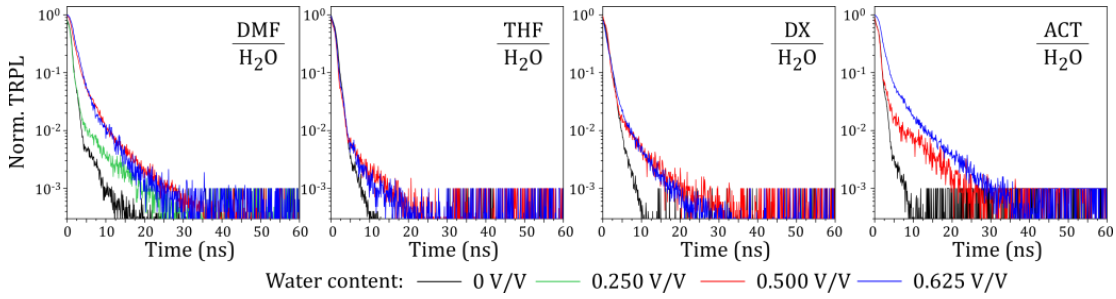

Figure 6.4 – Normalized TRPL spectra of AzeNaph-1 in the different solvent mixtures at increasing water volume fraction.

TRPL and PL spectra of AzeNaph-1 in DMF/H_2O, THF/H_2O, DX/H_2O, ACT/H_2O mixtures with increasing water content were acquired in order to exclude effects on decay lifetime caused by molecular rotor/solvent interaction. TRPL decays of AzeNaph-1 in THF/H_2O and DX/H_2O show only a small difference in decay lifetime and shape after addition of water. On the other hand, TRPL decays feature biexponential character and a longer lifetime in DMF/H_2O and ACT/H_2O at high water content (Figure 6.4). This slow component can be ascribed to the emission of crystallized AzeNaph-1 forming suspension that is somewhat

stable in the dispersant for a few hours. In fact, all samples were yellowish and noticeably turbid after the last water addition.

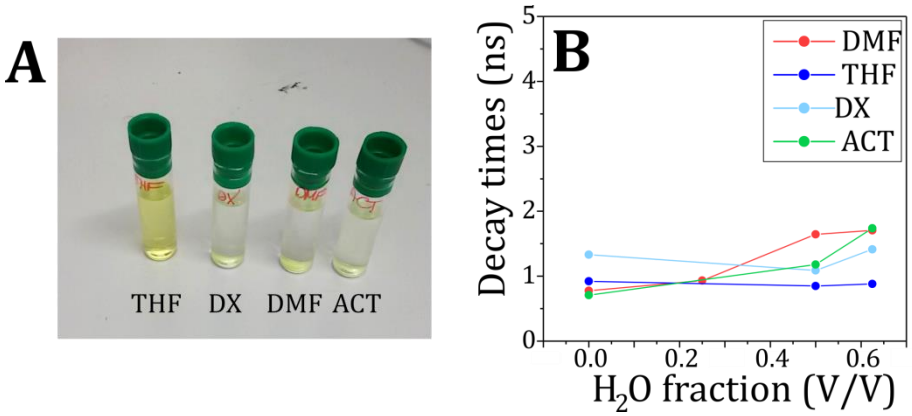

Figure 6.5 – (A) Appearance of the mixtures after sitting for the weekend (water content: 0.625 V/V). (B) Overall TRPL lifetime of AzeNaph-1 in the different solvent mixutres (scaling chosen as to facilitate comparison with lifetimes measured in the presence of self-assembling polymers).

The vials were left sitting on the bench for a few minutes; after this time, in DMF/H_2O, DX/H_2O and ACT/H_2O mixtures, AzeNaph-1 was precipitated on the bottom of the vial as a yellow solid, while the supernatant liquid was completely clear and colorless (to the naked eye). The formation of slowly decaying crystals was therefore only temporary (no signal was detected in the supernatant after precipitation). On the contrary, THF/H_2O showed little or no sediment, and the supernatant looked clear and vividly yellow (Figure 6.5(A)). This solvent composition is therefore able to dissolve AzeNaph-1, which renders this type of analytical technique risky for monitoring nanoparticle formation by nanoprecipitation from THF: since AzeNaph-1 has a favourable interaction with THF/water, confinement inside the nanoparticle is not likely, and linking its spectroscopic properties to the nanoparticles' mechanical properties would be tricky. Therefore, THF was excluded from the study. Nonetheless, AzeNaph-1 in other solvent mixtures proved to be hydrophobic enough to preferentially go into the particle rather than in the solvent.

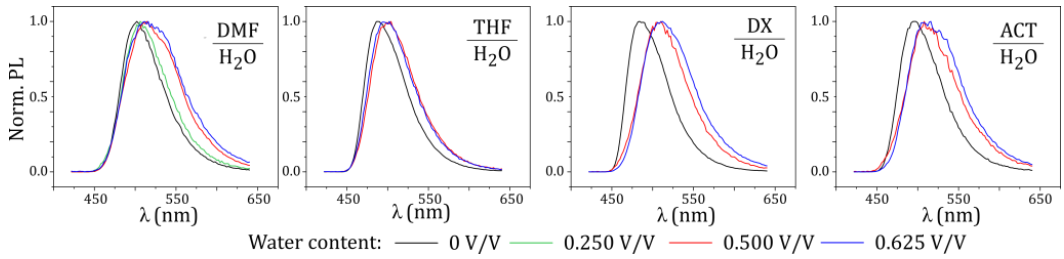

Figure 6.6 - Normalized PL spectra of AzeNaph-1 in different solvent mixtures at increasing water volume fraction.

PL spectra showed in all cases a red shifted emission from TCIT states, due to the increased viscosity of the solvent mixture (Figure 6.6).

6.4 AzeNaph-1 as a model hydrophobic load

Table 6.1 lists the polymeric sample set used for this study, which includes several PS-*b*-PDMA and PEO-*b*-PLA samples with different composition, with a focus on predominantly hydrophobic diblocks. Since AzeNaph-1 is hydrophobic, the importance of the length of the core-forming block is clear. However, nanoparticle morphology can also affect crucial parameters, namely local chain mobility, core size and rotor uptake; vice versa, rotor loading into the forming nanoparticle can affect its size and shape. Please refer to assumed morphologies in the relevant Chapters. Moreover, the corona-forming blocks cannot be excluded as possible loading sites: despite being hydrophilic compared to the core-forming block, they are aprotic and bear both hydrophilic and hydrophobic portions. The polar side groups of PDMA are analogous to DMF, and PEO is a polyether, and could behave locally in a similar fashion to cyclic ether solvents such as THF and DX; DMF, THF and DX are all good solvents for AzeNaph-1. Ideally, the hydrophilic block will be ever more solvated by water molecules while water is added to the dispersions, which should force AzeNaph-1 molecules out of the corona – either in the continuous phase (from which they will readily precipitate) or into the core. However, chain density of the tethered hydrophilic block at the interface with the nano-sized core can be high enough to favour polymer-polymer interactions over polymer-water interactions; in this region, encapsulation of AzeNaph-1 is possible.

Table 6.1 – Samples used for the investigation of incorporation of molecular rotor AzeNaph-1. Synthesis and characterization is described in detail in previous Chapters. (a) Volumic fraction of the hydrophilic block.

Sample	**M_w (g/mol)**	**f_{hydro}[a]**	**T_g (°C)**	
PS_{81}-*b*-$PDMA_{17}$	10900	0.15	53	
PS_{81}-*b*-$PDMA_{35}$	12500	0.26	95	115

PS_{273}-*b*-$PDMA_{86}$	34600	0.23	98
PS_{394}-*b*-$PDMA_{75}$	54700	0.14	105
PEO_{113}-*b*-PLA_{300}	26930	0.19	19
PEO_{113}-*b*-PLA_{400}	35000	0.15	32
PEO_{113}-*b*-PLA_{500}	39960	0.13	33
PEO_{113}-*b*-PLA_{600}	48200	0.11	38
PEO_{113}-*b*-PLA_{1300}	102830	0.05	45

10 mg of copolymer and AzeNaph-1 were dissolved in 500 µL of DMF ([AzeNaph] = $1.88 \cdot 10^{-5}$ M). The solution was left stirring for 20 to 30 minutes to achieve complete polymer dissolution. Then, aliquots 35 µL of filtered MQ water were added, and the dispersion was allowed to stir for 2 minutes to homogenize. After this time, a TRPL spectrum was acquired.

6.4.1 PS-*b*-PDMA in DMF/H_2O and DX/H_2O

In this case, copolymers with the same building blocks as those used in Vaccaro et al.[84] were used. The fundamental difference lies both in their overall molecular weight and their internal composition: in the published paper, the predominance of the hydrophilic PDMA fraction in PS_{105}-*b*-$PDMA_{817}$ constrained the PS blocks in a small solid core which behaved like bulk PS. TEM imaging showed that the nanoparticle morphology was indeed that of 'star-like', fairly monodisperse micelles. The samples selected for this study, on the contrary, assume more exotic morphologies: PS_{81}-*b*-$PDMA_{17}$ forms bicontinuous sponge-like structures, while PS_{81}-*b*-$PDMA_{35}$ and PS_{394}-*b*-$PDMA_{75}$ favour hierarchical, higher order self-assembly. PS_{273}-*b*-$PDMA_{86}$ forms crew-cut micelles, where cores are larger than those of "star-like" micelles with the same hydrophobic block length, and the elastic strain in the core cannot be completely balanced by hydrophilic block solvation. AzeNaph-1 allows for direct monitoring of subtle variations during the self-assembly process that would in some cases be hard to achieve: DLS gives limited insight when the formed particles are very large (> 500 nm), because their intense scattering renders the monitoring of unimers and smaller micelles often impossible.

A typical set of TRPL spectra acquired at different volume fractions is reported in Figure 6.7: AzeNaph-1 decay lifetime in the dissolved state is very close to the experimental setup detection limit (~1 ns). In the case of PS-*b*-PDMA samples in DMF, a long decay lifetime contribution immediately emerged upon the addition of water. Its decay lifetime (τ_{slow} = 7 ns) remained largely constant, while its amplitude and contribution to the overall decay increased. In this phase, the fast component had in most cases also a relatively constant decay time (τ_{fast}

~1.2 ns), consistent with that of 'free', dissolved AzeNaph-1. Since AzeNaph-1's emission is monoexponential in homogeneous environments, the two contributions to total decay can be assigned to two different AzeNaph-1 populations: one in the mixed solvent phase (τ_{fast}) and one inside the forming polymeric nanoparticles (τ_{slow}). The latter experienced its polymer surroundings (PS) as if they were identical to glassy, bulk PS (see Vaccaro et al.[84] Supporting Info). This provides two pieces of information: that PS cores behave as glassy from the first one or two water aliquots added, and that AzeNaph-1 is progressively being loaded into the nanoparticles with increasing water content.

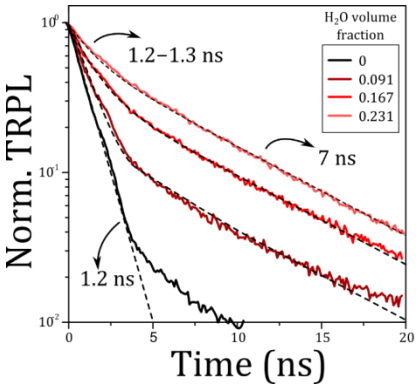

Figure 6.7 – Selected TRPL curves of AzeNaph-1 in PS_{273}-*b*-$PDMA_{86}$/DMF/H_2O at different water contents. Dashed lines trace mono- or biexponential function fits.

Biexponential fitting of TRPL curves with eq. (12) provides the amplitudes of the polymer-loaded AzeNaph-1 decay contributions (A_{slow}), which are plotted as a function of water content in Figure 6.8 for all PS-*b*-PDMA samples. A_{slow} increased quickly until a water volumic fraction of ~0.350 was reached, after which it reached a plateau. While in PS_{81}-*b*-$PDMA_{35}$, PS_{81}-*b*-$PDMA_{35}$ and PS_{273}-*b*-$PDMA_{86}$ A_{slow} was fairly constant over the remaining water content range, a positive slope remained in PS_{394}-*b*-$PDMA_{72}$. This sigmoid trend was directly reflected in the overall decay lifetime $\tau_{overall}$. The shape of the A_{slow} and $\tau_{overall}$ vs. H_2O curves is identical in all cases, the main difference being the plateau levels.

A_{slow} should not be confused with the fraction of aggregated polymer chains with respect to unimers: while the emergence of the τ_{slow} component and the presence of the self-assembling polymer are undoubtedly connected, meaning that AzeNaph-1's behaviour is caused by its encapsulation in the polymer, nanoparticle formation does not necessarily give rise to a well-defined slow component in the overall decay. Moreover, the fast component may not be generated by unencapsulated rotors, but rather by populations of rotor detecting a lower local viscosity.

Even at maximum water content, A_{slow} never reached 1. This was true also in the case of "star-like" PS_{105}-*b*-$PDMA_{800}$, where, however, it exceeded 0.9. The maximum value of Aslow was ~0.8 for PS_{394}-*b*-$PDMA_{75}$ and PS_{273}-*b*-$PDMA_{86}$, while it was only 0.3 and 0.4 for PS_{81}-*b*-$PDMA_{35}$ and PS_{81}-*b*-$PDMA_{17}$, respectively. The fast component had a longer decay time than that of free rotor: a biexponential fit yielded τ_{fast} = 3.5 ns and 3.1 ns, respectively (Figure 6.8(B)). Interestingly, classification of these results can be made on the basis of morphology more than other parameters like f_{PDMA} and molecular weight: PS_{273}-*b*-$PDMA_{86}$, which forms rather monodisperse micelles, and PS_{394}-*b*-$PDMA_{75}$, which predominantly forms micelles, are more rigid than bilayer and worm/compound micelle forming PS_{81}-*b*-$PDMA_{17}$ and PS_{81}-*b*-$PDMA_{35}$.

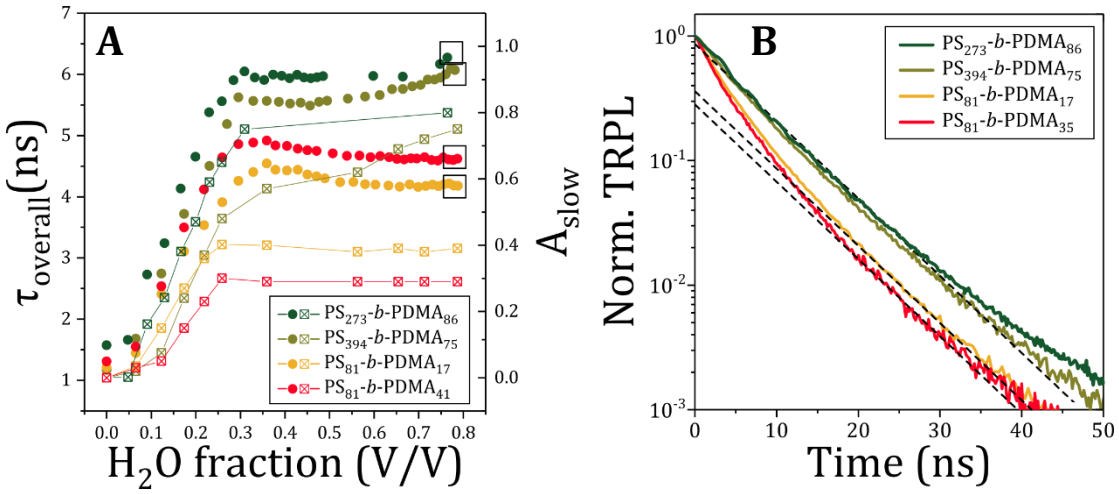

Figure 6.8 – (A) Overall decay lifetime and slow component amplitude of AzeNaph-1 in PS-*b*-PDMA/DMF/H_2O dispersions at different water content. (B) AzeNaph-1 TRPL spectra at maximum water content (indicated as a square in the left panel). Dashed lines represent monoexponentials governed by τ_{slow} = 7 ns.

The presence of a faster component in the luminescence decay hints at the presence of a separate AzeNaph-1 population experiencing a lower local viscosity. The region of higher mobility could be inside the core, close to the interface with the corona, and generated by the soft confinement effect induced by the solvated hydrophilic block. As mentioned in the introduction to this Chapter, the thickness of this high mobility shell can be of a few nm, within which viscosity can be considered to be either lower than $T_{g,bulk}$ and constant, or gradually decreasing from $T_{g,bulk}$ values close to the glassy core to the reduced Tg of the core-corona interface. In the former case, AzeNaph-1 decay is expected to be biexponential, while in the latter a multiexponential or a stretched exponential function should be a more appropriate fit for the fast component; however, the two cases are virtually indistinguishable. An alternative location is the corona, as discussed at the beginning of this section. This seems

to be a less likely option, given the low f_{PDMA} and low m_{PDMA} of the two samples. A third possible explanation to the enhanced mobility is swelling of nanoparticle cores by residual DMF: due to the favorable polymer-DMF interaction, some DMF could remain in the PS core upon nanoprecipitation, swelling it to some degree; if this were the case, it would mean that there is a DMF concentration gradient within the core, since the presence of the 7 ns decay component suggests that part of the polymer is indeed glassy. Nevertheless, in this framework it is difficult to justify the absence of a similar fast component in PS_{394}-*b*-$PDMA_{75}$ and PS_{273}-*b*-$PDMA_{86}$.

Higher PS mobility could be consistent with the formation of worms, which are the result of non-elastic collision between micelles, and with the formation of large bicontinuous networks prone to collapse.

We further investigated the effect of the non-selective solvent on the viscosity of PS-*b*-PDMA nanoparticles. Since ACT is not a very good solvent for PS, only DX was tested for low molecular weight PS_{81}-*b*-$PDMA_{17}$. Obtained TRPL curves for different water contents are shown in Figure 6.9(A): again, curves can be fitted with a biexponential function comprising a fast and slow component with fixed lifetime (τ_{slow} = 5.8 ns), similarly to what was observed in DMF. $\tau_{overall}$ and A_{slow} were therefore calculated, and are compared to results in DMF in Figure 6.9(B): the onset of $\tau_{overall}$ increase is shifted to higher water contents, but its slope is quite similar to that in DMF. It appears that while aggregation is delayed, chain dynamics are largely unchanged between the two solvents. A final saturation of the self-assembling phenomenon is reached when water content exceeded 0.6 V/V. A_{slow} in DX plateaus at 0.8, more than double the value obtained in DMF.

Interaction parameters of core-forming PS block with the non-selective solvent can be calculated from Hansen's solubility parameters of PS (δ_D = 21.3 $MPa^{0.5}$, δ_P = 5.8 $MPa^{0.5}$, δ_H = 4.3 $MPa^{0.5}$, δ_T = 22.5 $MPa^{0.5}$), yielding $\chi_{PS\text{-}DMF}$ = 1.737 and $\chi_{PS\text{-}DX}$ = 0.472: since interaction with DX is stronger, a larger amount of water is necessary to trigger PS nanoprecipitation in nanoparticle cores, which explains the shifted aggregation onset or, in other words, a higher critical water concentration (cwc) as addressed to by Yu et al.[145] A better solvent affinity, did not bring about significant changes in viscosity variation as a function of water content; nonetheless, the much larger population of AzeNaph-1 with a long decay time suggests that a larger portion of the core is glassy at the end of the self-assembly process. DLS distributions of dispersions obtained after TRPL experiments are shown in Figure 6.9(C): both average hydrodynamic diameter ($\langle D_H \rangle_{DX}$ = 419 nm, $\langle D_H \rangle_{DMF}$ = 483 nm) and PDI values (PDI_{DX} = 0.124, PDI_{DMF} = 0.114) are similar in DMF and DX, indicating that a similar morphology is assumed. Nanoparticle size is slightly larger in DMF compared to DX, which contrasts with

the size trend reported by Yu et al.; it should be noted, though, that particle morphology in this case is not that of crew-cut micelles (see Chapter 3, Figure 3.4).

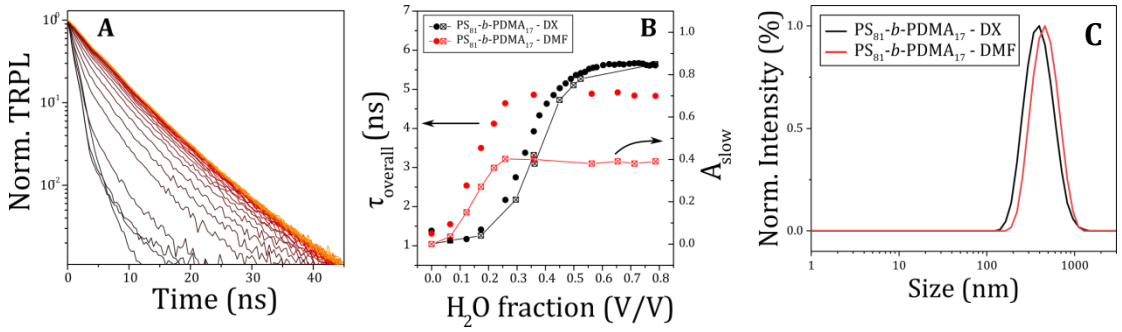

Figure 6.9 – (A) TRPL curves of AzeNaph-1 in PS_{81}-*b*-$PDMA_{17}$ self-assembled from DX. (B) Calculated $\tau_{overall}$ and A_{slow} values for PS_{81}-*b*-$PDMA_{17}$ self-assembled from DX (black cricles/crossed squares), compared with data obtained in DMF. (C) DLS normalized intensity distributions of AzeNaph-1 containing PS_{81}-*b*-$PDMA_{17}$ nanoparticles obtained from DX (black line) and DMF (red line). DLS data was processed considering a corrected viscosity of 1.282 mPa·s and 1.4623 mPa·s for DX/H_2O[192] and DMF/H_2O solvent mixtures, respectively.

6.4.2 PEO_{113}-*b*-PLA in DMF/H_2O, ACT/H_2O and DX/H_2O

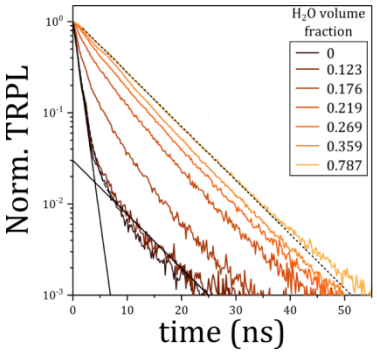

Figure 6.10 – Selected TRPL curves of AzeNaph-1 in PEO_{113}-*b*-PLA_{600}/DMF/H_2O at different water contents. Dashed lines trace monoexponential function fits. [AzeNaph-1] = $1.88 \cdot 10^{-5}$ M.

The same study as described above was repeated in the presence of a set of PEO_{113}-*b*-PLA_x samples. The glass transition temperature (T_g) of the hydrophobic PLA block close to room temperature (Table 6.1), so the rigidity of the environment in which AzeNaph-1 is enclosed may not be necessarily very high. It should be noted that the measured T_g is that of the diblock copolymer, and could be lowered by the bulk miscibility between PEO and PLA; when phase separation occurs in water, PLA's T_g may be higher, and closer to $T_{g,bulk}$(PLA) ~ 60 °C. Water was added as to mimic the action of a syringe pump operating at a flow rate of 1.0 mL/h (starting polymer solution volume: 0.5 mL): this is equal to a 4-fold decrease in

water addition rate compared to the procedure used for the preparation of nanodispersions whose DLS intensity distributions are reported in Chapter 4, Figure 4.7; the goal was to decouple the effect of kinetic 'freezing' of polymer chains due to the relatively fast water addition rate of 4 mL/h and the solvent/polymer interaction.

First, we studied the whole set sample set in DMF/H_2O mixtures. A spectrum was acquired after each subsequent addition of water in the initially clear polymer solution (Figure 6.10). Similarly to what was described in the previous section, a slowly decaying emission component appeared and gradually increased until it completely dominated the overall luminescence event. The major change in decay lifetime occurred in the water fraction range comprised between 0.20 and 0.35, after which a lifetime increase continued at a much slower rate. A small variation of the onset of lifetime increase was detected, which is anticipated to lower water contents in PEO_{113}-*b*-PLA_{600} and PEO_{113}-*b*-PLA_{1300} (**Figure 6.11**). This suggest that a larger PLA block could facilitate AzeNaph-1 loading into the nanoparticles at lower solvent polarity. τ_{slow} values are identical to those measured in glassy PS, and all TRPL curves followed a completely monoexponential decay (τ_{slow} = 7 ns, A_{slow} = 1) at the maximum water content, evidencing no difference within the sample set. These are indications that PLA cores behave as glassy, regardless of PLA molecular weight and morphology, consistently with a hard confinement regime.

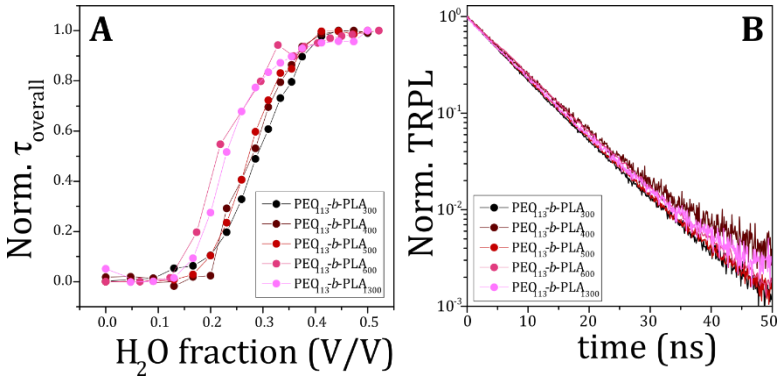

Figure 6.11 – (A) Comparison of $\tau_{overall}$ plots as a function of water content for the investigated PEO_{113}-*b*-PLA_x samples. Lifetime curves were normalized to aid comparison. (B) TRPL curves at maximum water content.

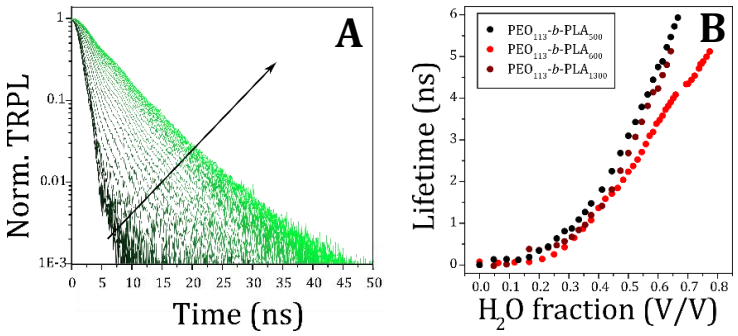

Figure 6.12 – (A) TRPL curves for PEO_{113}-b-PLA_{600} from ACT at water content increasing in the direction of the black arrow. (B) $\tau_{overall}$ as a function of water content for PEO_{113}-*b*-PLA_{500}, PEO_{113}-*b*-PLA_{600} and PEO_{113}-*b*-PLA_{1300} from ACT.

For selected samples, measurements were repeated using ACT as a starting non selective solvent. Figure 6.12(A) shows TRPL curves obtained at different water volumic fractions; qualitatively, the trend is quite different compared to that observed in DMF, as no single slow component can be discerned. On the contrary, AzeNaph-1's overall decay is the sum of three or more exponentials. This conflicts with the simple model employed so far, that considers two separate rotor populations, of which one experiences a homogeneously rigid environment. The absence of this population's emission may indicate that there is no homogeneously rigid environment in the forming nanoparticles, but rather a gradient of local viscosities presumably decreasing outwardly from the nanoparticle core center. The increase in overall lifetime indicates that, overall, local viscosity is also increasing with increasing water content, but no *homogeneously* viscous domains are formed.

Since a biexponential fitting would be hardly meaningful, only $\tau_{overall}$ was calculated (Figure 6.12(B)). While the lifetime increase onset corresponds roughly to that found in DMF, its slope is much lower, and no plateau was reached in the water content range used for the experiments, suggesting that AzeNaph-1 always lives in a lower viscosity environment compared to the analogous situation in DMF. Differences between samples with varying PLA block lengths are small.

An explanation of these data could be found in the plasticizing effect that ACT has on PLA cores. Similarly to what was described above for PS-*b*-PDMA/DMF, ACT may accumulate in PLA and 'delay' its transition to a glassy state. In order to compare the tendency of each solvent to remain in the PLA core, affinity of the solvent with PLA and with water were considered. Interaction parameters between non-selective solvent and water ($\chi_{S\text{-}H2O}$) and between PLA and solvent ($\chi_{PLA\text{-}S}$) were calculated according to equation (6) (see Chapter 4, Table 4.3). The lowest the χ, the strongest the affinity between the components.

Since $\chi_{DMF-H2O} < \chi_{ACT-H2O}$, DMF is expected to diffuse more readily into the water-rich solvent mixture than ACT, thanks to its enhanced affinity with water. On the other hand, since $\chi_{PLA-DMF} > \chi_{PLA-ACT}$, ACT is expected to have a stronger affinity with PLA, and thus a higher tendency to remain in the polymer-rich nanoparticle. If the concentration of ACT is not constant in the whole core volume (as is reasonable since it's governed by diffusion through the polymer into the solvent mixture), T_g would also vary within it, giving rise to the multiexponential emission of loaded AzeNaph-1.

Since solvent diffusion is time-dependent, a time-dependent viscosity should also be observed. Experiments were repeated on PEO_{113}-*b*-PLA_{600}: water aliquots were added to the polymer solution until a specific water content was reached; then, TRPL spectra were acquired as a function of time, and corresponding $\tau_{overall}$ values were calculated. As a comparison, the same procedure was applied using DMF as a non-selective solvent.

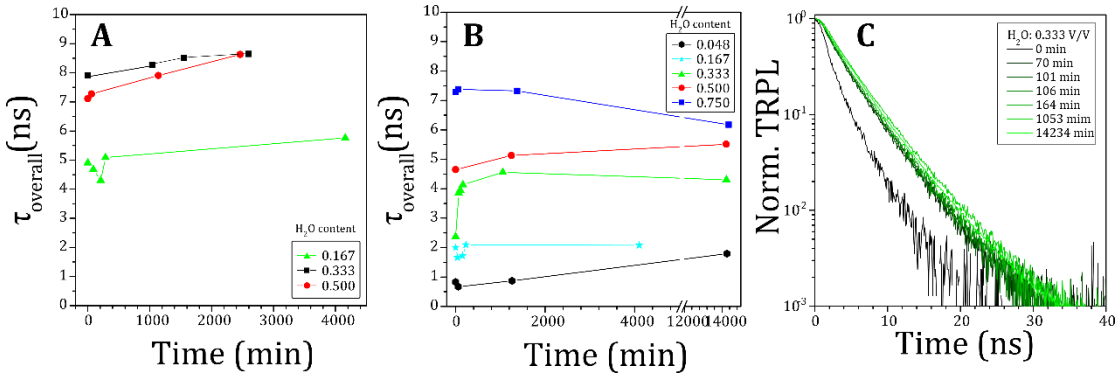

Figure 6.13 – $\tau_{overall}$ values at different water contents as a function of time for PEO_{113}-*b*-PLA_{600} using (A) DMF and (B) ACT as a starting solvent. (C) TRPL decays for PEO_{113}-*b*-PEO_{600}/ACT/H_2O at a water content of 0.333 V/V.

$\tau_{overall}$ in ACT is constant (within experimental error) with time for water contents up to 0.167 V/V (**Figure 6.13**(B)). At a water volumic fraction of 0.333, instead, a significant evolution of $\tau_{overall}$ with time was observed: a 2 ns jump in 70 minutes was followed by a further small increment over the following days (**Figure 6.13**(C)). A repetition of the same experiment at 0.333 V/V water content yielded comparable results. Interestingly, the described behavior was hardly detectable for higher water fractions, suggesting that an increased water content and a longer stirring time have a similar effect on AzeNaph-1's luminescence evolution.

In order to evaluate the time dependency of self-assembly from ACT, PEO_{113}-*b*-PLA_{500} was dissolved once again in ACT and water aliquots were added at a rate 30 times slower, maintaining a constant stirring, up to a water fraction of 0.5 V/V. Figure 6.14(B)

shows calculated $\tau_{overall}$ values in the two instances: local viscosity detected by AzeNaph-1 increases much more rapidly with water content when water is added slowly. Or rather, the same values of local viscosity are reached at a lower water content when the dispersion is allowed to stir undisturbed for a longer time; as a result, the polymer/rotor system persists in a relatively mobile state during most of the self-assembly process when a faster addition rate is used. By extension, one can reasonably expect an even slower process happening at the rate of 4 mL/h used for the preparation of PEO-*b*-PLA nanodispersions described in Chapter 4.

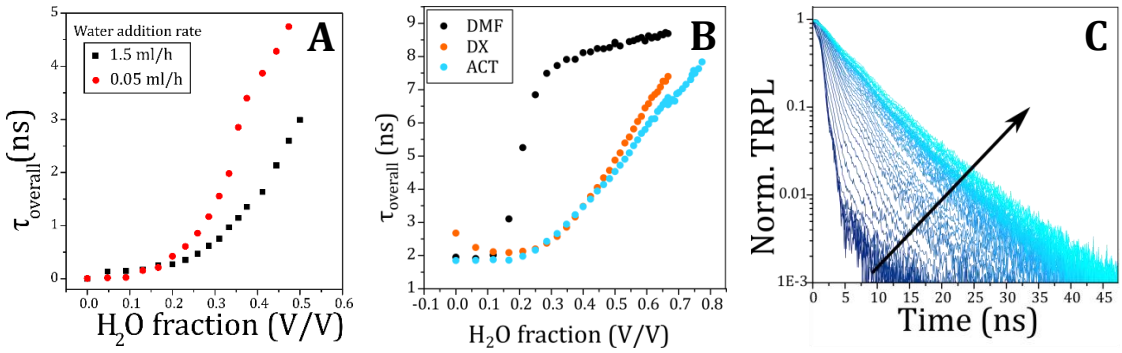

Figure 6.14 – (A) $\tau_{overall}$ values versus water content for PEO_{113}-*b*-PLA_{500} from ACT at different water addition rates. (B) Overall decay times of TRPL curves of AzeNaph-1 for PEO_{113}-*b*-PLA_{600} in DMF, DX and ACT mixtures as a function of water content. (C) TRPL curves for PEO_{113}-b-PLA_{600} from DX at water content increasing in the direction of the black arrow.

It should be highlighted that this is a solvent-induced effect, as AzeNaph-1 luminescence both in PEO-*b*-PLA and PS-*b*-PDMA systems doesn't exhibit any significant time dependency (see **Figure 6.13**(A) and Figure S10 in Vaccaro et al.[84]) when DMF is used.

Presented data seem to be consistent with the hypothesis involving the presence of core-swelling ACT slowly diffusing out of the nanoparticle, and so are the relevant time scales (tens of minutes). Nevertheless, rather surprisingly, DX had an almost identical effect on AzeNaph-1 luminescence in PEO_{113}-*b*-PLA_{600}: no constantly slow component could be recognized in TRPL curves, and $\tau_{overall}$ as a function of water content was practically superimposable to that obtained in ACT (Figure 6.14(B,C)). In this case, considerations involving Flory-Huggins interaction parameters between DX and water ($\chi_{DX\text{-}H2O}$) and PLA and DX ($\chi_{PLA\text{-}DX}$) only partially support the core-swelling hypothesis: whereas $\chi_{DX\text{-}H2O} \sim \chi_{ACT\text{-}H2O} > \chi_{DMF\text{-}H2O}$ (hence diffusion of DX to the water-rich phase is retarded compared to DMF while it's very similar to ACT), $\chi_{PLA\text{-}DX}$ is the highest among the solvents, which should make DX the worst good solvent for PLA, reducing the amount of DX swelling the core. It should

be noted that Hansen's method of calculation of interaction parameters assigns to dispersion forces a dominant role in polymer solvation thermodynamics (see equation (6)). Experimentally, DMF was found to be unable to completely dissolve PLA by Sato et al., although considerable swelling was observed; on the other hand, DX and ACT were able to dissolve it.[193] Both Hansen's solubility theory and PLA solubility measurements consider binary, solvent-polymer systems only; even disregarding the hydrophilic block entirely, and assuming that the core-forming block and water completely repel each other, the presence of water may complicate the interaction between the organic solvent and the core-forming block. For example, PS and PDMA are soluble in DX – in fact, PS-*b*-PDMA samples were synthesized in dry DX (see Chapter 3). Yet, solvent switching from DX to water by the same methodology used for TRPL experiments lead to considerable copolymer precipitation in white flakes even at very low water contents (< 0.300 V/V) for medium and high PS block molecular weights (namely, PS_{394}-*b*-$PDMA_{75}$ and PS_{273}-*b*-$PDMA_{86}$). Only PS_{81}-*b*-$PDMA_{17}$ was able to form a stable dispersion with no sediment (see below).

However, keeping all these factors in consideration, TRPL results are consistent with the nanoparticle size pattern we identified for PEO_{113}-*b*-PLA_x in Chapter 4. In particular, both techniques show that ACT and DX give rise to similar properties (DLS: similarly small and monodisperse nanoparticles; TRPL: similarly low and inhomogeneous overall nanoparticle viscosity), whereas DMF brings about different features (DLS: large, polydisperse objects; TRPL: very sharp viscosity variation, immediate formation of a hard core). Chain mobility and nanoparticle size are related, and several authors have argued that a higher mobility allows polymer chains to respond to changes in solvent polarity by rearranging more freely into structures that minimize their free energy, leading to better dispersions. Solubility parameters are generally used to justify these results,[123,145] while the presented technique allows to directly monitor the degree of nanoparticle mobility during formation, avoiding the shortcomings of solubility theories as discussed above.

6.5 Conclusions and future work

In conclusion, AzeNaph-1 was used as a fluorescent local viscosity probe for the *in situ* monitoring of block copolymer self–assembly in water from different organic solvents. The applicability of the technique was assessed in DMF, DX, ACT and THF for a set of PS-*b*-PDMA and PEO-*b*-PLA systems. AzeNaph-1 was successfully encapsulated into PS as well as in PLA cores. In PS-*b*-PDMA copolymers, encapsulated rotor molecules indicated the

presence of uniformly rigid domains within the forming nanoparticles *via* the appearance of a slowly decaying second emission in their TRPL spectra. Evolution of AzeNaph-1 TRPL as a function of water content in PS-*b*-PDMA was similar both in DMF and DX, though the onset of lifetime change was shifted to higher water contents when DX, a better solvent for PS compared to DMF, was used. Similar results were obtained in PEO_{113}-*b*-PLA_x samples in DMF, where evidence of rigid domains formation was also observed, despite the PLA blocks' T_g measured by DSC being close to room temperature. On the contrary, ACT and DX yielded strikingly different results: overall luminescence lifetime increased gradually with increasing water content, but much more slowly compared to DMF; more interestingly, no biexponential behavior was observed, indicating that no homogeneously rigid domain was formed in the nanoparticle. As a result, local core viscosity was much lower in ACT and DX than in DMF over the whole water fraction range. Unlike in DMF, a temporal evolution of TRPL at constant water content was also detected: in particular, a slower water addition rate (under constant stirring) yielded higher decay lifetimes at lower water contents. This suggests that the reduced core viscosity was due to a stronger PLA-solvent interaction, causing an accumulation of solvent in the core; as solvent slowly diffused out of the nanoparticle and into the water-rich phase, its plasticizing effect gradually disappeared.

Our results are in agreement with previously reported data on the effect of the non-selective solvent on block copolymer self-assembly, but offer a more direct and *in situ* observation of chain arrangement as a response to non-solvent addition; these aspects are typically inferred from polymer solvation theories, which have limited applicability in this complex setting, and can sometimes lead to conflicting considerations.

CHAPTER 7

Polymerization-Induced Self-Assembly (PISA) of (PAGA-*b*-PBA)

7.1 Introduction

Carbohydrates are known to play a crucial role in a multitude of fundamental functional biological processes involving cellular interaction, both physiological and pathological: from signal transmission and fertilization to inflammation, viral infection and cancer cell proliferation by metastasis.[194–196] This outstanding variety of functions is implemented *via* specific interactions with protein receptors expressed on the cellular membrane. The density of information conveyed by carbohydrates exceeds that of nucleotide-based macromolecules: whereas in peptides information lies in the number and order of aminoacids that constitute them, additional information is encoded in the structure, position, anomeric configuration and branching of glycosidic units in carbohydrates.[197–199] This highly complex 'glycocode'[200] is still largely unknown, but great effort is dedicated to its unraveling and understanding, a process that can be aided by using controlled synthetic carbohydrates.

Carbohydrate-binding proteins are called lectins, and besides recognition they can also act as receptors and transporters of sugar-containing ligands. Individual carbohydrate-lectin bonds are highly specific but reversible and generally weak; however, as is common in Nature, they are massively enhanced by multivalency:[201,202] dissociation constants of sugar-protein bonds are reduced by a factor of $10^3 – 10^6$ when multiple ('multivalent') binding is possible.[197,203,204] Glycopolymers – polymers bearing pendant glycosidic units or terminally functionalized with polysaccharides – show amplification effects in their interactions with lectines, thanks to their multiple binding sites. Glycopolymers with a higher degree of polymerization have improved binding abilities compared to those with lower molecular weight.[205,206] Having multiple saccharide moieties is not the only factor involved in sugar-protein interaction: the ability of the polymer chain to orient in different ways provides a conformational and entropic advantage over shorter polysaccharides. For example, glycopolymers have a larger affinity to lectins compared to monosaccharides, even when the polymer only binds to one lectin site,[207] because they can approach and interact with the protein in various binding modes. In fact, more flexible glycopolymer backbones or linkers lead to improved lectin affinities,[202] whereas a rigid polymer structure does not.[208]

Most cancer treatment strategies carry with them painful and, in some cases, life threatening collateral effects, due to the indiscriminate administration of toxic drugs or radiation to healthy and diseased cells alike. The selectivity of saccharide-lectin interaction

has the potential to grant targeted delivery of therapeutic or diagnostic agents. Thanks to extensive investigation of glycopolymer-lectin specific interactions, it is now known that lectin Concanavalin A (ConA) specifically interacts with glucosyl and mannosyl residues, whereas RCA_{120} (*Ricinus communis* Agglutinin 120) selectively binds to galactosyl residues.[209] Cancerous cells could be targeted by exploiting overexpressed saccharide-recognizing proteins: fructose transporter GLUT5 was found to be overexpressed by triple-negative breast cancer cells relatively to healthy cells,[210] while galactose receptor galectin-3 is involved in melanoma cancer cells evolution and metastasis.[211]

Encapsulation of chemotherapeutic drugs into glycopolymer-functionalized nanoparticles is therefore a promising strategy for selective drug delivery. RAFT polymerization proves again to be a powerful tool for the controlled synthesis of glycopolymers and glycopolymer-based amphiphilic block copolymers. Protected glucose, fructose, and galactose monomers were successfully polymerized and chain extended with hydrophobic monomers such as methyl methacrylate, butyl acrylate and butyl methacrylate[212–216] thermoresponsive N-isopropylacrylamide,[22] and light-responsive azobenzene containing monomers.[217] Biodegradable hydrophobic blocks such as poly(ε-caprolactone) can also be incorporated by preparing suitable PCL macroCTAs.[29]

Non-protected (‘free’) sugars have also been polymerized by RAFT in water or water-alcohol mixtures,[218,219] and, interestingly, glycopolymer blocks have been investigated as stabilizers for miniemulsion polymerization[220,221] and polymerization-induced self-assembly of amphiphilic block copolymers.[42]

In this Chapter, the fabrication of glycopolymer-based soft-core nanoparticles by polymerization-induced self-assembly of poly(acryloyl glucosamine)-*b*-poly(*n*-butylacrylate) is described. The final goal of the project was to develop a largely one-pot procedure for the sequential synthesis and self-assembly of nanocarriers for fluorescent up-converting dyes for bioimaging applications, whose efficiency is enhanced in fluid environments.[222]

This project was carried out at the Centre for Advanced Macromolecular Design (CAMD) at University of New South Wales in Sydney, Australia under the supervision of prof. Martina Stenzel.

7.2 Experimental

7.2.1 Materials

(D)-Glucosamine hydrochloride salt (GA.HCl), anhydrous K_2CO_3, 4,4'-Azobis(4-cyanopentanoic acid) (ACPA), acryloyl chloride, HPLC-grade methanol, dichloromethane (DCM), ethyl acetate (EtOAc), ethanol were used as received. *n*-Butylacrylate (BA) (Sigma Aldrich) was passed through activate alumina before use to remove the inhibitor. BTPA was synthesized as described elsewhere[223], and recrystallized from warm hexane before use.

7.2.2 Acryloyl glucosamine synthesis

In a typical synthesis,7 g (32.6 mmol) of GA.HCl and 6.762 g (50.0 mmol) of K_2CO_3 were stirred in 150 mL of methanol for at least an hour at room temperature in a round bottomed-flask. After complete solubilization occurred, the flask was put in an ice bath, and acryloyl chloride (4 mL, 4.456 g, 49.2 mmol) was added dropwise under vigorous agitation. A white solid started forming almost immediately. The solution was allowed to react at 0 °C for two hours, then removed from the ice bath and left stirring overnight. After this time, the white solid was filtered away, and the solution was concentrated by rotary evaporation and slowly added into excess cold DCM. The faintly yellow powder, containing AGA and K_2CO_3, was filtered and dried. Thin layer chromatography (TLC) was used to find the suitable eluent composition for column purification (EtOAc:MeOH:H_2O = 5:1:0.1), by using permanganate and methanolic sulfuric acid staining methods. The raw product was dried loaded onto a short and wide silica gel-packed column and purified by chromatography. Solvents were removed by rotary evaporation, and purified AGA was obtained with a 20 – 25% yield. AGA was characterized by ^{1}H and ^{13}C-NMR in D_2O and DMSO using either a Bruker Avance III 300, 5 mm BBFO probe (300.17 MHz, 1H: 300.17 MHz, ^{13}C: 75.48) or an Avance III 400, 5 mm BBFO probe (400.13 MHz, 1H: 400.13 MHz, ^{13}C: 100.62).

7.2.3 Poly(acryloyl glucosamine) synthesis by RAFT polymerization

In a typical synthesis, AGA (821 mg, 3.52 mmol), BTPA (32 mg, 0.134 mmol) and ACPA (7.6 mg, 0.027 mmol) were added to Schlenk flask and dissolved in 2.750 mL of MeOH/H_2O 1:1 V/V mixture. The flask was sealed with a rubber septum, and the polymerization solution was degassed by 5 freeze-pump-thaw cycles. After backfilling with dry N2 or Ar, the flask was put in an oil bath at 65 °C and allowed to react for 4 hours. After quenching by immersion in an ice bath and exposure to air, the solution was transferred in a dialysis bag (MWCO = 1000 Da) and dialyzed against a great excess of MQ water to remove unreacted monomer and ACPA. Finally, the polymer was dried by lyophilization. PAGA samples were

characterized by GPC in DMAc. AGA monomer conversion was calculated from ^{1}H-NMR spectra of raw solutions, prior to purification. SEC was carried out using a Shimandzu modular system containing a DGU-12A degasser, a LC-10AT pump, a SIL-10AD automatic injector, a CTO-10A column oven, and a RID-10A differential refractive index detector. A PL 5.0 micrometre beadsize guard column (50 x 7.5 mm2) followed by four 300 × 7.8 mm linear PL (Styragel) columns (105 , 104 , 103 and 500 Å pore size) were used for the analyses. N,N-dimethylacetamide [DMAC, HPLC grade; 0.03% w/v LiBr, 0.05% 2,6-dibutyl-4-methylphenol (BHT)] with a flow rate of 1 mL.min^{-1} was used as the mobile phase with an injection volume of 50 μL at 50 °C. Dry samples were dissolved in DMAc at a concentration of 2 - 3 mg/mL, and left stirring overnight at about 40 °C. The solutions were then filtered through PTFE filters with 450 um pore size. The unit calibration was conducted over commercially available narrow molecular weight distribution PMMA standards.

7.2.4 Poly(acryloyl glucosamine)-*b*-poly(*n*-butylacrylate) synthesis by PISA

Synthetic parameters are described in detail in the main text. As an example, PAGA50 macroCTA (40.7 mg, 0.0034 mmol), BA (72 uL, 64 mg, 0.050 mmol) and ACPA (0.19 mg, $6.7 \cdot 10^{-4}$ mmol) were added in a glass tube and dissolved in 662 μL of MeOH/H_2O 62:38 V/V mix. The tube was sealed with a rubber septum and degassed by bubbling dry Ar or N2 with a needle at 0 °C for > 30 minutes. The tube was immersed in an oil bath at 65 °C and allowed to react for 19 h to ensure total monomer conversion. After quenching by quickly immersing the tube in ice and exposing to air, aliquots were taken for conversion calculation by NMR in DMSO and molecular weight distribution measurement by GPC in DMAc. A small aliquot was withdrawn and diluted in MeOH/H_2O 62:38 V/V solution for DLS analysis using a Malvern Zetasier Nano ZS instrument equipped with a 4 mV He – Ne laser operating at λ = 632 nm and non-invasive backscatter detection at 173°. The dispersion was then transferred in a dialysis bag and dialyzed against MQ water for 24 hours (3 water changes, water in a 100-excess). Size distribution analysis by DLS was then repeated.

7.2.5 Polymer and nanoparticle characterization

7.3 Results and discussion

7.3.1 Acryloyl glucosamine (AGA) synthesis and characterization

As the glycopolymer block was going to act as a stabilizer of the growing hydrophobic block, high solubility in water/methanol mixtures was necessary. By virtue of their multiple exposed –OH functionalities, free sugars are readily soluble in water, and

soluble in methanol although a greater dilution is required. A common strategy to selectively functionalize a sugar with a RAFT-polymerizable moiety involves protection of most hydroxyl groups on the ring either by acetylation or isopropylidation, reaction with an acrylate, methacrylate or vinyl group-bearing molecule, and deprotection of the sugar. Deprotection steps, though, generally involve strong acids (TFA) or bases (NaOMe), that may cleave both the linkage (usually an ester) between sugar and double-bond, impeding chain growth, and the CTA's di- or trithiocarbonyl center, preventing further chain extension. For these reasons, a synthetic route that involved no protection/deprotection steps was chosen (**Scheme 7.1**).

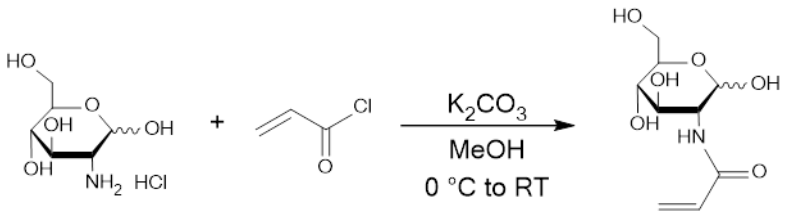

Scheme 7.1 – Reaction scheme for the formation of acryloyl glucosamine (AGA) monomers.

In a typical synthesis, a solution of glucosamine hydrochloride (GA.HCl) in HPLC-grade methanol was left stirring with 1.5 eq of K_2CO_3 for at least one hour at room temperature in a round bottom flask, in order to desalt the protected amine group. Temperature was then lowered to 0 °C, and 1.5 eq of acryloyl chloride was added dropwise to the solution via a syringe through a rubber septum. After two hours, the solution was allowed to react at room temperature overnight. After 18 - 24 hours, the solution was milky, and a white solid precipitated when stirring was interrupted. The precipitated salts were filtered off, and DCM (approx. 3 times the volume of methanol) is added to the methanol solution to induce precipitation of the monomer and K_2CO_3 and removal of excess acryloyl chloride or acrylic acid.

An estimated 50% of the white powder obtained is K_2CO_3, a base that can break the trithiocarbonyl group of the CTA, preventing controlled polymerization. Selectively removing it, though, can be tricky, since the salt and the AGA have very similar solubilities in water, methanol, and other organic solvents, making liquid-liquid separation or precipitation not feasible. Moreover, the added acrylic functionality impede glucosamine crystallization. An alternative is to induce precipitation of the salt in very polar organic solvents, that can otherwise dissolve the monomer very well, but these solvents (DMF, DMAc, or DMSO) are non-volatile and their removal is challenging.

Therefore, we opted for filtration on silica. Due to AGA's remarkable polarity, eluent mixtures that are strongly polar themselves were required: an eluent mixture of EtOAc:MeOH:H_2O 5:1:0.1 proved to be effective, but also caused contamination of the product with silica. While silica nanoparticles do not hamper polymerization, they cause incorrect weighting of AGA. So the dried compound was dissolved again in the smallest amount of methanol, and filtered through a 450 um PES syringe filter, several times if necessary. The solution pH was monitored by pH strip until it changed from acidic (pH ~ 5) to neutral (pH = 7).

Several reactions were carried out in order to find the optimal reaction conditions. In particular, the aim was to achieve complete consumption of GA, since the free amine group may harm the CTA's trithiocarbonate group. Reaction conditions of selected reactions are listed in Table 7.1. With an excess of acrylating agent of 1.3, no starting material signals were visible in the product NMR spectra (see **Figure 7.1** and following discussion). Despite complete GA reaction and the absence of any secondary products, the overall reaction yield was ultimately determined by the purification steps, especially by column chromatography, and therefore never exceeded 15% - 25%. Substituting K_2CO_3 with triethylamine (TEA) as a desalting agent that would have been easier to remove lead to unsatisfactory results.

Table 7.1 - Reaction conditions of selected AGA syntheses.

Label	GA.HCl (eq)	K_2CO_3 (eq)	AcryloylCl (eq)	[GA.HCl] (M)	GA.HCl peaks?
AGA_01	1	1.5	1.5	0.124	N
AGA_02	1	1.1	1.1	0.093	Y
AGA_03	1	1.1	1.1	0.064	Y
AGA_07	2	1.3	1.3	0.324	Y
AGA_11	1	1.5	1.3	0.093	N

The obtained compound was characterized by 1D ^{1}H-NMR and HSQC. Figure 7.1 shows a comparison of ^{1}H-NMR spectra of as-is GA.HCl, desalted GA.HCl, and AGA. Desalted GA.HCl (GA) was prepared by vigorously stirring ~20 mg of GA.HCl and ~25 mg K_2CO_3 in 650 µl of D_2O for around 30 minutes at RT. Protons attached to hydroxyl groups are not discernible in D_2O spectra, because they rapidly exchange with each other and with D_2O's residual protons, so their signals lie underneath a broad peak at 4.70 ppm. Peak assignment and integrals of all the other protons are listed in Table 7.2.

Upon deprotection of the amine group with a base, a shift in resonance frequency of protons attached to C1 and and C2 (colored green and orange in Figure 7.1, respectively) is

apparent. Some rearrangement of the signals in the 3.93 – 3.33 ppm range is also visible but less useful for monomer characterization because of overlapping.

After reaction with acryloyl chloride, C2 protons signal shift again to higher chemical shifts, while C1 proton signals remain mostly unchanged (there's a small shift probably due to the presence of some leftover methanol). Peaks generated by protons attached to the double bond (20 and 19) are also present. The disappearance of 8α and 8β peaks both in 1D ^{1}H-NMR and HSQC spectra (Figure 7.4) shows total consumption of GA.

Since an excess of acryloyl chloride was used, it was necessary to verify that reaction had only occurred on one site, the amine. ^{1}H-NMR spectra were also acquired in deuterated DMSO, where proton exchange is considerably slower, and hydroxyl protons are able to generate well defined signals. Figure 7.2 shows that all –OH groups are preserved in AGA, and that only one proton is bound to nitrogen, consistently with the formation of a secondary amide.

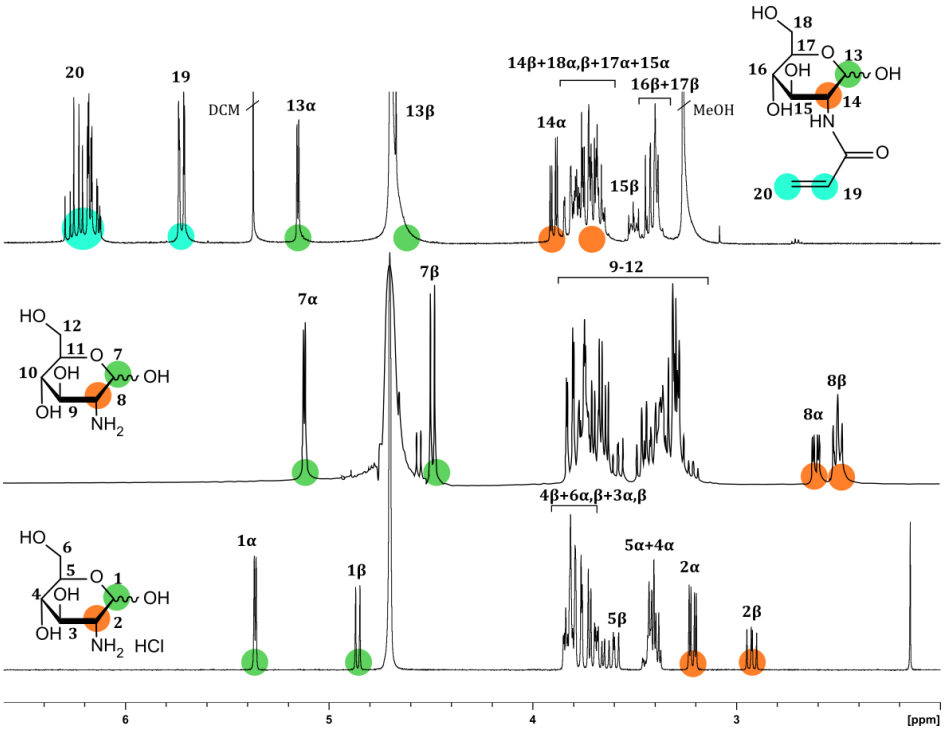

Figure 7.1 - D_2O NMR spectra of glucosamine hydrochloride (bottom), glucosamine (middle) and AGA (top). Assignments and integrals are listed in Table 7.2.

Table 7.2 - Peak assignment and integrals of NMR spectra reported in **Figure 7.1**. (R) = reference for integration.

GA.HCl

Chemical shift (ppm)	Assignment	Integral (a.u.)
5.36	1α	1.2255 (R)
4.86	1β	0.7502 (R)
3.88 – 3.64	4b+6a,b+3a,b	6.8440
3.64 – 3.56	5b	0.7756
3.50 – 3.34	5a+4a	2.8262
3.26 – 3.17	2a	1.3905
2.97 – 2.89	2b	0.6862

AGA

Chemical shift (ppm)	Assignment	Integral (a.u.)
6.32 – 6.08	20	3.8947
5.73	19	2.000 (R)
5.16	13α	1.1835
4.67	13β	Not measurable
3.94 – 3.87	14α	1.1450
3.87 – 3.596	14β +15α +17α +18α,β	7.6100
3.57 – 3.34	15β+16β +17β	3.8570

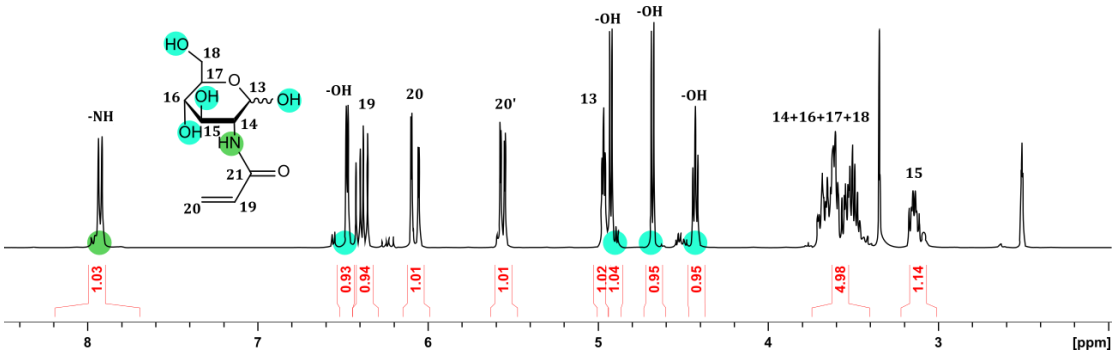

Figure 7.2 – ^{1}H-NMR spectrum of AGA in DMSO-d_6.

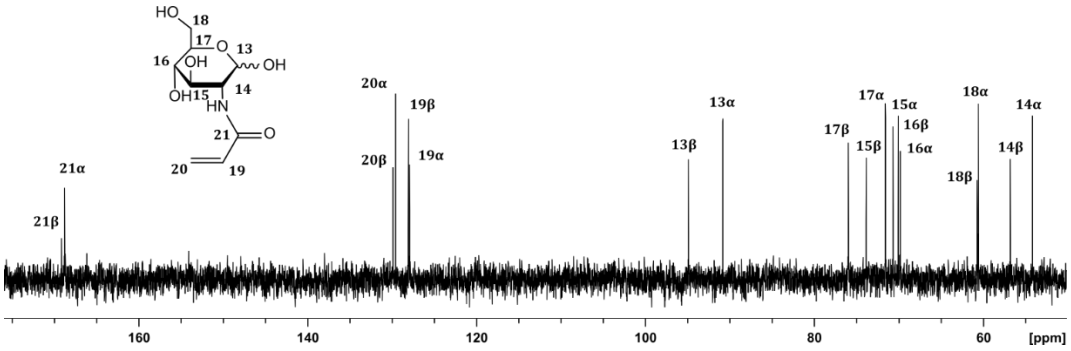

Figure 7.3 - ^{13}C-NMR of AGA in D_2O.

Table 7.3 - List of chemical shifts and assignments of AGA ^{13}C-NMR peaks.

Chemical shift (ppm)	Assignment	Chemical shift (ppm)	Assignment
169.1	21β	73.8	15β
168.8	21α	71.6	17α
129.9	20β	70.7	15α
129.6	20α	70.0	16β
128.0	19β	69.8	16α
127.9	19α	60.7	18β
94.9	13β	60.6	18α
90.8	13α	56.8	14β
75.7	17β	54.1	14α

High AGA purity was also proven by ^{13}C-NMR spectra in D_2O, showing only signals generated by the two anomeric forms of AGA (**Figure 7.3**).

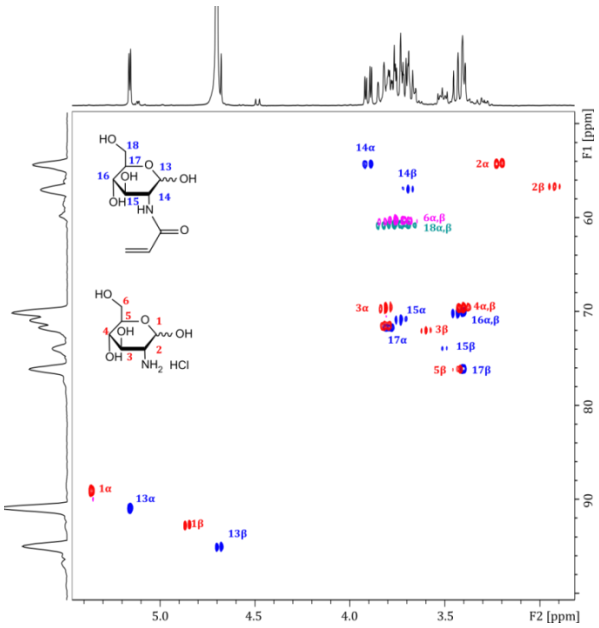

Figure 7.4 – HSQC spectra of GA.HCl (red/pink) and AGA (blue/cyan).

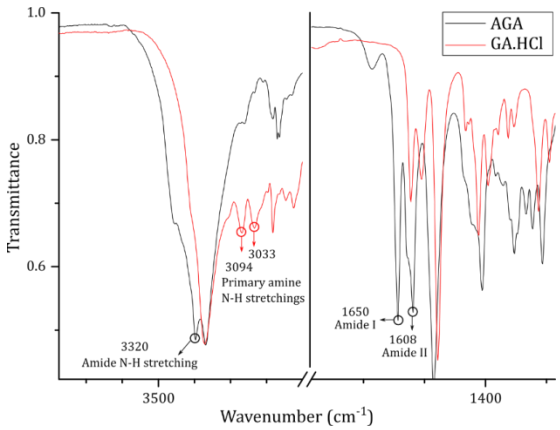

Figure 7.5 – FT-IR spectra of GA.HCl (red) and AGA (black) in powder form. Relevant peaks are highlighted and assigned.

Since a free amine could interfere with polymerization by degrading the trithiocarbonyl group of the CTA, particular care was employed in making sure no unreacted GA was contaminating AGA. IR spectra of AGA and GA.HCl were compared (Figure 7.5). Amine and amide N-H stretching peaks are generally found in the 3500 – 3300 cm^{-1} and 3700 – 3500 cm^{-1} range, respectively. Molecules with very high hydrogen bonding capabilities, though, may show a shift in vibrational frequencies to lower wavenumbers, especially when analysed not in dilute solution. IR spectra clearly show the disappearance of primary amine stretching modes and the emergence of amide stretching and bending characteristic peaks.

7.3.2 PAGA block synthesis and characterization

In the perspective of developing a one-pot process comprising the sequential synthesis of both blocks with minimal changes to the reactor environment, suitable synthetic conditions where all reactants are solubilized are needed. BTPA CTA shows good solubility in methanol, but sparse solubility in water. The behaviour of AGA is the opposite. Several solubility tests were carried out to find the right methanol/water mixture that ensured complete dissolution of BTPA and AGA at the desired concentrations. We settled on MeOH:H_2O 50:50 V:V composition: while at room temperature the mixture is very viscous and milky white (due to undissolved AGA), it turns completely clear and yellow (due to BTPA) at 65 °C after less than 5 seconds. Temperature has a particularly strong influence on solubilisation of unprotected sugars, due to great number of hydrogen bonds they can form with solvent molecules. Methanol soluble ACPA was used as initiator. Polymerization solutions were effectively degassed by N_2 bubbling for at least 30 minutes, at 0 °C to prevent methanol evaporation. A very high monomer conversion was targeted in order to render purification of the first block unnecessary before the chain extension step, and achieve a full one-pot procedure (**Scheme 7.2**).

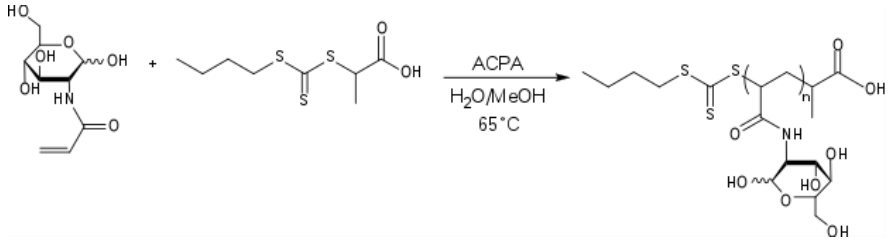

Scheme 7.2 – RAFT polymerization of AGA.

Polymerization conditions and product characterization for selected reactions are listed in Table 7.4. Conversion was calculated by ^{1}H NMR, by comparing the integrals of vinyl peaks at time zero and at the end of the reaction. The number of AGA repeating units was calculated by n_{PAGA} = (M/T)×(Conversion), and number-average molecular weight $\bar{M}_n^{NMR}$ was calculated by $\bar{M}_n^{NMR} = n_{PAGA} \cdot mw_{AGA} + mw_{BTPA}$, where $\mathrm{mw_{AGA}}$ and $\mathrm{mw_{BTPA}}$ are the molecular weights of AGA and BTPA, respectively.

Table 7.4 - Polymerization conditions and product characterization for selected reactions. $\mathrm{n_{PAGA}}^{\mathrm{NMR}}$ is calculated comparing the integrals of PAGA backbone protons and that of CTA's $-CH_3$ end group. $\mathrm{M_n}^{\mathrm{NMR}}$ is calculated from conversion. $\mathrm{M_w}^{\mathrm{GPC}}$ and PDI are calculated by SEC in DMAc, using PMMA standards as calibration.

Label	M/T	T/I	$[AGA]_0$ (M)	T (°C)	Time	Conv	n_{PAGA}	$\mathrm{n_{PAGA}}^{\mathrm{NMR}}$	$\mathrm{M_n}^{\mathrm{NMR}}$	$\mathrm{M_w}^{\mathrm{GPC}}$	PDI

					(h)	(%)			(Da)	(Da)	
PAGA_02	72	5	1.001	70	5	76	55	30	13053	19200	1.19
PAGA_05	50	5	1.005	70	5	--	--	--	--	--	
PAGA_06	50	8	1.272	70	5	--	--	--	--	--	
$PAGA_{50}$	48	5	1.016	65	5	~100	48	54	11422	21900	1.06
$PAGA_{75}$	74	5	0.742	65	5	~100	74	75	17480	29400	1.07
$PAGA_{25}$	24	4	0.967	65	3.5	~100	24	24	5830	8500	1.07

Entries 1, 2 and 3 in Table 7.4 exemplify the effect of the presence of K_2CO_3 due to imperfect purification of AGA on polymerization. In all three cases, the brightly yellow starting solution turned orange-brown after a few hours in the oil bath, symptom of BTPA trithiocarbonylthio center disruption. While in PAGA_05 and PAGA_06 no polymerization was observed in 5 hours, in PAGA_02 a conversion of 76% was reached. DP obtained by conversion (n_{PAGA}) and by comparison with CTA NMR signals (n_{PAGA}^{NMR}) (Figure 7.6(B)), did not match very well, suggesting a poor control on chain end functionalization. After proper monomer purification, the polymerizations were repeated, setting a rather low T/I and using a starting monomer concentration ≥ 0.70 M. In all cases, almost total conversion was achieved after 3.5 hours. n_{PAGA} and n_{PAGA}^{NMR} are almost identical, suggesting good control on chain end functionalization with BTPA, and PDIs are very low. Molecular weights calculated by GPC are higher than those calculated by NMR; however, these values ought to be considered as 'PMMA equivalents', and not absolute. GPC traces are shown in Figure 7.6(A).

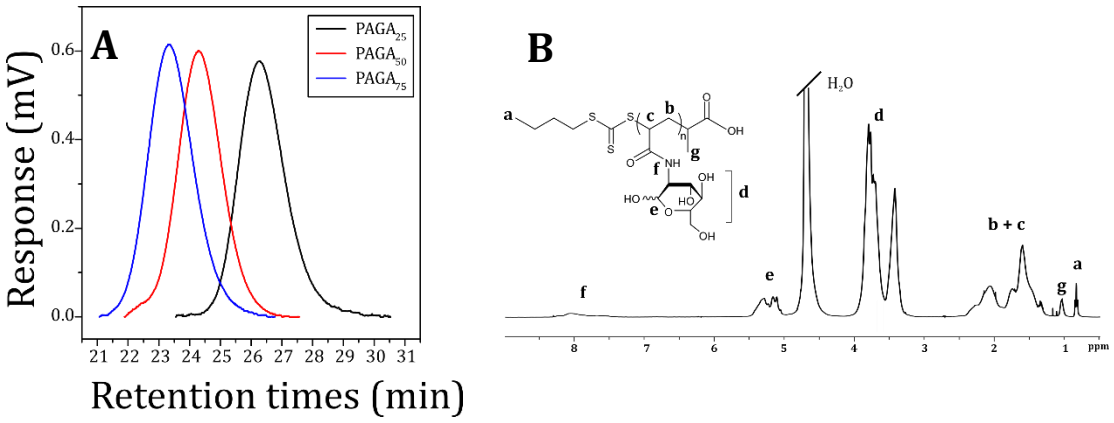

Figure 7.6 – (A) GPC traces of $PAGA_{25}$, $PAGA_{50}$ and $PAGA_{75}$ (B) D_2O ^1H NMR spectrum of $PAGA_{25}$.

7.3.3 Chain extension with BA in PISA conditions

PISA conditions require dissolution of the monomer in the solvent before polymerization starts. If the monomer is not soluble, an emulsion is formed and the polymerization will continue in emulsion conditions, yielding only spherical particles. In

order to access self-assembled morphologies driven by polymerization, no initial sphere formation due to hydrophobic monomer insolubility is desirable. PAGA macroCTAs and *n*-butylacrylate (BA) have opposite solubilities: PAGA is readily soluble in water, sparingly in methanol; BA largely insoluble in water, and soluble in methanol. Moreover, large quantities of BA can induce precipitation of PAGA by increasing the overall hydrophobicity of the solvent/monomer phase. Several solubility tests were conducted in order to find the right solvent mixture for chain extension reactions. Only very limited ranges of solids concentration and solvent compositions were found to be accessible. If the water content is too high, BA undergoes phase separation. If it's too low, PAGA crashed out when hydrophobic BA is added (using a molar ratio of 250:1 BA:$PAGA_{25}$). An additional level of complexity is added by the molecular-weight dependent solubility of PAGA: PAGA75 was found to be only partially soluble in the desired conditions, and was therefore discarded as a stabilizing block. We chose to use 62:38 V/V MeOH/H_2O solutions as a solvent mixture, and a solid concentration (i.e. total copolymer weight concentration after complete conversion) of 15%. In these conditions, BA is phase separated at room temperature but is dissolved at 65 °C. The initially turbid dispersion turns completely clear and yellowish within 5 seconds in the oil bath.

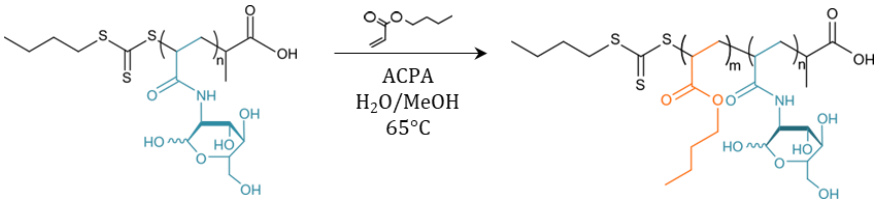

Scheme 7.3 – PISA of PAGA-*b*-PBA.

Polymerizations were carried out in sealed glass tubes, after bubbling with nitrogen, at 65 °C. Since stirring rate is known to influence self-assembly, a fixed rate of 400 rpm was maintained using a stir plate. Complete conversion was targeted, in order to obtain so-called *post-mortem* morphologies: that is, objects whose morphology depends mainly on the hydrophilic/hydrophobic balance of the block copolymer. After 20 to 24 hours, polymerizations were stopped by quenching in iced water and exposing to air (Scheme 7.3).

A summary of polymerizations can be found in Table 7.5. Monomer conversion was calculated by comparing the integrals of the vinyl peaks of BA and the protons of polymerized BA (Figure 7.7). The fraction of hydrophilic block f_{PAGA} was calculated from the

number AGA and BA units as: $f_{PAGA} = n_{PAGA}/(n_{PAGA} + \frac{M}{T} Conv)$, and as such is not a volumic fraction.

Table 7.5 – PAGA extension with PBA polymerization parameters and monomer conversions. $Conv = (I_{1+a} - 3I_6)/I_{1+a} \cdot 100$.

Label	M_n PAGA (Da)	M/T	T/I	t (h)	Conv. (%)	f_{PAGA}
$PAGA_{50}$-*b*-PBA_{50}	11420	50	4	3.5	94	0.52
$PAGA_{50}$-*b*-PBA_{100}	11420	101	5	24	92	0.35
$PAGA_{50}$-*b*-PBA_{150}	11420	148	5	24	91	0.27
$PAGA_{50}$-*b*-PBA_{175}	11420	181	5	24	97	0.22
$PAGA_{50}$-*b*-PBA_{275}	11420	264	5	24	99	0.16
$PAGA_{50}$-*b*-PBA_{500}	11420	523	5	24	91	0.09
$PAGA_{25}$-*b*-PBA_{50}	5830	49	5	24	99	0.36
$PAGA_{25}$-*b*-PBA_{75}	5830	77	5	24	99	0.25
$PAGA_{25}$-*b*-PBA_{100}	5830	100	5	24	99	0.20
$PAGA_{25}$-*b*-PBA_{175}	5830	186	5	24	99	0.13
$PAGA_{25}$-*b*-PBA_{250}	5830	258	5	24	99	0.09

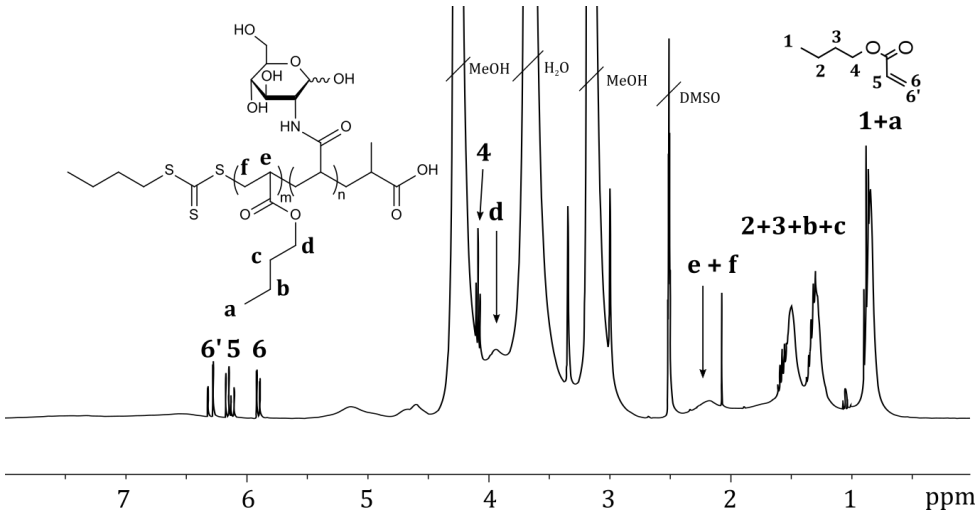

Figure 7.7 – ^{1}H NMR spectrum of $PAGA_{50}$-b-PBA_{100} crude solution in DMSO-d6.

Gel permeation chromatography of copolymers was problematic because of the two constituting blocks' opposed polarity that rendered sample dissolution in a common solvent very difficult. In fact, DMAc is not a good solvent for PBA. No signal was visible for copolymer concentrations up to 2.5 mg/mL in DMAc (either from crude solutions or dried products). A peak was visible only at relatively high concentration of 3.0 – 3.2 mg/mL, but still not very intense. It is likely that a great portion of copolymer sample was lost during filtration through 450 um-pore filters. GPC curves of copolymers obtained after dialysis

against MQ water are shown in Figure 7.8; samples with higher PBA contents showed no peak in the chromatogram. Their intensity was normalized to aid comparison, but it should be kept in mind that, for example, the intensity of the curve of $PAGA_{25}$-*b*-PBA_{250} (Figure 7.8(A), red line) was 1/10 of that generated by $PAGA_{25}$ (Figure 7.8(A), black line), as also indicated by its much lower signal-to-noise ratio. PDI determination could be therefore imprecise.

While a shift to higher molecular weights is present, peaks are non-symmetrical and PDIs increase with increasing monomer-to-macroCTA ratios, indicating a very poor control on polymerization. Possible causes are:

- unsuitable macroCTA: chain extension by RAFT may be poorly controlled when the stability of the radical is lower on the monomer than on the macroCTA forming block. Although reactivities of acrylamides and acrylates are close enough to be generally categorized in the same class,[224] acrylamide macroCTA may not be able to control chain extension with acrylates;
- poor end group control on the PAGA block, due to termination reactions occurring at high AGA conversions;
- inaccessibility of CTA during polymerization in PISA conditions.

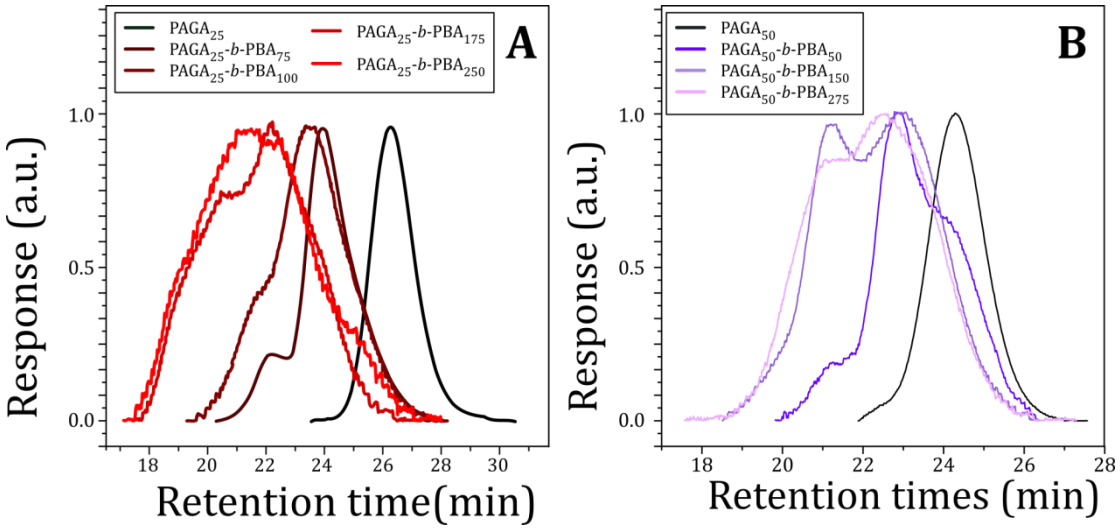

Figure 7.8 – Normalized GPC curves of (A) $PAGA_{25}$-*b*-PBA_x and (B) $PAGA_{50}$-*b*-PBA_x copolymers in DMAc.

7.3.4 Nanoparticles characterization

Each obtained dispersion was analysed by DLS. Size intensity distributions are shown in **Figure 7.9**(A–B), and nanoparticle size and PDI values are listed in Table 7.6. Since the

native dispersion concentration exceeded the concentration range within size distribution determination by DLS is precise, dispersions were diluted until see-through and the automatic measurement optimization selected a focus position near the center of the cuvette with a medium attenuation (5 or 6) – generally 1:10 to 1:100 V/V. In all cases, single populations were obtained. PDI generally increased after dialysis. At the same number of BA units, PAGA25-based copolymers yielded larger particles than $PAGA_{50}$-based counterparts (Figure).

Selected TEM images of dispersions negatively stained with uranyl acetate are shown in Figure 7.10 and Figure 7.11 for $PAGA_{50}$-*b*-PBA_x and $PAGA_{25}$-*b*-PBA_x, respectively. All observed particles are spherical, though some shape deformation is visible, possibly due to characterization being out in vacuum conditions after drying TEM grids at 30 °C overnight. A tendency to aggregation is clear in all images; nevertheless, very little particle fusion was present, especially in $PAGA_{50}$-containing samples: despite little repulsion exists between PAGA coronas, it was sufficient to prevent coalescence.

The spherical shape of the obtained nanoparticles and their size increase with a decrease of stabilizer molecular weight suggest that the polymerization proceeded in emulsion rather than dispersion conditions. In order to access other morphological classes (worms, vesicles), better solvent conditions for monomer and stabilizer need to be found. Since modulation of solvent composition proved to be limited, a less hydrophilic glycomonomer or a more hydrophilic core-forming monomer need to be selected. A good strategy would the insertion of an acrylate – instead of acrylamide – moiety on glucosamine, for example by reacting it with the acyl chloride of 2-carboxyethyl acrylate: this would have the double effect of increasing hydrophobicity and allowing a better control over chain extension with butyl acrylate.

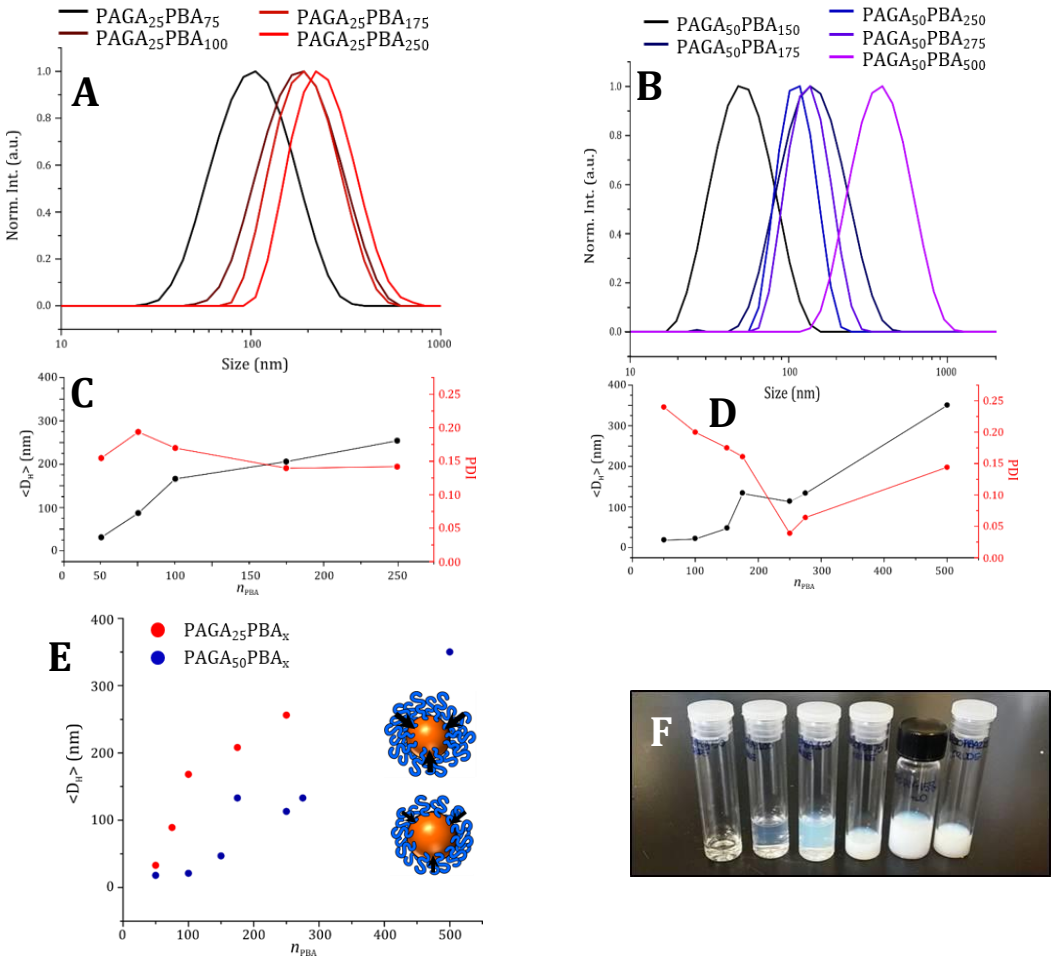

Figure 7.9 – DLS intensity distributions, average hydrodynamic diameters $<D_H>$ and PDI value of (A,C) PAGA$_{25}$-*b*-PBA$_x$ and (B,D) PAGA$_{50}$-*b*-PBA$_x$ after dialysis. (E) Comparison of nanoparticle size as a function of PBA content for PAGA$_{25}$ and PAGA$_{50}$-containing systems. (F) Physical appearance PAGA$_{50}$-*b*-PBA$_x$ dispersions. n_{PBA} increases from left to right.

Table 7.6 - Hydrodynamic diameters of particles dispersed in 38:62 V/V H_2O:MeOH (WM subscript) and in water after dialysis (W subscript).

Label	**$<D_H>_{WM}$(nm)**	**PDI_{WM}**	**$<D_H>_W$ (nm)**	**PDI_W**
PAGA$_{50}$-*b*-PBA$_{50}$	25	0.240		
PAGA$_{50}$-*b*-PBA$_{100}$	30	0.200	Polydisperse	Polydisperse
PAGA$_{50}$-*b*-PBA$_{150}$	69	0.130	47	0.175
PAGA$_{50}$-*b*-PBA$_{175}$	180	0.170	133	0.161
PAGA$_{50}$-*b*-PBA$_{250}$	N.d.	N.d.	113	0.039
PAGA$_{50}$-*b*-PBA$_{275}$	201	0.040	133	0.064
PAGA$_{50}$-*b*-PBA$_{500}$	402	0.055	350	0.144
PAGA$_{25}$-*b*-PBA$_{50}$	36	0.156		

$PAGA_{25}$-*b*-PBA_{75}	122	0.138	89	0.195
$PAGA_{25}$-*b*-PBA_{100}	246	0.344	168	0.171
$PAGA_{25}$-*b*-PBA_{175}	270	0.065	208	0.141
$PAGA_{25}$-*b*-PBA_{250}	362	0.161	256	0.143

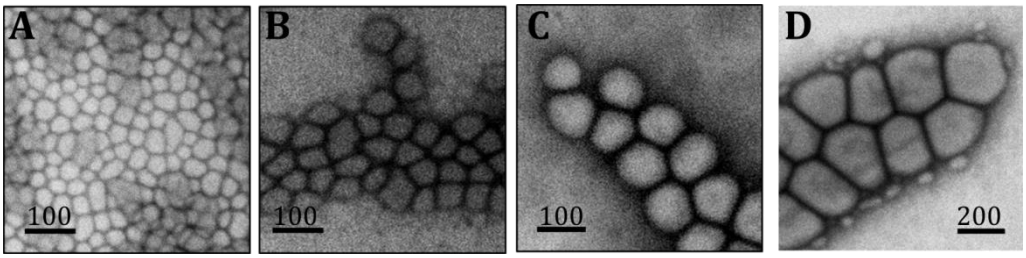

Figure 7.10 – TEM micrographs of (A) $PAGA_{50}$-*b*-PBA_{100}, (B) $PAGA_{50}$-*b*-PBA_{150}, (C) $PAGA_{50}$-*b*-PBA_{275}, (D) $PAGA_{50}$-*b*-PBA_{500} nanoparticles.

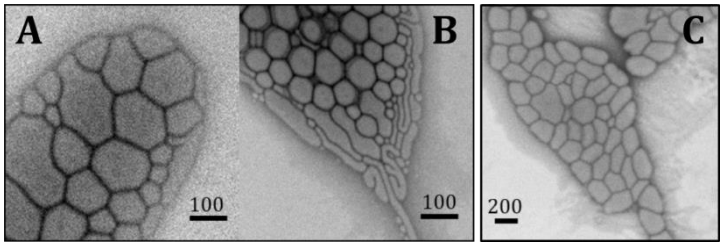

Figure 7.11 – TEM micrographs of (A–B) $PAGA_{25}$-*b*-PBA_{175}, (C) $PAGA_{25}$-*b*-PBA_{250} nanoparticles.

Although further optimization of the process is warranted, it is worth noting that the obtained latexes proved to be remarkably stable at 25 – 50 mg/mL concentrations: after storage at room temperature with no stirring for one month, DLS distributions were superimposable with freshly synthesized samples. This feature, coupled with the softness of their core, are promising bioactive carriers for up-converting molecules.

7.4 Conclusions

In this Chapter, polymerization-induced self-assembly of glycopolymer-based amphiphilic block copolymers was investigated. A facile synthetic strategy allowed to obtain acryloyl glucosamine (AGA) monomers with high purity in only one synthetic step. Three poly(AGA) samples with DP = 25, 50 and 75 were polymerized in water/methanol mixture by RAFT polymerization, with remarkable control even to very high monomer conversion (PDI = 1.07, 1.06 and 1.07 for $PAGA_{25}$, $PAGA_{50}$ and $PAGA_{75}$, respectively). Optimization of reaction conditions allowed the use of $PAGA_{25}$ and $PAGA_{50}$ as stabilizers and macroCTAs for chain-

extension with *n*-butylacrylate (BA) in methanol/water environment. BA to AGA ratios varied from 1:1 to 10:1. DLS analysis of crude and dialyzed dispersions, which proved to be stable for one month, showed single populations with PDIs always < 0.200. Particle size increased with BA:AGA monomer ratio, ranging from 25 to 402 nm. Shorter $PAGA_{25}$ stabilizing chains lead to the formation of larger particles compared to $PAGA_{50}$. In dry state, nanoparticles appeared as mainly spherical, possibly due to the softness of PBA cores allowing for chain rearrangement during polymerization, and particle fusion during TEM sample preparation and analysis. However, poor control was achieved over RAFT polymerization: PAGA-*b*-PBA GPC traces were shifted to higher molecular weights, but peaks were asymmetrical and multimodal. It is expected that using both hydrophilic and hydrophobic monomers bearing the same polymerizable moiety (acrylate or acrylamide) a better control over chain extension could be reached.

LIST OF ABBREVIATIONS

ACT: acetone;
AFM: Atomic Force Microscopy;
AIBN: 2,2'-azobis(2-methylpropionitrile);
AM: acrylamide;
AN: acrylonitrile;
AROP: anionic ring opening polymerization;
ATRP: atom transfer polymerization;
BBB: blood-brain barrier;
BTP: 3-(Benzylsulfanylthiocarbonylsulfanyl) propionic acid;
$CDCl_3$: deuterated chloroform;
CEM: Cryogenic Electron Microscopy;
CET: Cryogenic Electron Tomography;
CL: caprolactone;
CROP: Cationic Ring Opening Polymerization;
CTA: chain transfer agent;
DAAM: diacetone acrylamide;
DBU: 1,8-diazabicyclo[5.4.0]undec-7-ene;
DCM: dichloromethane;
D_{core}: core diameter;
DDAT: 2-(Dodecylcarbonylthioylthio)-2-methylpropionic acid;
DDS: drug delivery system;
D_H: hydrodynamic diameter;
DLS: dynamic light scattering;
DMA: N,N'-dimethylacrylamide;
DMAP: 4-(dimethylamino)pyridine;
DMF: dimethylformamide;
DSC: differential scannin calorimetry;
DX: 1,4-dioxane;
EtOx: 2-ethyl-2-oxazoline;
FDA: Food and Drugs Administration;
FIB: Focused Ion Beam;
HUVEC: human umbilical vein endothelial cells;
LA: lactic acid;
LRP: Living Radical Polymerization;
MA: methyl acrylate;
macroCTA: macromolecular chain transfer agent;
MADIX: macromolecular design via the interchange of xanthates;
MMA: methyl methacrylate;
$mPEO_{113}$: poly(ethylene oxide) monomethyl ether, 113 repeating units;
MPS: mononuclear phagocytic systems;
Mw: weigth-averaged molecular weight;
MWCO: molecular weight cut-off;
*n*BA: n-butyl acrylate;
NHC: N-heterocyclic carbenes;
NMP: nitroxide mediated polymerization;
NMR: nuclear magnetic resonance;
NP: nanoparticle;
P(L-LA): poly(L-lactic acid);
P4VP: poly(4-vinyl pyridine);
PB: poly(butadiene);
PCL: poly(e-caprolactone);
PDI: polydispersity index;
PDMA: poly(N,N'-dimethylacrylamide);
PEO: poly(ethylene oxide);
PEtOx: poly(2-ethyl-2-oxazoline);
PISA: polymerization induced self-assembly;
PLA: poly(lactic acid);
PLGA: poly(lactic-co-glycolic acid);
POx: poly(oxazoline)s;
PS: polystyrene;
P*t*BA: poly(tert-butyl acrylate);

Q.E.: quantum efficiency;

RAFT: Radical Addition-Fragmentation chain Transfer;

SANS: small angle neutron scattering;

SEM: Scanning Electron Microscopy;

$Sn(Oct)_2$: tin(II) 2-ethylhexanoate;

TEM: Transmission Electron Microscopy;

T_g: glass transition temperature;

THF: tetrahydrofuran;

TRPL: time-resolved photoluminescence;

TU: thiourea;

VAc: vinyl acetate;

VL: valerolactone;

REFERENCES

(1) Ferrari, M. *Nat. Rev.* **2005**, *5*, 161–171.

(2) Nicolas, J.; Guillaneuf, Y.; Lefay, C.; Bertin, D.; Gigmes, D.; Charleux, B. *Prog. Polym. Sci.* **2013**, *38* (1), 63–235.

(3) Matyjaszewski, K.; Tsarevsky, N. V. *J. Am. Chem. Soc.* **2014**, *136* (18), 6513–6533.

(4) Perrier, S.; Takolpuckdee, P. *J. Polym. Sci. Part A Polym. Chem.* **2005**, *43* (22), 5347–5393.

(5) Chiefari, J.; Chong, Y. K.; Ercole, F.; Krstina, J.; Jeffery, J.; T Le, T. P.; A Mayadunne, R. T.; Meijs, G. F.; Moad, C. L.; Moad, G.; Rizzardo, E.; Thang, S. H. *Macromolecules* **1998**, *31*, 5559–5562.

(6) Boyer, C.; Bulmus, V.; Davis, T. P.; Ladmiral, V.; Liu, J.; Perrier, S. *Chem. Rev.* **2009**, *109*, 5402–5436.

(7) Corrigan, N.; Rosli, D.; Warren, J.; Jones, J.; Xu, J.; Boyer, C. *Macromolecules* **2016**, *49* (18), 6779–6789.

(8) Lu, L.; Yang, N.; Cai, Y. *Chem. Commun.* **2005**, 5287–5288.

(9) Chong, (Bill) Y. K.; Krstina, J.; Le, T. P. T.; Moad, G.; Postma, A.; Rizzardo, E.; Thang, S. H. *Macromolecules* **2003**, *36* (7), 2256–2272.

(10) Moad, G.; Rizzardo, A. E.; Thang, S. H. *Aust. J. Chem* **2005**, *58*, 379–410.

(11) Favier, A.; Charreyre, M.-T. *Macromol. Rapid Commun.* **2006**, *27* (9), 653–692.

(12) Duncan, R. *Nat. Rev. Cancer* **2006**, *6* (9), 688–701.

(13) Albertin, L.; Stenzel, M.; Barner-Kowollik, C.; Foster, J. R.; Davis, T. P. *Macromolecules* **2004**, *37*, 7530–7537.

(14) Warren, N. J.; Mykhaylyk, O. O.; Mahmood, D.; Ryan, A. J.; Armes, S. P. *J. Am. Chem. Soc.* **2014**, *136* (3), 1023–1033.

(15) Byard, S. J.; Williams, M.; Mckenzie, B. E.; Blanazs, A.; Armes, S. P. *Macromolecules* **2017**, *50*, 1482–1493.

(16) Kopeć, M.; Krys, P.; Yuan, R.; Matyjaszewski, K. *Macromolecules* **2016**, acs.macromol.6b01336.

(17) Khine, Y. Y.; Jiang, Y.; Dag, A.; Lu, H.; Stenzel, M. H. *Macromol. Biosci.* **2015**, *15*, 1091–1104.

(18) Werz, P. D. L.; Kainz, J.; Rieger, B. *Macromolecules* **2015**, *48* (18), 6433–6439.

(19) Lovett, J. R.; Warren, N. J.; Armes, S. P.; Smallridge, M. J.; Cracknell, R. B. *Macromolecules* **2016**, *49* (3), 1016–1025.

(20) Chen, W.; Du, J. *Sci. Rep.* **2013**, *3*, 1–9.

(21) Şanal, T.; Oruç, O.; Öztürk, T.; Hazer, B. *J. Polym. Res.* **2015**, *22* (2), 3.

(22) Zhang, L.; Bernard, J.; Davis, T. P.; Barner-Kowollik, C.; Stenzel, M. H. *Macromol. Rapid Commun.* **2008**, *29* (2), 123–129.

(23) Quémener, D.; Davis, T. P.; Barner-Kowollik, C.; Stenzel, M. H. *Chem. Commun. (Camb).* **2006**, No. 48, 5051–5053.

(24) Wu, Y.; Zhou, Y.; Zhu, J.; Zhang, W.; Pan, X.; Zhang, Z.; Zhu, X. *Polym. Chem.* **2014**, *5* (19), 5546.

(25) Abdelkader, O.; Moebs-sanchez, S.; Queneau, Y.; Bernard, J.; Fleury, E.; Lyon, D. *J. Polym. Sci. Part A Polym. Chem.* **2011**, *49*, 1309–1318.

(26) Spruell, J. M.; Levy, B. A.; Sutherland, A.; Dichtel, W. R.; Cheng, J. O. Y. Y.; Stoddart, J. F.; Nelson, A. *J. Polym. Sci. Part A Polym. Chem.* **2009**, *47*, 346–356.

(27) Kulkarni, S.; Schilli, C.; Grin, B.; Mü, A. H. E.; Hoffman, A. S.; Stayton, P. S. *Biomacromolecules* **2006**, *7*, 2736–2741.

(28) Yu, Y. C.; Li, G.; Kim, J.; Youk, J. H. *Polym. (United Kingdom)* **2013**, *54* (22), 6119–6124.

(29) Ganda, S.; Dulle, M.; Drechsler, M.; Förster, B.; Förster, S.; Stenzel, M. H. *Macromolecules* **2017**, *50*, 8544–8553.

(30) Yildirima, I.; Weber, C.; Schubert, U. S. *Prog. Polym. Sci.* **2018**, *76*, 111–150.

(31) Qian, W.; Song, X.; Feng, C.; Xu, P.; Jiang, X.; Li, Y.; Huang, X. *Polym. Chem.* **2016**, *7*, 3300–3310.

(32) Krieg, A.; Weber, C.; Hoogenboom, R.; Remzi Becer, C.; Schubert, U. S. *ACS Macro Lett.* **2012**, *1*, 776–779.

(33) Huynh, V. T.; Binauld, S.; De Souza, P. L.; Stenzel, M. H. *Chem. Mater.* **2012**, *24*, 3197–3211.

(34) Gregori, M.; Bertani, D.; Cazzaniga, E.; Orlando, A.; Mauri, M.; Bianchi, A.; Re, F.; Sesana, S.; Minniti, S.; Francolini, M.; Cagnotto, A.; Salmona, M.; Nardo, L.; Salerno, D.; Mantegazza, F.; Masserini, M.; Simonutti, R. *Macromol. Biosci.* **2015**, *15*, 1687–1697.

(35) Zhang, W.-J.; Hong, C.-Y.; Pan, C.-Y. *Biomacromolecules* **2017**, *18* (4), 1210–1217.

(36) Hu, J.; Qiao, A. R.; Whittaker, M. R.; Quinn, J. F.; Davis, T. P. *Aust. J. Chem.* **2017**, *70*, 1161–1170.

(37) Zhang, W.; D'Agosto, F.; Dugas, P. Y.; Rieger, J.; Charleux, B. *Polym. (United Kingdom)* **2013**, *54* (8), 2011–2019.

(38) Rieger, J.; Osterwinter, G.; Bui, C.; Stoffelbach, F.; Charleux, B. *Macromolecules*

2009, *42* (15), 5518–5525.

(39) Zhang, X.; Boisson, F.; Colombani, O.; Chassenieux, C.; Charleux, B. *Macromolecules* **2014**, *47* (1), 51–60.

(40) Hatton, F. L.; Ruda, M.; Lansalot, M.; D 'agosto, F.; Malmströ, E.; Carlmark, A. *Biomacromolecules* **2016**, *17*, 1414–1424.

(41) Ladmiral, V.; Semsarilar, M.; Canton, I.; Armes, S. P. *J. Am. Chem. Soc.* **2013**, *135* (36), 13574–13581.

(42) Ladmiral, V.; Semsarilar, M.; Canton, I.; Armes, S. P. *J. Am. Chem. Soc.* **2013**, No. 135, 13574–13581.

(43) Ratcliffe, L. P. D.; Blanazs, A.; Williams, C. N.; Brown, S. L.; Armes, S. P. *Polym. Chem.* **2014**, No. 5, 3643–3655.

(44) Warren, N. J.; Armes, S. P. *J. Am. Chem. Soc.* **2014**, *136*, 10174–10185.

(45) Zhou, D.; Dong, S.; Kuchel, R. P.; Perrier, S.; Zetterlund, P. B. *Polym. Chem.* **2017**, *8*, 3082.

(46) Jones, E. R.; Mykhaylyk, O. O.; Semsarilar, M.; Boerakker, M.; Wyman, P.; Armes, S. P. *Macromolecules* **2016**, *49* (1), 172–181.

(47) Jones, E. R.; Semsarilar, M.; Blanazs, A.; Armes, S. P. *Macromolecules* **2012**, *45*, 5091.

(48) Jones, E. R.; Semsarilar, M.; Wyman, P.; Boerakker, M.; Armes, S. P. *Polym. Chem.* **2016**, *7*, 851–859.

(49) Karagoz, B.; Boyer, C.; Davis, T. P. *Macromol. Rapid Commun.* **2014**, *35* (4), 417–421.

(50) Yeow, J.; Shanmugam, S.; Corrigan, N.; Kuchel, R. P.; Xu, J.; Boyer, C. *Macromolecules* **2016**, *49*, 7277.

(51) Tan, J.; Sun, H.; Yu, M.; Sumerlin, B. S.; Zhang, L.; Butler, J. *ACS Macro Lett.* **2015**, *4*, 1249.

(52) Dechy-Cabaret, O.; Martin-Vaca, B.; Bourissou, D. *Chem. Rev.* **2004**, *104*, 6147–6176.

(53) Kamber, N. E.; Jeong, W.; Waymouth, R. M.; Pratt, R. C.; Lohmeijer, B. G. G.; Hedrick, J. L. *Chem. Rev.* **2007**, *107*, 5813–5840.

(54) Alba, A.; Thillaye Du Boullay, O.; Martin-Vaca, B.; Bourissou, D. *Polym. Chem.* **2015**, *6*.

(55) Thomas, C.; Bibal, B. *Green Chem.* **2014**, *16* (4), 1687–1699.

(56) Pratt, R. C.; Lohmeijer, B. G. G.; Long, D. A.; Lundberg, P. N. P.; Dove, A. P.; Li, H.; Wade, C. G.; Waymouth, R. M.; Hedrick, J. L. *Macromolecules* **2006**, *39* (23), 7863–

7871.

(57) Spink, S. S.; Kazakov, O. I.; Kiesewetter, E. T.; Kiesewetter, M. K. *Macromolecules* **2015**, *48* (17), 6127–6131.

(58) Thomas, C.; Peruch, F.; Bibal, B. *RSC Adv.* **2012**, *2*, 12851–12856.

(59) Coady, D. J.; Fukushima, K.; Horn, H. W.; Rice, J. E.; Hedrick, J. L. *Chem. Commun.* **2011**, *47* (47), 3105–3107.

(60) Sherck, N. J.; Kim, H. C.; Won, Y. Y. *Macromolecules* **2016**, *49* (13), 4699–4713.

(61) Hrkach, J. S.; Matyjaszewski, K. *Macromolecules* **1992**, *25*, 2070–2075.

(62) Guillerm, B.; Darcos, V.; Lapinte, V.; Monge, S.; Coudane, J.; Robin, J.-J. *Chem. Commun.* **2012**, *48*, 2879–2881.

(63) Becer, C. R.; Paulus, R. M.; Höppener, S.; Hoogenboom, R.; Fustin, C.-A.; Gohy, J.-F.; Schubert, U. S. *Macromolecules* **2008**, *41* (14), 5210–5215.

(64) Kowalczuk, A.; Kronek, J.; Bosowska, K.; Trzebicka, B.; Dworak, A. *Polym. Int.* **2011**, *60* (7), 1001–1009.

(65) Hoogenboom, R.; Leenen, M. A. M.; Wiesbrock, F.; Schubert, U. S. *Macromol. Rapid Commun.* **2005**, *26* (22), 1773–1778.

(66) Trzebicka, B.; Koseva, N.; Mitova, V.; Dworak, A. *Polymer (Guildf).* **2010**, *51* (12), 2486–2493.

(67) Mansfeld, U.; Hoeppener, S.; Kempe, K.; Schumers, J.-M.; Gohy, J.-F.; Schubert, U. S. *Soft Matter* **2013**, *9* (25), 5966.

(68) Waschinski, C. J.; Tiller, J. C. *Biomacromolecules* **2005**, *6*, 235–243.

(69) Rzayev, J.; Hillmyer, M. a. *J. Am. Chem. Soc.* **2005**, *127* (38), 13373–13379.

(70) Rzayev, J.; Hillmyer, M. A. *Macromolecules* **2005**, *38*, 3–5.

(71) Hernández-Guerrero, M.; Stenzel, M. H. *Polym. Chem.* **2012**, *3* (3), 563.

(72) Wang, X.; Zhou, J.; Lv, X.; Zhang, B.; An, Z. *Macromolecules* **2017**, *50*, 7222–7232.

(73) Figg, C. A.; Carmean, R. N.; Bentz, K. C.; Mukherjee, S.; Savin, D. A.; Sumerlin, B. S. *Macromolecules* **2017**, *50*, 935–943.

(74) Zhang, L.; Shen, H.; Eisenberg, A. *Macromolecules* **1997**, *9297* (96), 1001–1011.

(75) Liu, X.; Wu, J.; Kim, J.; Eisenberg, A. *Langmuir* **2006**, *7*, 419–424.

(76) Azzam, T.; Eisenberg, A. *Langmuir* **2010**, *26* (13), 10513–10523.

(77) Burke, S. E.; Eisenberg, A. *Polymer (Guildf).* **2001**, *42*, 9111–9120.

(78) Choucair, A. A.; Kycia, A. H.; Eisenberg, A.; Colloid, P. A.; Sci, I. *Langmuir* **2003**, No. 40, 1001–1008.

(79) Liu, F.; Eisenberg, A. *J. Am. Chem. Soc.* **2003**, *11*, 15059–15064.

(80) Khougaz, K.; Zhong, X. F.; Eisenberg, A. *Macromolecules* **1996**, *9297* (95), 3937–

3949.

(81) Choucair, A.; Lavigueur, C.; Eisenberg, A. *Langmuir* **2004**, *29*, 3894–3900.

(82) Terreau, O.; Luo, L.; Eisenberg, A. *Langmuir* **2003**, *7*, 5601–5607.

(83) Zhang, L.; Eisenberg, A. *J. Am. Chem. Soc.* **1996**, No. 24, 3168–3181.

(84) Vaccaro, G.; Bianchi, A.; Mauri, M.; Bonetti, S.; Meinardi, F.; Sanguineti, A.; Simonutti, R.; Beverina, L. *Chem. Commun. (Camb).* **2013**, *49* (76), 8474–8476.

(85) Bianchi, A.; Mauri, M.; Bonetti, S.; Koynov, K.; Kappl, M.; Lieberwirth, I.; Butt, H.-J.; Simonutti, R. *Macromol. Rapid Commun.* **2014**, *35*, 1994–1999.

(86) Gregori, M.; Bertani, D.; Cazzaniga, E.; Orlando, A.; Mauri, M.; Bianchi, A.; Re, F.; Sesana, S.; Minniti, S.; Francolini, M.; Cagnotto, A.; Salmona, M.; Nardo, L.; Salerno, D.; Mantegazza, F.; Masserini, M. *Macromol. Biosci.* **2015**, No. 15, 1687–1697.

(87) Pardridge, W. M. *NeuroRx* **2005**, *2* (1), 3–14.

(88) Willersinn, J.; Bogomolova, A.; Brunet Cabré, M.; K J Schmidt, B. V. *Polym. Chem* **2017**, *8*, 1244.

(89) Hiruta, Y.; Nemoto, R.; Kanazawa, H. *Colloids Surfaces B Biointerfaces* **2017**, *153*, 2–9.

(90) Zhu, K.; Liu, G.; Hu, J.; Liu, S. *Biomacromolecules* **2017**, *18*, 2571–2582.

(91) Wong, K. H.; Davis, T. P.; Barner-Kowollik, C.; Stenzel, M. H. *Polymer (Guildf).* **2007**, *48* (17), 4950–4965.

(92) Zhulina, E. B.; Adam, M.; LaRue, I.; Sheiko, S. S.; Rubinstein, M. *Macromolecules* **2005**, *38* (12), 5330–5351.

(93) Kwon, S. Y.; Kim, M. W. *Phys. Rev. Lett.* **2002**, *98* (25), 258302–1.

(94) Tlusty, T.; Safran, S.; Strey, R. *Phys. Rev. Lett.* **2000**, *84* (6), 1244–1247.

(95) Bernheim-Groswasser, A.; Tlusty, T.; Safran, S. A.; Talmon, Y. *Langmuir* **1999**, *15*, 5448–5453.

(96) Jain, S.; Bates, F. S. *Science* **2003**, *300* (5618), 460–464.

(97) Zhang, M.; Wang, M.; He, S.; Qian, J.; Saffari, A.; Lee, A.; Kumar, S.; Hassan, Y.; Guenther, A.; Scholes, G.; Winnik, M. A. *Macromolecules* **2010**, *43*, 5066–5074.

(98) Zhao, J.; Lu, H.; Wong, S.; Lu, M.; Xiao, P.; Stenzel, M. H. *Polym. Chem.* **2017**, *8* (21), 3317–3326.

(99) Kim, K. T.; Zhu, J.; Meeuwissen, S. A.; Cornelissen, J. J. L. M.; Pochan, D. J.; Nolte, R. J. M.; Hest, J. C. M. Van. *J. Am. Chem. Soc.* **2010**, *132*, 12522–12524.

(100) Kulkarni, C. V.; Wachter, W.; Iglesias-Salto, G.; Engelskirchen, S.; Ahualli, S. *Phys. Chem. Chem. Phys.* **2011**, *13* (8), 3004–3021.

(101) Israelachvili, J.; Mitchell, D.; Ninham, B. *J. Chem. Soc., Faraday Trans. 2* **1976**, *72*,

1525–1568.

(102) Klibanov, A. L.; Maruyama, K.; Torchilin, V. P.; Huang, L. *FEBS Lett.* **1990**, *268* (1), 235–237.

(103) Harris, J. M.; Chess, R. B. *Nat. Rev. Drug Discov.* **2003**, *2* (3), 214–221.

(104) Owens Iii, D. E.; Peppas, N. A. *Int. J. Pharm.* **2006**, *307*, 93–102.

(105) Veronese, F. M.; Pasut, G. *Drug Discov. Today* **2005**, *10* (21), 1451–1458.

(106) Gustafson, H. H.; Holt-Casper, D.; Grainger, D. W.; Ghandehari, H. *Nano Today* **2015**, *10* (4), 487–510.

(107) Carrstensen, H.; Muller, R. H.; Muller, B. W. *Clin. Nutr.* **1992**, *11* (5), 289–297.

(108) Rosera, M.; Fischerb, D.; Kisselb, T. *Eur. J. Pharm. Biopharm.* **1998**, *46* (3), 255–263.

(109) Peracchia, M. T. *STP pharma Sci.* **2003**, *13(3)*, 155–161.

(110) Huang, Y.; Szleifer, I.; Peppas, N. A. *J. Chem. Phys.* **2001**, *114* (8), 3809–3816.

(111) Anderson, J. M.; Shive, M. S. *Adv. Drug Deliv. Rev.* **2012**, No. 64, 72–82.

(112) Athanasiou, K. A.; Niederauer, G. G.; Agrawal, C. M. *Biomoterials* **1996**, *17*, 93–102.

(113) Xiang, T. X.; Anderson, B. D. *J. Pharm. Sci.* **2014**, *103* (9), 2759–2771.

(114) Lee, K. S.; Chung, H. C.; Im, S. A.; Park, Y. H.; Kim, C. S.; Kim, S.-B.; Rha, S. Y.; Lee, M. Y.; Ro, J. *Breast Cancer Res. Treat.* **2008**, *108* (2), 241–250.

(115) Kim, D.-W.; Kim, S.-Y.; Kim, H.-K.; Kim, S.-W.; Shin, S. W.; Kim, J. S.; Park, K.; Lee, M. Y.; Heo, D. S. *Ann. Oncol.* **2007**, *18* (12), 2009–2014.

(116) Mai, Y.; Eisenberg, A. *Chem. Soc. Rev.* **2012**, *41* (18), 5969–5985.

(117) Champion, J. A.; Katare, Y. K.; Mitragotri, S. *J. Control. Release* **2007**, *121* (1–2), 3–9.

(118) Hagan, S. A.; Coombes, A. G. A.; Garnett, M. C.; Dunn, S. E.; Davies, M. C.; Illum, L.; Davis, S. S.; Harding, S. E.; Purkiss, S.; Gellert, P. R. *Langmuir* **1996**, *12* (9), 2153–2161.

(119) Riley, T.; Stolnik, S.; Heald, C. R.; Xiong, C. D.; Garnett, M. C.; Illum, L.; Davis, S. S.; Purkiss, S. C.; Barlow, R. J.; Gellert, P. R. *Langmuir* **2001**, *17* (11), 3168–3174.

(120) Riley, T.; Stolnik, S.; Garnett, M. C.; Illum, L.; Davis, S. S.; Taylor, P.; Tadros, T. F. *Langmuir* **2002**, *18* (20), 7663–7668.

(121) Riley, T.; Heald, C. R.; Stolnik, S.; Garnet, C. M.; Illum, L.; Davis, S. S.; King, S. M.; Heenan, R. K.; Purkiss, S. C.; Barlow, R. J.; Gellert, P. R.; Washington, C. *Langmuir* **2003**, *19* (11), 8428–8435.

(122) Posocco, P.; Fermeglia, M.; Pricl, S. *J. Mater. Chem.* **2010**, *20* (36), 7742–7753.

(123) Yang, B.; Lowe, J. P.; Schweins, R.; Edler, K. J. *Biomacromolecules* **2015**, *16* (2), 457–464.

(124) Meng, F.; Hiemstra, C.; Engbers, G. H. M.; Feijen, J. *Macromolecules* **2003**, *36*, 3004–3006.

(125) Ahmed, F.; Discher, D. E. *J. Control. Release* **2004**, *96* (1), 37–53.

(126) Du, B.; Mei, A.; Yin, K.; Zhang, Q.; Xu, J.; Fan, Z. *Macromolecules* **2009**, *42*, 8477–8484.

(127) Park, J.-K.; Kim, D.-W.; Kim, C.-H.; Maeng, K.-S.; Hwang, T.-S.; Kim, Y.-C. *Polym. Eng. Sci.* **1991**, *31* (12), 867–872.

(128) Deng, C.; Rong, G.; Tian, H.; Tang, Z.; Chen, X.; Jing Xiabin. *Polymer (Guildf).* **2005**, *46*, 653–659.

(129) Savic, R.; Azzam, T.; Eisenberg, A.; Maysinger, D. *Langmuir* **2006**, *22*, 3570–3578.

(130) Gagliardi, M.; Di Michele, F.; Mazzolai, B.; Bifone, A. *J. Polym. Res.* **2015**, *22* (2), 17.

(131) Chognot, D.; Six, J. L.; Leonard, M.; Bonneaux, F.; Vigneron, C.; Dellacherie, E. *J. Colloid Interface Sci.* **2003**, *268*, 441–447.

(132) Qian, H.; Wohl, A. R.; Crow, J. T.; MacOsko, C. W.; Hoye, T. R. *Macromolecules* **2011**, *44* (18), 7132–7140.

(133) Nachtergael, A.; Coulembier, O.; Dubois, P.; Helvenstein, M.; Duez, P.; Blankert, B.; Mespouille, L. *Biomacromolecules* **2015**, *16*, 507–514.

(134) Coady, D. J.; Fukushima, K.; Horn, H. W.; Rice, J. E.; Hedrick, J. L. *Chem. Commun.* **2011**, *47* (11), 3105.

(135) Brown, H. A.; De Crisci, A. G.; Hedrick, J. L.; Waymouth, R. M. *ACS Macro Lett.* **2012**, *1*, 1113–1115.

(136) Lohmeijer, B. G. G.; Pratt, R. C.; Leibfarth, F.; Logan, J. W.; Long, D. A.; Dove, A. P.; Nederberg, F.; Choi, J.; Wade, C.; Waymouth, R. M.; Hedrick, J. L. *Macromolecules* **2006**, *39* (25), 8574–8583.

(137) Lohmeijer, B. G. G.; Pratt, R. C.; Leibfarth, F.; Logan, J. W.; Long, D. a.; Dove, A. P.; Nederberg, F.; Choi, J.; Wade, C.; Waymouth, R. M.; Hedrick, J. L. *Macromolecules* **2006**, *39* (25), 8574–8583.

(138) Reed, R.; Réau, R.; Dahan, F.; Bertrand, G. *Angew. Chemie Int. Ed. English* **1993**, *32* (3), 399–401.

(139) Brown, H. A.; De Crisci, A. G.; Hedrick, J. L.; Waymouth, R. M. *ACS Macro Lett.* **2012**, No. 1, 1113–1115.

(140) Carafa, M.; Mesto, E.; Quaranta, E. *European J. Org. Chem.* **2011**, *13*, 2458–2465.

(141) Cohn, D.; Hotovely-Salomon, A. *Polymer (Guildf).* **2005**, *46* (7), 2068–2075.

(142) Pannu, R. K.; Tanodekaew, S.; Li, W.; Collett, J. H.; Attwood, D.; Booth, C. **1999**, *20*.

(143) Manfredi, N.; Bianchi, A.; Causin, V.; Ruffo, R.; Simonutti, R.; Abbotto, A. *J. Polym. Sci. Pol. Chem.* **2014**, *52*, 719–727.

(144) Heald, C. R.; Stolnik, S.; Kujawinski, K. S.; De Matteis, C.; Garnett, M. C.; Illum, L.; Davis, S. S.; Purkiss, S. C.; Barlow, R. J.; Gellert, P. R. *Langmuir* **2002**, *18* (9), 3669–3675.

(145) Yu, Y.; Zhang, L.; Eisenberg, A. *Macromolecules* **1998**, *9297* (97), 1144–1154.

(146) Hansen, C. M. *Hansen Solubility Parameters A User's Handbook*; 2013; Vol. 53.

(147) Legrand, P.; Lesieur, S.; Bochot, A.; Gref, R.; Raatjes, W.; Barratt, G.; Vauthier, C. *Int. J. Pharm.* **2007**, *344*, 33–43.

(148) Azzam, T.; Eisenberg, A.; Maysinger, D. *Langmuir* **2006**, No. 10, 3570–3578.

(149) Bilati, U.; Allémann, E.; Doelker, E. *Eur. J. Pharm. Sci.* **2005**, *24*, 67–75.

(150) Sato, S.; Gondo, D.; Wada, T.; Kanehashi, S.; Nagai, K. *J. Appl. Polym. Sci.* **2013**, *129* (3), 1607–1617.

(151) Biondi, O.; Motta, S.; Mosesso, P. *Mutagenesis* **2002**, *17* (3), 261–264.

(152) Chanan-Khan, A.; Szebeni, J.; Savay, S.; Liebes, L.; Rafique, N. M.; Alving, C. R.; Muggia, F. M. *Ann. Oncol.* **2003**, *14* (9), 1430–1437.

(153) Szebeni, J. *Toxicology* **2005**, *216* (2–3), 106–121.

(154) Dijkmans, P.; Visser, C.; Kamp, O. *Eur. J. Echocardiogr.* **2005**, *6* (5), 363–366.

(155) Assal, C.; Watson, P. Y. *Gastrointest. Endosc.* **2006**, *64* (2), 294–295.

(156) Armstrong, J. K.; Hempel, G.; Koling, S.; Chan, L. S.; Fisher, T.; Meiselman, H. J.; Garratty, G. *Cancer* **2007**, *110* (1), 103–111.

(157) Brouwers, A.; De Jong, D.; Dams, E.; Oyen, W.; Boerman, O.; Laverman, P.; Naber, T.; Storm, G.; Corstens, F. *J. Drug Target.* **2000**, *8* (4), 225–233.

(158) Ishida, T.; Masuda, K.; Ichikawa, T.; Ichihara, M.; Irimura, K.; Kiwada, H. *Int. J. Pharm.* **2003**, *255* (1–2), 167–174.

(159) Aarthi, T.; Shaama, M. S.; Madras, G. *Ind. Eng. Chem. Res.* **2007**, *46* (19), 6204–6210.

(160) Kagiya, T.; Narisawa, S.; Maeda, T.; Fukui, K. *J. Polym. Sci. Part B Polym. Lett.* **1966**, *4* (7), 441–445.

(161) Seeliger, W.; Aufderhaar, E.; Diepers, W.; Feinauer, R.; Nehring, R.; Thier, W.; Hellmann, H. *Angew. Chemie Int. Ed. English* **1966**, *5* (10), 875–888.

(162) Hoogenboom, R. *Angew. Chem. Int. Ed. Engl.* **2009**, *48* (43), 7978–7994.

(163) Kelly, A. M.; Hecke, A.; Wirnsberger, B.; Wiesbrock, F. *Macromol. Rapid Commun.* **2011**, *32*, 1815–1819.

(164) Aoi, K.; Suzuki, H.; Okada ', M. *Macromolecules* **1992**, *25*, 7073–7075.

(165) Gaertner, F. C.; Luxenhofer, R.; Blechert, B.; Jordan, R.; Essler, M. *J. Control. Release* **2007**, *119* (3), 291–300.

(166) Goddard, P.; Hutchinson, L. E.; Brown, J.; Brookman, L. J. *J. Control. Release* **1989**, *10* (1), 5–16.

(167) Woodle, M. C.; Engbers, C. M.; Zalipsky, S. *Bioconjug. Chem.* **1994**, *5* (6), 493–496.

(168) Zalipsky, S.; Hansen, C. B.; Oaks, J. M.; Allen, T. M. *J. Pharm. Sci.* **1996**, *85* (2), 133–137.

(169) Chang, B.-J.; Prucker, O.; Groh, E.; Wallrath, A.; Dahm, M.; Rühe, J. *Colloids Surfaces A Physicochem. Eng. Asp.* **2002**, *198–200*, 519–526.

(170) Glatzel, S.; Laschewsky, A. E.; Lutz, J.-F.-O. *Macromolecules* **2010**, *44*, 413–415.

(171) Cox, J. K.; Yu, K.; Constantine, B.; Eisenberg, A.; Lennox, R. B. *Langmuir* **1999**, No. 7, 7714–7718.

(172) Dormidontova, E. E. *Macromolecules* **2002**, No. 35, 987–1001.

(173) Glassner, M.; Lava, K.; de la Rosa, V. R.; Hoogenboom, R. *J. Polym. Sci. Part A Polym. Chem.* **2014**, *52* (21), 3118–3122.

(174) Brandup, J.; Immergut, E.; Grulke, E. *Polymer handbook*; 1999.

(175) Saegusa, T.; Ikeda, H.; Fujii, H. *Macromolecules* **1972**, *5*, 108.

(176) Lambermont-Thijs, H. M. L.; Heuts, J. P. A.; Hoeppener, S.; Hoogenboom, R.; Schubert, U. S. *Polym. Chem.* **2011**, *2*, 313–322.

(177) Monnery, B. D.; Shaunak, S.; Thanou, M.; Steinke, J. H. G. *Macromolecules* **2015**, *48*, 3197–3206.

(178) De La Rosa, V. R.; Bauwens, E.; Monnery, B. D.; De Geest, B. G.; Hoogenboom, R. *Polym. Chem.* **2014**, *5*, 4957.

(179) Aydin, S. A.; Erdogan, T.; Sakar, D.; Hizal, G.; Cankurtaran, O.; Tunca, U.; Karaman, F. *Eur. Polym. J.* **2008**, *44*, 2115–2122.

(180) Ray, G. B.; Chakraborty, I.; Moulik, S. P. *J. Colloid Interface Sci.* **2006**, *294* (294), 248–254.

(181) Chaudhuri, A.; Haldar, S.; Chattopadhyay, A. *Biochem. Biophys. Res. Commun.* **2009**, *390*, 728–732.

(182) Wang, X.; Li, L.; Ye, X.; Wu, C. *Macromolecules* **2014**, *47*, 2487–2495.

(183) Winnik, F. M. *Chem. Rev* **1993**, *93*, 587–614.

(184) Kuimova, M. K.; Yahioglu, G.; Levitt, J. A.; Suhling, K. *J. Am. Chem. Soc.* **2008**, *130*, 6672–6673.

(185) Harkness, J. *Biorheology* **1971**, *8* (3), 171.

(186) Letcher, R. L.; Chien, S.; Pickering, T. G.; Sealey, J. E.; Laragh, J. H. *Am. J. Med.*

1981, *70* (6), 1195–1202.

(187) Haidekker, M. A.; Tsai, A. G.; Brady, T.; Stevens, H. Y.; Frangos, J. A.; Theodorakis, E.; Intaglietta, M. *Am J Physiol Hear. Circ Physiol* **2002**, *282*, 1609–1614.

(188) Martin, G. S.; Lewis, C. A. *Semin. Respir. Crit. Care Med. New York Thieme Med. Publ.* **1994**, *25*, 683–693.

(189) Haidekker, M. a; Theodorakis, E. a. *J. Biol. Eng.* **2010**, *4*, 11.

(190) Doolittle, A. K. *J. Appl. Phys.* **1952**, 23:236.

(191) Raut, S.; Kimball, J.; Fudala, R.; Doan, H.; Maliwal, B.; Sabnis, N.; Lacko, A.; Gryczynski, I.; Dzyuba, S. V; Gryczynski, Z. *Phys. Chem. Chem. Phys. Phys. Chem. Chem. Phys* **2014**, *16* (16), 27037–27042.

(192) Besbes, R.; Ouerfell, N.; Latrous, H. *J. Mol. Liq.* **2009**, *145*, 1–4.

(193) Sato, S.; Gondo, D.; Wada, T.; Kanehashi, S.; Nagai, K. *J. Appl. Polym. Sci.* **2013**, *129* (3), 1607–1617.

(194) Hernandez, J. D.; Baum, L. G. *Glycobiology* **2002**, *12* (10), 127–136.

(195) Kwon, D. S.; Gregorio, G.; Bitton, N.; Hendrickson, W. A.; Littman, D. R. *Immunity* **2002**, *16*, 135–144.

(196) Lee, Y. C.; Lee, R. T. *Acc. Chem. Res.* **1995**, *28* (8), 321.

(197) Ting, S. R. S.; Chen, G.; Stenzel, M. H. *Polym. Chem.* **2010**, No. 1, 1392–1412.

(198) Kiessling, L. L.; Grim, J. C. *Chem. Soc. Rev. Chem. Soc. Rev* **2013**, *42* (42), 4476–4491.

(199) Chen, Y.; Lord, M. S.; Piloni, A.; Stenzel, M. H. *Macromolecules* **2015**, *45*, 346–357.

(200) Ambrosi, M.; Cameron, N. R.; Davis, B. G. *Org. Biomol. Chem.* **2005**, *3*, 1593–1608.

(201) Fasting, C.; Schalley, C. A.; Weber, M.; Seitz, O.; Hecht, S.; Koksch, B.; Dernedde, J.; Graf, C.; Knapp, E. W.; Haag, R. *Angew. Chemie - Int. Ed.* **2012**, *51* (42), 10472–10498.

(202) Mammen, M.; Choi, S.-K.; Whitesides, G. M. *Angew. Chem. Int. Ed.* **1998**, *37*, 2754–2794.

(203) Lundquist, J. J.; Toone, E. J. *Chem. Rev.* **2002**, *102*, 555–578.

(204) Dam, T. K.; Brewer, C. F. *Chem. Rev.* **2002**, *102*, 387–429.

(205) Miura, Y.; Koketsu, D.; Kobayashi, K. *Polym. Adv. Technol.* **2007**, *18*, 647–651.

(206) Gestwicki, J. E.; Cairo, C. W.; Strong, L. E.; Oetjen, K. A.; Kiessling, L. L. *J. Am. Chem. Soc.* **2002**, *124*, 14922–14933.

(207) Miura, Y.; Hoshino, Y.; Seto, H. **2015**.

(208) Hasegawa, T.; Kondoh, S.; Matsuura, K.; Kobayashi, K. *Macromolecules* **1999**, *32*, 6595–6603.

(209) Ruiz, C.; Sanchez-Chaves, M.; Cerrada, M. L.; Fernandez-Garcia, M. *J. Polym. Sci. Part A Polym. Chem.* **2008**, *46*, 7238–7248.

(210) Zamora-Leòn, S. P.; Golde, D. W.; Conchat, I. I.; Rivas, C. I.; Delgado-Lòpez, F.; Baselga, J.; Nualart, F.; Vera, J. C. *Med. Sci.* **1996**, *93*, 1847–1852.

(211) Mourad-Zeidan, A. A.; Melnikova, V. O.; Wang, H.; Raz, A.; Bar-Eli, M. *Am. J. Pathol.* **2008**, *173* (6), 1839–1852.

(212) Zhao, J.; Babiuch, K.; Lu, H.; Dag, A.; Gottschald, M.; Stenzel, M. H. *Chem. Commun.* **2014**, *50*, 15928.

(213) von der Ehe, C.; Rinkenauer, A.; Weber, C.; Szamosvari, D.; Gottschaldt, M.; Schubert, U. S. *Macromol. Biosci.* **2016**, *16* (4), 508–521.

(214) Dag, A.; Callari, M.; Lu, H.; Stenzel, M. H. *Polym. Chem.* **2016**, *7*, 1031–1036.

(215) Callari, M.; Aldrich-Wright, J. R.; de Souza, P. L.; Stenzel, M. H. *Prog. Polym. Sci.* **2014**, *39* (9), 1614–1643.

(216) Cameron, N. R.; Spain, S. G.; Kingham, J. A.; Weck, S.; Albertin, L.; Barker, C. A.; Battaglia, G.; Smart, T.; Blanazs, A. *Faraday Discuss.* **2008**, *139*, 359–368.

(217) Pearson, S.; Vitucci, D.; Khine, Y. Y.; Dag, A.; Lu, H.; Save, M.; Billon, L.; Stenzel, M. H. *Eur. Polym. J.* **2015**, *69*, 616–627.

(218) Albertin, L.; Stenzel, M. H.; Barner-Kowollik, C.; Foster, L. J. R.; Davis, T. P. *Macromolecules* **2005**, *38* (22), 9075–9084.

(219) Albertin, L.; Kohlert, C.; Stenzel, M.; Foster, J. R.; Davis, T. P. *Biomacromolecules* **2004**, *5* (2), 255.

(220) Utama, R. H.; Jiang, Y.; Zetterlund, P. B.; Stenzel, M. H. *Biomacromolecules* **2015**, *16*, 2144–2156.

(221) Al-Bagoury, M.; Buchholz, K.; Yaacoub, E.-J. *Polym. Adv. Technol.* **2006**, *17*, 395–418.

(222) Monguzzi, A.; Mauri, M.; Bianchi, A.; Dibbanti, K.; Simonutti, R.; Meinardi, F. *J. Phys. Chem. C* **2016**, *120*, 2609–2614.

(223) Chiefari, J.; Mayadunne, R. T. A.; Moad, C. L.; Moad, G.; Rizzardo, E.; Postma, A.; Skidmore, M. A.; Thang, S. H. *Macromolecules* **2003**, *36*, 2273–2283.

(224) Keddie, D. J.; Moad, G.; Rizzardo, E.; Thang, S. H. *Macromolecules* **2012**, *45*, 5321–5342.